Development of Optical Imaging Methods for Evaluating the Vascular Response to Hind Limb Ischemia

By

Kristin Poole O'Grady

Dissertation

Submitted to the Faculty of the

Graduate School of Vanderbilt University

in partial fulfillment of the requirements

for the degree of

DOCTOR OF PHILOSOPHY

in

Biomedical Engineering

December, 2015

Nashville, Tennessee

Approved:

Craig L. Duvall, Ph.D.

Melissa C. Skala, Ph.D.

Bruce M. Damon, Ph.D.

Jeffrey M. Davidson, Ph.D.

David G. Harrison, M.D.

To my husband, Brian O'Grady, for his support and patience throughout this journey
and
To my family and friends for their infinite support and encouragement

ACKNOWLEDGMENTS

I would like to thank my Ph.D. advisors, Professors Craig Duvall and Melissa Skala, for their guidance and expertise throughout my dissertation project and my development as a scientist. I would also like to thank my committee members, Professors Bruce Damon, Jeffrey Davidson, and David Harrison for providing valuable insight and dedicating time to advising me on this work.

Next, I would like to thank my collaborators and peers for their support and contributions to this work, especially the members of the Biomaterials and Biophotonics laboratories. Many thanks go to Dr. Chetan Patil, Dr. Jason Tucker-Schwartz, and Devin McCormack for their help with OCT and developing image processing code. Dr. Christopher Nelson and Taylor Kavanaugh helped with particle fabrication for therapeutic experiments, and Dr. Fang Yu's help with animal experiments is greatly appreciated. Several undergraduates assisted with experiments and data analysis, including Wesley Sit, Megan Madonna, Jinjoo Lee, and Belle Ye.

This work would not have been possible without the financial support provided by Vanderbilt University Start-Up funding for Professors Melissa Skala and Craig Duvall, the IBM Graduate Fellowship Award, the National Science Foundation Graduate Research Fellowship, the P.E.O. Scholar Award, Vanderbilt Discovery Grant, NIH R21 HL109748, and American Heart Association Grant-in-Aid 12GRNT 12060235. I would also like to acknowledge laboratories and core facilities in which portions of this work were performed, including the Vanderbilt University Institute of Imaging Science (VUIIS), the Translational Pathology Shared Resource (TPSR), and the labs of Dr. Anita Mahadevan-Jansen and Dr. Lillian Nanney.

TABLE OF CONTENTS

Page

DEDICATION ii

ACKNOWLEDGMENTS iii

LIST OF TABLES vi

LIST OF FIGURES vii

Chapter

1. INTRODUCTION 1

- 1.1 Motivation 1
- 1.2 Optical Imaging Approach 3
- 1.3 Therapeutic Treatment Approach 5
- 1.4 Innovation 6
- 1.5 Specific Aims 7
- 1.6 Outline 8

2. BACKGROUND 9

- 2.1 Peripheral Arterial Disease and Diabetes 9
- 2.2 Treatment Strategies for PAD 11
- 2.3 Current Methods for the Hind Limb Ischemia Model of PAD 15
- 2.4 Hyperspectral Imaging 17
- 2.5 Optical Coherence Tomography 19
- 2.6 Novel Therapeutic Strategies 20

3. QUANTITATIVE OPTICAL IMAGING OF VASCULAR RESPONSE IN VIVO IN A MODEL OF PERIPHERAL ARTERIAL DISEASE 22

- 3.1 Abstract 22
- 3.2 Introduction 23
- 3.3 Methods 25
- 3.4 Results 36
- 3.5 Discussion 50
- 3.6 Acknowledgments 57

4. QUANTIFYING THE VASCULAR RESPONSE TO ISCHEMIA WITH SPECKLE VARIANCE OCT 58

4.1 Abstract 58
4.2 Introduction 58
4.3 Methods 62
4.4 Results 67
4.5 Discussion and Conclusions 71
4.6 Acknowledgments 77

5. ROS-RESPONSIVE MICROSPHERES FOR ON DEMAND ANTIOXIDANT THERAPY IN A MODEL OF DIABETIC PERIPHERAL ARTERIAL DISEASE 78

5.1 Abstract 78
5.2 Introduction 79
5.3 Materials and Methods 81
5.4 Results 91
5.5 Discussion 103
5.6 Conclusions 108
5.7 Acknowledgments 108

6. EVALUATING A DUAL-ANTIOXIDANT THERAPY AND THE EFFECT OF DIABETES DURATION ON THE VASCULAR RESPONSE TO ISCHEMIA 109

6.1 Abstract 109
6.2 Introduction 110
6.3 Materials and Methods 112
6.4 Results 121
6.5 Discussion 141
6.6 Conclusions 145
6.7 Acknowledgments 145

7. SYNOPSIS AND FUTURE DIRECTIONS 147

7.1 Summary 147
7.2 Limitations 150
7.3 Future Directions and Recommendations 151
7.4 Contribution to the Field and Broader Impacts 155
7.5 Conclusion 157

Appendix

A. SUPPLEMENTARY FIGURES FOR CHAPTER 5 158
B. SUPPLEMENTARY METHODS AND FIGURES FOR CHAPTER 6 162

REFERENCES 174

LIST OF TABLES

Table Page

2.1 Gene therapy in peripheral arterial disease: bioactivity data 14

4.1 Quantitative morphology metrics extracted from speckle variance OCT images 67

LIST OF FIGURES

Figure Page

2.1 Illustration of the concept of therapeutic angiogenesis....13
2.2 Absorbance spectra of oxygenated and deoxygenated hemoglobin....19

3.1 Hyperspectral imaging system schematic and validation....27
3.2 Optical coherence tomography system schematic and validation....32
3.3 LDPI and tissue oxygen tension measurements in hind limb ischemia....37
3.4 Variability of OxyLite pO_2 measurements....39
3.5 Hemoglobin oxygen saturation recovery in hind limb ischemia....41
3.6 Histograms of hemoglobin oxygen saturation for control and ischemic footpads....42
3.7 Speckle variance OCT projections of vessels in the hind limb....44
3.8 Perfusion measurements with Doppler OCT....46
3.9 Correlation of vascular endpoints in the hind limb ischemia model....48
3.10 Inter-animal variability in measures of the vascular response to ischemia....49

4.1 Illustration of hind limb ischemia model and schematic of OCT system....63
4.2 Flow chart of image processing procedures for speckle variance images....66
4.3 Representative speckle variance OCT images of the adductor muscle....68
4.4 Vascular morphology metrics quantified from speckle variance projections....70
4.5 Structural OCT images from the adductor muscle region imaged over time....71

5.1 Size distribution of curcumin-PPS microspheres analyzed by SEM....92
5.2 Curcumin release from PPS microparticles is ROS dose-dependent and "on demand"....93
5.3 Curcumin loaded PPS microparticles reduce the cytotoxicity of H_2O_2....95
5.4 Curcumin-PPS microspheres are preferentially internalized by activated macrophages and exert functional effects on ROS generation and MCP-1 secretion....96
5.5 PPS microspheres provide sustained, on demand local curcumin release and reduce tissue ROS levels in the ischemic limb *in vivo*....99
5.6 Curcumin loaded PPS microspheres improve ischemic limb recovery in the setting of diabetes *in vivo*....101
5.7 Vessel morphology was imaged non-invasively on day 7 with speckle variance OCT. ...102

6.1 Free and encapsulated tempo-benzoate scavenge superoxide, while blank PPS microspheres scavenge H_2O_2 *in vitro*....123
6.2 Blank PPS and tempo-PPS microspheres protect PGR from bleaching by peroxynitrite .124
6.3 Oxygenation and perfusion outcomes of diabetic and non-diabetic mice with hind limb ischemia....126
6.4 Vascular morphology parameters from intravital OCT images reveal differences between diabetes models....128
6.5 Tissue H_2O_2 levels are elevated in the gastrocnemius of diabetic mice....130
6.6 Two doses of microspheres were compared using functional measures of recovery....132

6.7 The effect of microspheres on H2O2 levels in ischemic muscle was measured using the Amplex Red assay 133
6.8 Hemoglobin saturation and perfusion measured in diabetic mice treated with saline, blank PPS, tempo-PPS, or free tempo-benzoate 135
6.9 Representative time course OCT images of adductor vascular morphology 136
6.10 Representative time course OCT images of gastrocnemius vascular morphology 137
6.11 Vessel morphology parameters were quantified from OCT images of the adductor muscle region after treatment with microspheres 138
6.12 Vessel morphology parameters were quantified from OCT images of the gastrocnemius muscle region after treatment with microspheres 139
6.13 CD68 and nitrotyrosine IHC were performed on gastrocnemius muscles extracted at day 8 post-surgery 140

7.1 "Mild" and "severe" vessel ligation and transection locations for the mouse hind limb ischemia model 154

A.1 Polymer synthesis scheme and structure for poly(propylene sulfide) 158
A.2 Curcumin loaded PPS microspheres reduce the cytotoxicity of H_2O_2 (middle dose) 158
A.3 Animals treated with curcumin PPS microspheres have significantly higher perfusion in the hind limb footpads compared to blank PPS or saline treatment 159
A.4 Representative H&E stained sections from the ischemic gastrocnemius muscle at day 7 for each treatment group 160
A.5 Free curcumin is insoluble in aqueous solution and crystalizes, consequently increasing ROS in the ischemic muscle 161

B.1 Synthesis scheme for PPS, ^{1}H NMR spectrum, and mechanisms of ROS scavenging 164
B.2 In older mice, 15 weeks of diabetes significantly reduces vessel area density and vessel length fraction in the gastrocnemius muscle 165
B.3 General linear model of hemoglobin saturation longitudinal response to ischemia and therapeutic treatment 166
B.4 General linear model of LDPI perfusion longitudinal response to ischemia and therapeutic treatment 167
B.5 Representative OCT images for the adductor at day 7 for treatment groups 168
B.6 Representative OCT images for the gastroc at day 7 for treatment groups 169
B.7 General linear model of adductor vessel area density response to ischemia and therapeutic treatment 170
B.8 General linear model of adductor vessel length fraction response to ischemia and therapeutic treatment 171
B.9 General linear model of gastrocnemius vessel area density response to ischemia and therapeutic treatment 172
B.10 General linear model of gastrocnemius vessel length fraction response to ischemia and therapeutic treatment 173

CHAPTER 1

INTRODUCTION

Text partially adapted from:

Poole KM, Tucker-Schwartz JM, Sit WW, Walsh AJ, Duvall CL, Skala MC. Quantitative optical imaging of vascular response in vivo in a model of peripheral arterial disease. American Journal of Physiology – Heart and Circulatory Physiology. 2013; 305(8):H1168-H1180

Poole KM, Nelson CE, Joshi RV, Martin JR, Gupta MK, Haws SC, Kavanaugh TE, Skala MC, Duvall CL. ROS-responsive microspheres for on demand antioxidant therapy in a model of diabetic peripheral arterial disease. Biomaterials. 2015; 41(0):166-175

1.1 Motivation

Peripheral arterial disease (PAD) affects millions of individuals and increases the risk of myocardial infarction and stroke [1-3]. PAD is an occlusive arterial disease and is most often used to describe disease of arteries supplying the lower extremities. Symptoms include intermittent claudication, non-healing ulcers, gangrene, ischemic rest pain and critical limb ischemia [4], all of which contribute to a reduced quality of life. Common treatment strategies for PAD patients include modification of risk factors (i.e. smoking cessation), exercise, pharmacotherapy, and surgical revascularization, although some patients are not suitable candidates for the latter due to diffuse disease [5]. Development of novel PAD treatments that are less invasive and more effective than the current standard of care is a significant focus within basic and clinical cardiovascular research. Although promising results from preclinical studies have justified translation of pro-angiogenic therapies, recent clinical trials have yielded only mildly-encouraging, insignificant trends toward improvement in secondary endpoints [6-10]. Several factors may contribute to the disparity between successful preclinical studies and unsuccessful clinical trials, including the use of young and healthy animals for evaluating novel therapies in the mouse hind limb ischemia (HLI) model of PAD [11], rather than more relevant

preclinical models such as aged, diabetic, or hypertensive mice. These models are more representative of conditions associated with PAD in humans, but they are typically more time- and cost-intensive to implement [6]. Preclinical models are also typically assessed only in the early stages of HLI recovery, and very few experimental designs include time points to assess long-term stability of therapeutically-stimulated neovasculature. However, it has been recently shown that therapeutic angiogenesis treatments can induce unstable vessels that regress after cessation of treatment, so long-term monitoring is important for thorough evaluation of a new therapy at the preclinical stage. Additionally, late-stage regression of vascular responses that occur immediately following induction of HLI is particularly prevalent in the challenged setting of diabetes [12, 13].

PAD is especially relevant to individuals with diabetes mellitus (DM), since diabetic patients have a four times greater risk of developing PAD than the general population [5], worse lower-extremity function [14], and a greater risk of amputation [2, 15]. Despite the significance and severe implications of diabetes-related PAD, a better understanding of the effect of diabetes on collateral vessel formation and treatment response is needed in order to develop more successful therapies for DM-PAD patients [13, 16]. The streptozotocin model of DM has been used extensively in preclinical research to study the pathways that lead to insulitis and β cell death [17]. The mouse HLI model [11] has been used to study postnatal blood vessel formation and plays a vital role in testing new therapeutic angiogenesis approaches. Recently, these models have been combined in an effort to develop better treatments for DM-PAD patients [18, 19]. However, a key limitation to carrying out more thorough longitudinal analyses during preclinical testing of pro-angiogenic therapies is the lack of quantitative, non-invasive techniques to monitor relevant physiological endpoints (e.g. microvascular density and perfusion, blood velocity, blood

oxygenation) over time in the same animal. Current techniques for evaluating vascular recovery in the HLI model suffer from several limitations. Microcomputed tomography (micro-CT) permits global analysis of the vascular network in the entire limb and provides highly quantitative 3D data; however, it requires post-mortem perfusion with contrast agents making it inefficient for longitudinal studies [20-22]. Similarly, x-ray angiography provides visualization of collateral arteries but it too is a post-mortem technique [23]. Histology quantifies microvessel density but is post-mortem, 2D and can be subject to sampling error. Laser Doppler perfusion imaging (LDPI) provides a non-invasive, functional measure of blood flow, but it is superficial, low resolution, and provides a relative rather than absolute measurement [11]. These techniques provide limited insight into structure-function relationships involved in the vascular response to ischemia. With this existing toolset, numerous cohorts of mice as well as access to and expertise in using multiple complementary instruments are required to complete a comprehensive, longitudinal analysis of the vascular response. This makes preclinical studies expensive and time-consuming. Providing the research community with enabling technologies for robust, standardized, and longitudinal measurements would catalyze new discoveries through better elucidation of the angiogenesis and arteriogenesis processes, more rapid screening of new therapeutic agents, and acceleration of the engineering of delivery systems [24, 25].

1.2 Optical Imaging Approach

This work focuses on the development of a non-invasive, optical imaging platform for studying vascular structure, oxygenation, and hemodynamics in the hind limb ischemia model in wild type mice and in the setting of diabetes. This platform consists of hyperspectral imaging and optical coherence tomography (OCT) which measure hemoglobin oxygen saturation and blood flow plus vessel morphology, respectively, in a living animal. These techniques provide a robust

evaluation of the vascular response to ischemia with quantitative, high resolution, longitudinal data from each animal. Furthermore, the optical imaging approach has been combined with complementary information obtained with conventional methods such as LDPI and histology to study the vascular response to novel therapeutic treatments developed in this work.

Hyperspectral imaging is used to quantify hemoglobin oxygen saturation *in vivo* by collecting absorption images at multiple wavelengths and fitting the resulting absorption curve at each pixel to oxy- and deoxyhemoglobin spectra using a modified version of Beer's Law [26-28]. Hyperspectral imaging provides a quantitative, spatially-resolved measurement, and it is non-invasive and does not require contrast agents or contact with the tissue, which allows for repeated *in vivo* measurements over a time course of ischemic recovery.

Optical coherence tomography (OCT) is a high resolution, 3D optical imaging technique that can non-destructively visualize structural features in tissue at cellular-level resolution with imaging depths of ~1-3 mm [29, 30]. Cross sectional images are acquired by resolving the difference in path lengths between reflecting and scattering sites in the sample and that of a reference arm using a Michelson interferometer. Doppler OCT, a functional extension of OCT, images microvessel networks and blood velocities in 3D [31, 32] in humans [33, 34] and in preclinical models [35-38] through detection of Doppler shifts arising from motion in the sample (i.e. flowing red blood cells) [32]. Speckle variance OCT techniques are also sensitive to blood flow and may be used to obtain vessel morphology information [39]. Currently, morphological endpoints such as vascular density and vessel size are obtained from post-mortem histology, micro-CT, and angiography techniques in the HLI model. OCT provides the advantage of obtaining these endpoints intravitally with simultaneous acquisition of functional endpoints such

as blood flow. This facilitates a better understanding of structure-function relationships and enables longitudinal measurements of these endpoints within individual mice.

1.3 Therapeutic Treatment Approach

Development of collateral vessels can functionally compensate for obstructed arteries in patients with PAD, providing motivation for vascular biologists to study the mechanisms that control formation and remodeling of vasculature. Complementary research on therapeutic angiogenesis seeks to develop clinical approaches for manipulating these mechanisms to stimulate formation of new blood vessels that will bypass diseased arteries and abrogate the symptomatic effects of PAD [24]. Early clinical trials have focused on delivery of growth factors such as FGF or the genes that encode them, but these approaches have shown limited efficacy [12, 40].

In the context of diabetes, there is a chronic pro-inflammatory and oxidative stress environment which contributes to both endothelial dysfunction and a predisposition to PAD [41, 42]. Preclinical studies have shown that animals with type 1 diabetes have an impaired vascular response to ischemia [43-45] and that decreasing oxidative stress improves post-ischemic neovascularization [43, 44]. Therefore, the therapeutic treatments we have developed and screened using the optical imaging platform have been targeted toward reducing oxidative stress in diabetic mice. These therapies are based on poly(propylene sulfide) (PPS) microparticles that can be used to encapsulate antioxidant and anti-inflammatory drugs and provide “on demand” delivery, as PPS transitions from a hydrophobic to a hydrophilic state upon exposure to reactive oxygen species. The ability to modulate therapeutic release based upon environmental demand [46-49] is anticipated to yield more efficient and sustained local delivery, particularly when applied in the context of diabetic PAD.

1.4 Innovation

This project represents a significant development of the application of intravital optical imaging techniques and quantification of novel biomarkers in the mouse HLI model of PAD. Current techniques are high resolution and invasive/post-mortem, or non-invasive and semi-quantitative. These techniques are unable to provide intravital, quantitative, structure *and* function information for the vascular response of the hind limb without excessive use of mice and access to multiple instruments. The development of hyperspectral imaging and OCT methods and biomarkers for the HLI model allows for new insight into the physiology of the vascular response to ischemia (both with and without the complication of diabetes) and provides an improved platform for preclinical screening of novel therapeutic approaches. Non-invasive, longitudinal imaging also mitigates the impact of inter-animal variability present in measures of recovery even within inbred strains of mice [50-52], and allows one to circumvent artifacts associated with post-mortem animal evaluation caused by injection of viscous contrast agents at super-physiologic pressures or masking of desired epitopes due to fixation [20-22].

In addition to the improved toolset we have developed for studying the vascular response to hind limb ischemia, we have demonstrated the utility of our optical imaging approach through diabetes and therapeutic treatment studies. Reactive oxygen species-responsive PPS microparticles were successfully utilized for encapsulation and sustained, on demand delivery of antioxidant and anti-inflammatory drugs in the diabetic mouse HLI model of PAD, and the particles reduced reactive oxygen species (ROS) levels *in vitro* and *in vivo*. The use of PPS microparticle-based, environmentally-sensitive depots represents a compelling approach to provide on demand bioavailability of hydrophobic antioxidant and/or anti-inflammatory drugs

for treatment of diabetic PAD or other localized tissue sites affected by chronic inflammatory diseases.

1.5 Specific Aims

The objectives of this dissertation are to develop quantitative biomarkers for vascular morphology and function in the HLI model from OCT and hyperspectral imaging data, test the ability of these techniques to characterize the vascular response in the diabetic phenotype, and evaluate novel therapeutic approaches for treating diabetic PAD. These objectives will be addressed through completion of the following three specific aims:

Aim 1: Develop and validate OCT and hyperspectral imaging methods for imaging vascular morphology and function in the HLI model. Image acquisition and processing procedures will be established in wild-type mice with HLI. Biomarkers for collateral vessel morphology and blood flow (from OCT) and blood oxygenation (from hyperspectral imaging) will be extracted and quantified from the optical imaging data sets. The optical imaging endpoints will be validated against gold standard techniques.

Aim 2: Characterize the effect of the diabetic phenotype on the vascular response to HLI. The hyperspectral imaging and OCT methods developed in Aim 1 will be used to assess the effect of diabetes on the rate and extent of recovery from HLI. The temporal changes in vessel morphology and hemodynamics will be compared between control mice and mice with streptozotocin-induced Type 1 diabetes. The longitudinal, non-invasively acquired data sets will provide previously unattainable information which may lead to new insight into the vascular response to hemodynamic changes such as late-stage vessel regression in the context of DM.

Aim 3: Apply a combination of optical imaging and conventional methods to develop new, more effective therapeutic interventions for improving HLI recovery in the

setting of diabetes. Therapeutic treatments such as controlled, local release of antioxidant and anti-inflammatory drugs will be tested in the diabetic mouse HLI model using novel drug delivery systems. Therapeutic response will be evaluated using hyperspectral imaging and OCT in combination with conventional methods including LDPI and histology.

1.6 Outline

In this dissertation, a description of the development and validation of a preclinical optical imaging platform for studying temporal and therapeutic responses to hind limb ischemia is given. Chapter 1 provides the motivation and introductory information for this research and outlines the specific aims that are addressed. Chapter 2 provides background information on peripheral arterial disease, microvascular complications associated with diabetes, methods for studying vascular structure and function, and environmentally-responsive therapies. Chapter 3 describes the development of the optical imaging platform and its validation in wild-type mice with hind limb ischemia. In Chapter 4, two wild-type strains known to have differing responses to ischemia are used to further validate the application of OCT to imaging vascular morphology, and a new swept-source OCT system is incorporated into the imaging platform. Chapter 5 describes the delivery of the antioxidant and anti-inflammatory agent curcumin from environmentally responsive microparticles which is evaluated *in vitro* and in diabetic mice with hind limb ischemia. In Chapter 6, variations on the streptozotocin model of type 1 diabetes are compared using the imaging platform, and an ROS-responsive microparticle system for delivery of a superoxide dismutase mimetic is evaluated in mice with long-term hyperglycemia. Finally, a summary of the major results and a discussion of the broader impacts, challenges, and future directions for this work will conclude this dissertation.

CHAPTER 2

BACKGROUND

Text partially adapted from:

Poole KM, Tucker-Schwartz JM, Sit WW, Walsh AJ, Duvall CL, Skala MC. Quantitative optical imaging of vascular response in vivo in a model of peripheral arterial disease. American Journal of Physiology – Heart and Circulatory Physiology. 2013; 305(8):H1168-H1180

Poole KM, McComack DR, Patil CA, Duvall CL, Skala MC. Quantifying the vascular response to ischemia with speckle variance optical coherence tomography. Biomedical Optics Express. 2014; 5(12):4118-4130

Poole KM, Nelson CE, Joshi RV, Martin JR, Gupta MK, Haws SC, Kavanaugh TE, Skala MC, Duvall CL. ROS-responsive microspheres for on demand antioxidant therapy in a model of diabetic peripheral arterial disease. Biomaterials. 2015; 41(0):166-175

Poole KM. 2012. Quantitative optical imaging of vascular structure and function in a model of peripheral arterial disease (Master's Thesis). Vanderbilt University.

2.1 Peripheral Arterial Disease and Diabetes

As many as 8 million American adults are affected by peripheral arterial disease (PAD) which is associated with significant morbidity and mortality [1]. PAD is an occlusive arterial disease affecting non-coronary arteries, and it is most often used to describe disease of the arteries supplying the lower extremities. Symptoms include intermittent claudication, non-healing ulcers, ischemic rest pain and critical limb ischemia [4]. PAD is also associated with increased risk of myocardial infarction and stroke [2, 3]. Therapy for PAD patients consists of modification of risk factors, exercise, pharmacotherapy, and surgical revascularization [5]. However, some patients may have prior revascularization procedures or diffuse atherosclerosis and therefore be poor candidates for surgical intervention [16]. Therapeutic angiogenesis has been investigated as an adjunct approach to managing PAD through delivery of angiogenic growth factors such as vascular endothelial growth factor (VEGF) in recombinant protein or

gene delivery form. This strategy aims to increase blood flow to ischemic tissue by inducing formation of a collateral vessel network [16, 53]. Some of the early clinical trials have shown mildly promising results, but quantitative analysis of the efficacy of new therapeutics is lacking [16].

Peripheral arterial disease is most commonly caused by atherosclerosis, but it may also be a secondary disease to cardiac or vascular embolism, vasculitis, hypercoagulopathy, vascular dissection, vascular compression syndromes, and other disorders [4]. The classical risk factors that are associated with more than 50% of PAD cases in the population include smoking, diabetes mellitus, dyslipidemia and hypertension, and prevalence increases with age [54]. Diabetes is a particularly potent risk factor, as patients with diabetes have a risk of developing PAD that is four times that of the general population. In diabetic patients, exposure of the vasculature to excessive glucose increases endothelial cell nitric oxide synthase (eNOS) expression and superoxide production. This leads to increased generation of hydroxyl radicals, hydrogen peroxide, and peroxynitrite [41, 55, 56], and the chronic oxidative stress and accompanying inflammation contribute to endothelial dysfunction and microvascular complications [41, 42]. Patients who smoke and have diabetes further increase that risk by 2.5 fold [5]. After accounting for the classical risk factors, nearly 50% of PAD cases are caused by unmeasured factors that likely result from hundreds of genes interacting with each other and the environment [4]. Several studies have been conducted in which inherited factors were concluded to contribute to the manifestation of PAD, and genetic variations have been discovered that are predictive of coronary artery disease and PAD [54, 57, 58]. However, genetic variations that are more specific for PAD are unlikely to be found [4].

Despite having known risk factors, PAD is underdiagnosed since only 10% to 30% of PAD patients present with the classic symptom of intermittent claudication [4]. Clinical studies have

determined that asymptomatic patients are more likely to be diagnosed by non-invasive testing with the ankle-brachial index (ABI) test, but since many clinicians rely on claudication symptoms alone to detect PAD, 85% to 90% of PAD diagnoses may be missed [59]. To measure the ABI, a Doppler ultrasound probe is used to measure the systolic blood pressures in the upper extremities at the brachial arteries and in the lower extremities at the dorsalis pedis and posterior tibial arteries [54, 59]. The ABI is defined as the higher of the two ankle systolic pressures divided by the higher brachial systolic pressure. An ABI less than or equal to 0.9 is the criterion for diagnosis of PAD [54, 59]. Once ABI testing is adopted by more clinicians as a simple, non-invasive way to diagnosis PAD in asymptomatic patients with known risk factors, the next step will be to improve upon long term treatment of those affected by this disease.

2.2 Treatment Strategies for PAD

Treatment options for PAD patients include management of risk factors, supervised exercise programs, pharmacotherapy, and surgical intervention [5, 60]. Some risk factors, such as smoking, are relatively straightforward to address. Smoking is the dominant modifiable risk factor for PAD, and a dose-dependent relationship has been observed between smoking and severity of PAD [60]. Poor wound healing, increased risk of amputation, and increased mortality are all linked to smoking, especially in diabetic patients. With smoking cessation the 10 year survival rate in diabetic PAD patients was 82%, a significant improvement over the 46% survival rate of those who did not stop smoking [5]. Exercise is another life-style change that can have an impact on symptoms for PAD patients. It significantly improves maximal walking time and overall walking ability in patients with stable intermittent claudication, and is more effective than both antiplatelet therapy and angioplasty [60]. Other risk factors can be addressed with pharmacotherapy such as statin drugs, antihypertensive drugs and antiplatelet therapy which may reduce the incidence of claudication and

increase maximum walking distance [60]. Diabetes can be more complicated to address as a risk factor for PAD, since diabetic patients tend to have more diffuse vascular disease. Control of blood glucose levels has been shown to reduce microvascular complications of diabetic PAD, but there were no significant reductions in stroke, myocardial infarction or amputation due to PAD. Instead, blood pressure and blood cholesterol levels should be rigorously controlled with pharmacotherapy and life-style changes to prevent serious vascular events in diabetic PAD patients [60].

Surgical revascularization procedures are an option for patients that fail to improve with risk factor management and pharmacotherapy, have non-healing ulcerations, gangrene, or critical limb ischemia [5]. These procedures include percutaneous transluminal angioplasty (PTA) and bypass surgery. PTA has been shown to restore adequate blood flow in patients with critical limb ischemia, and bypass grafts have been performed effectively on more distal arteries in the limb [16]. Both types of revascularization have reduced rates of early major amputation in comparison with patients without revascularization [16].

Some patients, particularly those with diabetes or prior revascularization procedures, are poor candidates for surgical interventions. Diffuse atherosclerosis in multiple anatomical regions is common in diabetic PAD patients and difficult to treat, and repeat surgeries are technically prohibitive [16, 61]. Thus, there is a significant, unmet need for alternative treatment strategies for patients with critical limb ischemia. Efforts to meet this need started as early as 1994 with a human clinical trial in which vascular endothelial growth factor (VEGF) was delivered as a naked plasmid intramuscularly by Baumgartner et al. This phase 1 clinical trial sought to test the concept of therapeutic angiogenesis in patients with critical limb ischemia after preclinical studies showed that angiogenic growth factors can stimulate collateral artery development. While the sample size of this study was small, they observed significant improvements in the ABI, evidence of improved distal

blood flow, and improvement in ischemic ulcers [62]. Figure 2.1 illustrates the concept of therapeutic angiogenesis in which growth factors are delivered to promote remodeling and growth of collateral vessels to compensate for the reduced blood flow caused by PAD.

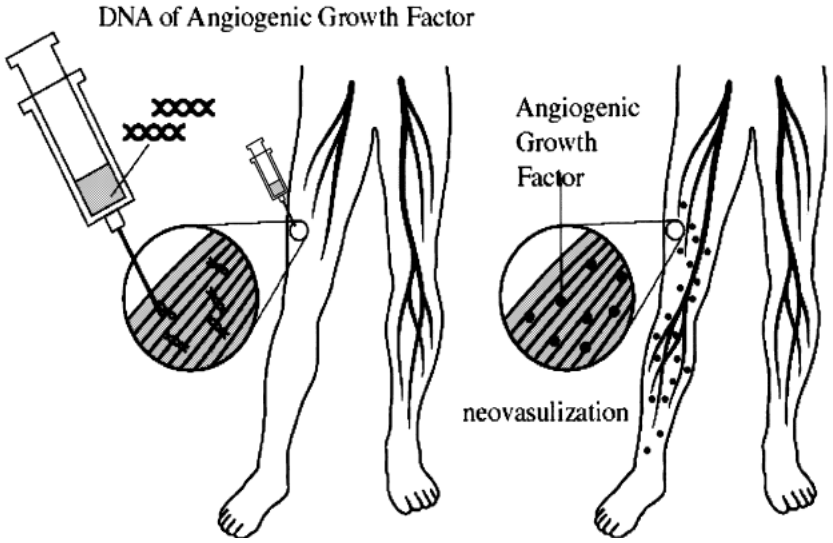

Figure 2.1: Illustration of the concept of therapeutic angiogenesis [61].

Since this study, many other angiogenic growth factors have been tested in clinical trials including various forms of VEGF, fibroblast growth factor (FGF), and hepatocyte growth factor (HGF) [63, 64]. As shown in Table 2.1, some of the early clinical trials have produced mildly promising results, but quantitative analysis of the efficacy of new treatments is lacking due to the challenges of choosing patients and measuring a true signal of bioactivity among the background noise of variability between patients with chronic critical limb ischemia [25]. This is particularly true for patients with diabetes, a population in which therapeutic angiogenesis has not been studied enough. There is also a concern about the safety of growth factor administration in diabetic PAD patients, because they have a greater risk of widespread vascular disease including retinopathy which might be exacerbated by proangiogenic growth factors [16, 25]. In non-diabetic patients with

PAD, some adverse effects have been observed with therapeutic angiogenesis treatment, including hypotension, vascular leakage, and transient tissue edema [25].

Table 2.1: Gene therapy in peripheral arterial disease: bioactivity data [25].

Trial Design	Condition	Treatment(s) Dosing	Route	Patients Verum/Placebo, n	Follow-Up	Parameters of Bioactivity	Trends for Bioactivity
Phase I/II							
DELTA-1 phase II double-blind, placebo-controlled, multicenter trial	PAD; claudication	Del-1 plasmid (VLTS-589)	IM	52/53	30-90-180 d	Δ Walking time (PE); Δ ABI; Δ COT; Δ QoL	None
PREVENT I phase I double-blind trial	PAD/revascularization, CLI, vein bypass graft	E2F decoy (edifoligide)	Ex vivo	16/8/17	12 mo	Graft occlusion	↓Graft occlusion, critical stenosis, revision
Phase I trial	PAD, CLI	FGF-1 plasmid (NV1FGF); 1× 500-16 000 μg, 2× 500-8000 μg	IM	Safety 51/0; efficacy 15/0	3-6 mo	$TcPO_2$, ABI, TBI, pain, ulcer healing	↑$TcPO_2$ (P=0.01), ↑ABI (P=0.01), ↓pain (P=0.001), ↓ulcer size (P=0.01)
PM202 phase II double-blind, placebo-controlled, multicenter trial	PAD, CLI	FGF-1 plasmid (NV1FGF), 2-16 mg	IM	71	N/A	Δ $TcPO_2$ (PE), ABI, TBI, ulcer healing, amputation, death	↓Death, amputation
TALISMAN 201 phase II double-blind, placebo-controlled, multicenter trial	PAD, CLI	FGF-1 plasmid (NV1FGF), 4× 4 mg	IM	56/56	25 wk	Complete ulcer healing (PE), ABI, amputation, death	↓Risk of all amputations (P=0.015), ↓risk of major amputations (P=0.015), ↓risk of death
Phase I dose-escalation, double-blind, placebo-controlled trial	PAD, claudication	rh bFGF, 1× 10, 1× 30, 2× 30 mg/kg	IA	4-5-4/6	6 mo	Calf flow (plethysmography)	↑Blood flow (P=0.002)
Phase II dose-escalation, double-blind, placebo-controlled trial	PAD, claudication	rh bFGF, 6× 2 μg · kg^{-1} · wk^{-1}	IV	16/8 (prematurely terminated)	4-8-12 wk	PWT (PE), QoL	None
TRAFFIC phase II, double-blind, placebo-controlled trial	PAD, claudication	rh FGF-2, 1× or 2× 30 μg/kg	IA	66-61/68	90-180 d	PWT (PE), Δ PWT, COT, Δ ABI, QoL	↑Change in PWT (day 90, P=s), ↑ABI (day 90, P=s)
Phase I/IIa	PAD/Buerger's, CLI	bFGF/gelatin hydrogel sphere, 200 μg	IM	7/0	4-24 wk	6-min Walk, $TcPO_2$, rest pain, ABI, ulcer healing, perfusion (laser Doppler), thermography	↑Distance for 6-min walk (P=0.023), ↑$TcPO_2$ (P=0.03), ↓rest pain (P=0.022), improved ulcers (5/6), ↑ABI (4 wk, P=0.024), ↑limb perfusion (P=0.015), ↑limb temperature (4 wk, P<0.05)
Phase I/II dose-escalation, double-blind, placebo-controlled, multicenter trial	PAD, CLI	Ad5FGF-4, 2.87×10^{8}-10^{10} VP	IM	10/3	12 wk	Rest pain, ABI, angiography (DSA), perfusion (MRI, scintigraphy)	↓Rest pain (4/10), more/bigger vessels

Despite the lack of a clinical breakthrough in therapeutic angiogenesis treatment to date, there are several reasons why researchers continue to pursue this problem so that quality of life can be improved for patients who do not respond to risk factor management or qualify for surgical intervention. Work in this field is motivated by the fact that single genes appear to activate potent angiogenic mechanisms, and these effects may be magnified by activating specific targets and pathways with therapeutic agents. Additionally, novel delivery methods can be designed to direct therapeutic agents to the disease locus and potentially reduce the side effects observed in previous studies. These novel delivery strategies, along with a search for the most efficient and safe combination of proangiogenic genes and/or proteins, are currently being pursued in preclinical studies [25].

2.3 Current Methods for the Hind Limb Ischemia Model of PAD

The mouse hind limb ischemia (HLI) model [11] has been used to study postnatal blood vessel formation and plays a vital role in testing new therapeutic angiogenesis approaches before they can be advanced to clinical trials. Typically, the femoral artery and vein are isolated from the femoral nerve after making a small incision in the hind limb. The artery and vein are then ligated with sutures at one or two locations. Depending on the severity of ischemia desired for the experiment, a segment of the vessels between the ligation points may be excised. These studies generally use a combination of several techniques to obtain information about the morphological and functional responses of the vasculature after induction of ischemia. In addition to studying the effect of therapeutic angiogenesis treatments on wild type mice, mouse models of diabetes and genetically modified strains can be included in these studies to better understand the mechanisms of vascular recovery in the context of conditions that impair angiogenesis and increase the likelihood and severity of PAD [17, 45, 65].

Despite the widespread use of the mouse hind limb ischemia model, current techniques for evaluating vascular recovery suffer from several limitations. Vascular density parameters, including vessel number and lumen area, may be measured using histological evaluation of CD31 and α-smooth muscle actin expression [11, 66-68], but this technique is restricted to two dimensional sections of excised tissue and does not allow for individual animals to be monitored over time. Similarly, morphological data may be derived from microcomputed tomography (micro-CT) [21, 22] and x-ray angiography [23, 66, 69], but these are also terminal methods that require injection of contrast agents. Laser Doppler perfusion imaging (LDPI) is widely used for the HLI model, since it provides a non-invasive, functional measure of blood flow that can be used to track individual animals over time. However, it is superficial and provides a relative rather than absolute measurement [11]. A similar relative measure of recovery can be acquired with optical spectroscopy, which provides a point-based measurement of the oxygen saturation of hemoglobin based on the differing absorption spectra of oxyhemoglobin and deoxyhemoglobin at specific wavelengths [23, 65]. Other methods for measuring tissue oxygenation at the microvascular level are more quantitative and include polarographic electrodes and fluorescence lifetime needle-based sensors, but these devices have several limitations including small sampling area, long stabilization periods, and invasiveness [70]. Measurements of pO_2 can also be obtained less invasively with the electron paramagnetic resonance (EPR) oximetry method, but this requires injection of an exogenous material [69]. While each of these techniques provides important endpoints for hind limb ischemia studies, access to multiple instruments and multiple cohorts of mice are required to study the effects of novel therapeutic treatments over time. A complete picture of the structure-function relationships

involved in the vascular response to ischemia is not currently attainable since robust quantitative endpoints cannot be obtained intravitally within the same mouse over time.

Several *in vivo* imaging methods have been employed to evaluate vascular remodeling over time in other preclinical models, including fluorescent microscopy [28, 71], photoacoustic microscopy [72, 73], laser speckle imaging [74, 75], high frequency ultrasound [76], and magnetic resonance (MR) angiography [69, 77]. These methods provide the advantage of assessing dynamic changes in the vasculature within individual animals, but there are often trade-offs between resolution, field of view, and imaging depth. For example, MR angiography and high frequency ultrasound provide relatively low resolution (~100 μm) images of vasculature but can penetrate deeper within tissue [76, 77], while microscopy provides higher resolution (sub-micron) images of vasculature at relatively shallow depths of approximately 0.2 mm [28]. Photoacoustic microscopy improves upon the penetration depth of fluorescent microscopy with a depth of ~0.5 mm while maintaining axial resolution on the order of 10 μm. However, axial resolution degrades with distance from the focal point [73]. Laser speckle imaging provides vascular maps with approximately 10-25 μm resolution and covers larger spatial areas than microscopy, but similar to LDPI, the data are two dimensional and superficial (< 1 mm) [74, 75]. While each of these methods has been successfully applied to assess vascular morphology in preclinical studies, there are trade-offs with each and the ideal methodology is application-specific.

2.4 Hyperspectral Imaging

Current methodologies used to evaluate the vascular response in the HLI model lack the ability to provide quantitative, longitudinal data on vascular structure and function from individual animals. Optical imaging methods help us address these limitations, since quantitative

vascular information can be obtained non-invasively. Hyperspectral imaging has been used to quantify hemoglobin oxygen saturation *in vivo* by collecting absorption images at multiple wavelengths and fitting the resulting absorption curve at each pixel to oxy- and deoxyhemoglobin spectra (Fig. 2.2) using a modified version of Beer's Law [26-28]. It has been successfully applied to map local tissue oxygenation in preclinical tumor models [27], mouse brain [26], and in the feet of diabetic patients [78]. Point-based optical spectroscopy methods have previously been employed to probe hemoglobin oxygen saturation *in vivo*, although these methods do not provide spatial mapping, and results are typically reported as a ratio of the ischemic to control limb rather than absolute values [23, 65]. Hyperspectral imaging overcomes the limitations of other methods for measuring tissue oxygenation discussed previously and provides a robust, quantitative, spatially-resolved measurement. Its resolution may be optimized for a given application through system configuration (CCD with camera lens versus microscope-mounted camera with a magnifying objective). Furthermore, hyperspectral imaging is non-invasive and does not require contrast agents or contact with the tissue, which allows for repeated *in vivo* measurements over a time course of ischemic recovery.

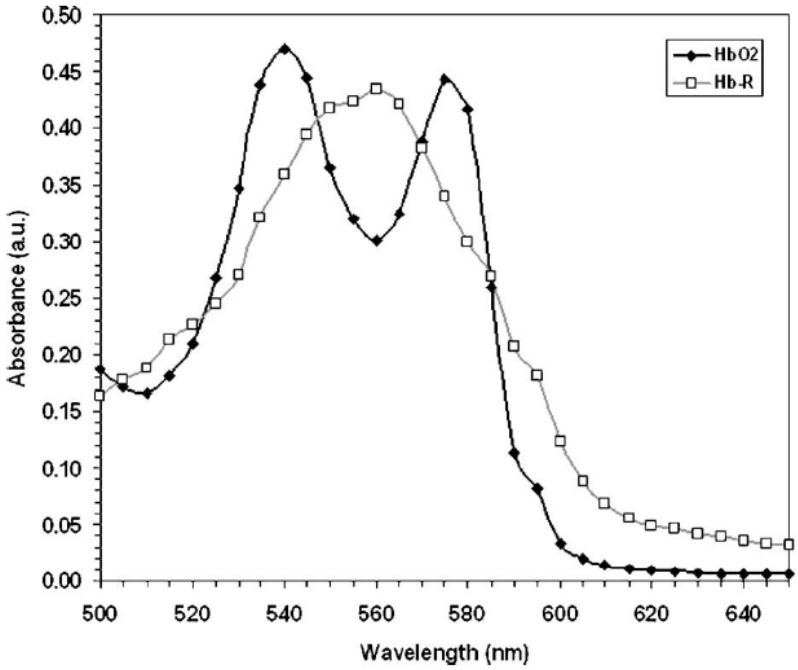

Figure 2.2: Absorbance spectra of oxygenated and deoxygenated hemoglobin for wavelength range used for hyperspectral imaging [27].

2.5 Optical Coherence Tomography

Optical coherence tomography (OCT) is a 3D optical imaging technique that can non-destructively resolve structures in tissue at cellular-level resolution with imaging depths of ~1-3 mm [29, 30]. Cross sectional images are acquired by resolving the difference in path lengths between reflecting and scattering sites in the sample and that of a reference arm using a Michelson interferometer. The speed of OCT allows for fast acquisition of image volumes (~2x2x2 mm volume in as little as 12 seconds) [79]. Doppler OCT, a functional extension of OCT, images microvessel networks and blood velocities in 3D [31, 32] in humans [33, 34] and in preclinical models [35-38]. Doppler shifts arising from motion in the sample (i.e. flowing red blood cells) are detected through phase-sensitive detection of interference between the probe and reference beam [32]. Several quantitative endpoints can be extracted from a Doppler OCT image,

including the velocity profile across the center of a vessel, the blood flow (a function of the mean velocity and vessel diameter), and a vascular index in which the fraction of pixels with a Doppler signal greater than a designated threshold is computed. Speckle variance OCT is another extension of OCT, and it is advantageous for visualizing blood vessel morphology in volume scans collected with OCT since it is independent of the angle of blood flow relative to the imaging beam (unlike Doppler OCT). To generate speckle variance images, repeated images of the same location are acquired and the variance between repeated scans is computed. Fluid motion, i.e. blood flow, causes the speckle variance to be greater within blood vessels than in the surrounding stationary tissue, permitting visualization of vascular morphology in three dimensions or as a two dimensional projection of all of the vessels contained within a volume.

With its combination of speed, resolution, field of view, imaging depth, and sensitivity to blood flow, OCT fills a niche for assessing vasculature in the mouse hind limb. Currently, morphological endpoints such as vascular density and vessel size are obtained from post-mortem histology, micro-CT, and angiography techniques in the HLI model. OCT provides the advantage of obtaining these endpoints intravitally with simultaneous acquisition of functional endpoints such as blood flow. This facilitates a better understanding of structure-function relationships and enables longitudinal measurements of these endpoints within individual mice.

2.6 Novel Therapeutic Strategies

Previous preclinical studies have demonstrated that animals with type 1 diabetes have an impaired vascular response to ischemia [43-45] and that decreasing oxidative stress improves post-ischemic neovascularization [43, 44]. Therefore, the work in this dissertation is focused on targeting oxidative stress locally in the ischemic hind limb in an effort to improve recovery of vascular function. Several strategies have been used to deliver hydrophobic antioxidant and anti-

inflammatory drugs, such as the molecule curcumin, to target oxidative stress, including hydrogels [80], exosomes [81], and stimuli-responsive nanoparticles [82]. Microparticles composed of biodegradable polymers have also been used to create local depots for drug delivery [83], but the particles are typically based on poly(lactic-co-glycolic acid) (PLGA) which is non-specifically degraded by hydrolysis. Furthermore, the byproducts of PLGA degradation are acidic and can exacerbate local inflammation [84], leading to autocatalytic degradation and an uncontrolled drug release profile [85].

An alternative to PLGA-based particles is poly(propylene sulfide) (PPS), which undergoes a transition from a hydrophobic state that efficiently encapsulates hydrophobic drugs, to more hydrophilic poly(propylene sulfoxide) and poly(propylene sulfone) upon exposure to reactive oxygen species (ROS). This transition to a water soluble phase permits the release of encapsulated drug from microparticles only when ROS are locally present. In contrast to PLGA, PPS provides environmentally-responsive release in the presence of oxidative stress, which is expected to be excessive in the context of hyperglycemia. Oxidation-responsive polymersomes [86], nanoparticles [87, 88], micelles [89, 90], and hydrogels [49] have previously been applied, but prior to our work [91] there was no example of micron-scale particles that are more effectively retained at the tissue site to generate a stable, local depot for sustained, oxidation-responsive, on demand delivery. Therefore, we have developed a PPS-based microparticle system for encapsulation of anti-inflammatory and antioxidant drugs for local delivery to the ischemic hind limb in diabetic mice. This system leverages locally-elevated ROS levels for environmentally-responsive release, and the ROS-scavenging ability of PPS itself to enhance the therapeutic effect of the microparticle cargo [91]. This system has been tested by our group in a model of diabetic PAD in the work described in Chapters 5 and 6 of this dissertation.

CHAPTER 3

QUANTITATIVE OPTICAL IMAGING OF VASCULAR RESPONSE IN VIVO IN A MODEL OF PERIPHERAL ARTERIAL DISEASE

Aim 1: Develop and validate OCT and hyperspectral imaging methods for imaging vascular morphology and function in the HLI model

Text for Chapter 3 taken from:

Poole KM, Tucker-Schwartz JM, Sit WW, Walsh AJ, Duvall CL, Skala MC. Quantitative optical imaging of vascular response in vivo in a model of peripheral arterial disease. American Journal of Physiology – Heart and Circulatory Physiology. 2013; 305(8):H1168-H1180

3.1 Abstract

The mouse hind limb ischemia (HLI) model is well established for studying collateral vessel formation and testing therapies for peripheral arterial disease, but there is a lack of quantitative techniques for intravitally analyzing blood vessel structure and function. To address this need, non-invasive, quantitative optical imaging techniques were developed to assess the time-course of recovery in the mouse HLI model. Hyperspectral imaging and optical coherence tomography (OCT) were used to non-invasively image hemoglobin oxygen saturation and microvessel morphology plus blood flow, respectively, in the anesthetized mouse after induction of HLI. Hyperspectral imaging detected significant increases in hemoglobin saturation in the ischemic paw as early as 3 days after femoral artery ligation ($p<0.01$), and significant increases in distal blood flow were first detected with OCT 14 days post-surgery ($p<0.01$). Intravital OCT images of the adductor muscle vasculature revealed corkscrew collateral vessels characteristic of the arteriogenic response to HLI. The hyperspectral imaging and OCT data significantly correlated with each other and with laser Doppler perfusion imaging (LDPI) and tissue oxygenation sensor data ($p<0.01$). However, OCT measurements acquired depth-resolved information and revealed more sustained flow deficits following surgery that may be masked by

more superficial measurements (LDPI, hyperspectral imaging). Therefore, intravital OCT may provide a robust biomarker for the late stages of ischemic limb recovery. This work validates non-invasive acquisition of both functional and morphological data with hyperspectral imaging and OCT. Together, these techniques provide cardiovascular researchers an unprecedented and comprehensive view of the temporal dynamics of HLI recovery in living mice.

3.2 Introduction

Peripheral arterial disease (PAD) affects an estimated 8 million Americans and is associated with increased risk of myocardial infarction, stroke, and reduced quality of life [1-3]. Development of novel PAD treatments that are less invasive and more effective than the current standard of care is a significant focus within basic and clinical cardiovascular research. Although promising results from preclinical studies have justified translation of pro-angiogenic therapies, recent clinical trials have yielded only mildly-encouraging, insignificant trends toward improvement in secondary endpoints [6-10]. There are several factors that may contribute to the disparity between successful preclinical studies and unsuccessful clinical trials. For example, novel therapeutic strategies are often evaluated with the mouse hind limb ischemia (HLI) model [11] in young and healthy animals, rather than in more relevant preclinical models (e.g. aged, diabetic, hypertensive mice) that are more time- and cost-intensive to implement [6]. Preclinical models are also typically assessed only in the early stages of HLI recovery, and very few experimental designs include time points to assess long-term stability of therapeutically-stimulated neovasculature. However, this is a myopic strategy, as it has been recently shown that therapeutic angiogenesis treatments can induce unstable vessels that regress after cessation of treatment. Additionally, late-stage regression of vascular responses that occur immediately following induction of HLI is particularly prevalent in the challenged setting of diabetes [12, 13].

A key limitation to the use of more relevant models and carrying out more thorough temporal analyses during preclinical testing of pro-angiogenic therapies is the lack of quantitative, non-invasive techniques to monitor relevant physiological endpoints (e.g. microvascular density and perfusion, blood velocity, blood oxygenation) longitudinally in the same animal. Currently, it is standard to utilize a combination of intravital methods such as laser Doppler perfusion imaging (LDPI) [11, 23] and MRI angiography [77], and post-mortem methods such as microcomputed tomography (micro-CT) [21, 22, 92] and histology [23] to study the effects of pro-angiogenic therapies over time. With this toolset, numerous cohorts of mice as well as access to and expertise in using multiple complementary instruments are required to complete a comprehensive, longitudinal analysis of the vascular response. This makes preclinical studies expensive and time-consuming. Providing the research community with enabling technologies for robust, standardized, and longitudinal measurements would catalyze new discoveries through better elucidation of the angiogenesis and arteriogenesis processes, more rapid screening of new therapeutic agents, and accelerating the engineering of delivery systems [24, 25].

The objective of this study was to fulfill this unmet need through development and validation of an optical imaging approach that combines hyperspectral imaging with optical coherence tomography (OCT) to intravitally quantify blood oxygenation as well as vascular morphology and function as metrics of mouse ischemic limb recovery. Hyperspectral imaging can noninvasively provide superficial, spatially-resolved maps of the hemoglobin oxygen saturation *in vivo* [27]. This technique has never been used to assess preclinical models of HLI, but it has been successfully applied for other applications in mice [26, 27] and for assessment of blood circulation in diabetic patients [78]. OCT is a complementary optical method that is ideal

for obtaining structural and functional endpoints of the microvasculature over time. This three-dimensional (3-D) imaging technique can non-destructively visualize structural features in tissue at cellular-level resolution with imaging depths of ~1-3 mm [29, 30]. The speed of OCT allows for image volumes to be collected quickly (~2x2x2 mm volume in as little as 12 seconds) [79]. Doppler OCT, a functional extension of OCT, images microvessel networks and blood velocities in 3-D [31, 32] in humans [33, 34] and in preclinical models [35-38].

In this study, a combination of hyperspectral imaging and OCT was utilized to quantitatively and longitudinally assess parameters related to HLI recovery. Hyperspectral data were used to quantify recovery of blood oxygenation at a site distal to femoral artery obstruction (paw). Doppler OCT techniques were applied to image formation of collateral vessels that bypass the site of arterial blockage and to measure restoration of blood flow in the femoral artery distal to the ligation sites. Together, hyperspectral imaging and OCT enable non-invasive acquisition of both functional and morphological measurements of recovery in the HLI model, providing new insight into the dynamics of vascular remodeling, perfusion, and oxygen delivery at multiple tissue depths and anatomical locations. The combined application of these non-invasive optical imaging modalities provides researchers with a new toolset to quantitatively and intravitally evaluate recovery from HLI, enabling more efficient preclinical development of improved PAD therapies.

3.3 Methods

3.3.1 Animals

Male, 8-10 week-old A/J mice (Jackson Laboratories) were used in these studies. The animals were fed a standard chow diet ad libitum and had free access to water. All protocols were approved by the Institutional Animal Care and Use Committee of Vanderbilt University

and done in accordance with the National Institutes of Health *Guide for the Care and Use of Laboratory Animals*.

3.3.2 Hind limb ischemia model

Hind limb ischemia was surgically induced in 20 mice according to the well-established model of femoral artery ligation and transection [11, 67, 93]. Surgery was carried out under 1.5-2.5% isoflurane anesthesia with the mice maintained at normal body temperature. After subcutaneous administration of pre-operative analgesia (ketoprofen, 10 mg/kg) and removal of hair, the surgical site was thoroughly cleansed with alternating iodine and chlorhexidine scrubs. A 5-mm unilateral incision was then made over the right medial thigh of the mouse. The femoral artery and vein were dissected away from the femoral nerve and were ligated with 6-0 silk sutures at two locations: [1] immediately distal to the origins of the epigastric artery and deep branch of the femoral artery and [2] approximately 2 mm distal to the first ligation, proximal to the origin of the nearest distal branch. The artery and vein were transected between the two ligations, leaving a gap of 2-3 mm. The wound was irrigated with sterile saline and the incision was closed with interrupted 5-0 nylon sutures. The contralateral limb served as the control for each animal. Analgesia (ketoprofen, 5-10 mg/kg) was administered subcutaneously every 18-24 hours post-operatively for 72 hours or until animals exhibited normal appearance and behavior.

3.3.3 Hyperspectral imaging system

Two-dimensional diffuse reflectance images were collected with a 200 W halogen lamp coupled into a 10-mm core diameter liquid light guide for epi-illumination. The collection head consisted of a Varispec VIS-20 liquid-crystal tunable filter (LCTF) for bandlimited optical filtering (CRI, Inc.), a variable focal length (f = 28-80 mm) camera lens (Nikon), and a 512 x 512 pixel PhotonMax CCD camera (Princeton Instruments), resulting in a sampling density of

58 μm (schematic in Fig. 3.1A). The LCTF tuning, CCD camera communication, shutter control, and data handling were controlled with a custom C-based computer program with graphic user interface controls from the Fast Light Toolkit [94].

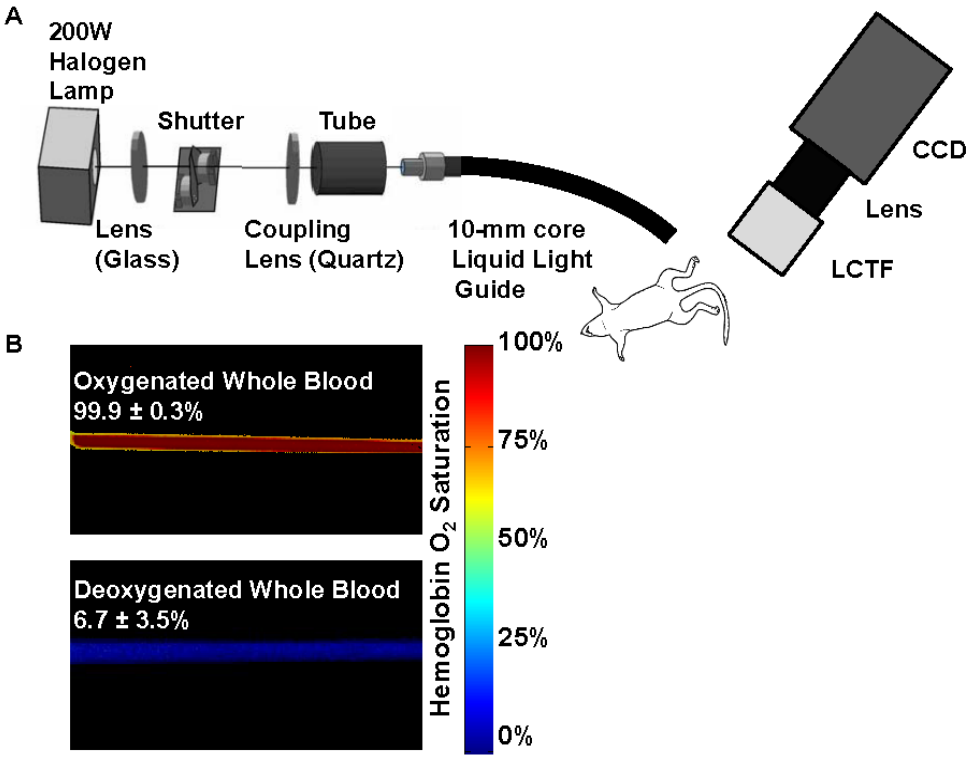

Figure 3.1: Hyperspectral imaging system. (A) Hyperspectral system for diffuse reflectance imaging. White light from the halogen lamp is coupled into a liquid light guide for illumination of the footpads. Specific wavelengths are collected with a liquid crystal tunable filter (LCTF) mounted on the end of a variable focal length (f = 28-80 mm) camera lens and a 512 x 512 pixel CCD camera. (B) Hyperspectral quantification of hemoglobin oxygen saturation was validated in vitro in glass capillary tubes with whole blood diluted with phosphate-buffered saline at pH 7.4.

3.3.4 Hyperspectral imaging validation

To obtain calibrated hemoglobin absorption spectra for the hyperspectral imaging system, oxyhemoglobin and deoxyhemoglobin solutions were prepared from red blood cells obtained from mouse whole blood collected from anesthetized mice via cardiac puncture with a heparinized needle. After lysis of the red blood cells, the hemolysate was diluted 1:10 with Dulbecco's phosphate-buffered saline (DPBS, GIBCO). An aliquot of the solution was inverted repeatedly in room air to prepare an oxygenated hemoglobin solution, and a deoxygenated hemoglobin solution was prepared by adding 5% wt/vol sodium dithionite (Sigma-Aldrich) to a separate aliquot. Glass capillary tubes with an inner diameter of 1 mm were filled with the oxygenated and deoxygenated hemoglobin solutions, sealed on the ends, and submerged in index-matching immersion oil on a glass slide. A diffuse reflectance standard (Spectralon) was placed below the glass slide to provide total reflection in areas where light was not absorbed by hemoglobin. The measured spectra for oxyhemoglobin and deoxyhemoglobin were corrected for the dark offset and the lamp spectrum. Repeated measures of oxy- and deoxyhemoglobin solutions yielded similar spectra (n=3). These calibrated hemoglobin absorption spectra were then used to fit measured absorption spectra for mouse whole blood at 100% and 0% (treated with 5% wt/vol sodium dithionite) oxygenation *in vitro* to validate quantification of hemoglobin oxygen saturation. Blood gas measurements were performed on parallel samples prepared in the same way to verify that the pO_2 values in each solution were sufficiently high or low enough to assume the mouse whole blood was 100% or 0% oxygenated, respectively. Hemoglobin saturation images for whole blood were calculated from hyperspectral data (500 to 620 nm in 10 nm increments) using a model derived from an extension of the Beer-Lambert law [26-28]. The model calculates the hemoglobin saturation in each pixel by fitting the measured spectra to the

calibrated spectra for oxy- and deoxy-hemoglobin, using linear least-squares regression [26-28]. Oxygenated and deoxygenated hemoglobin were assumed to be the dominant factors contributing to absorption in this model. The measured saturation of 100% and 0% oxygenated blood was 99.9% ± 0.3% and 6.7% ± 3.5%, respectively (Fig. 3.1B) thus validating the accuracy of the system.

3.3.5 Hyperspectral imaging

Immediately following surgery (day 0) and at 3, 7, 14 and 21 days post-surgery, control and ischemic footpads were imaged non-invasively through the skin with hyperspectral imaging (500 to 620 nm in 10 nm increments). Hyperspectral images can be collected at any location, but in this study the footpads were selected as the site of interest since the most severe ischemia/hypoxia occurs in the distal limb in this model [67]. All imaging was carried out under 1-2% isoflurane anesthesia with the mice maintained at normal body temperature with a circulating water heating pad. Anesthesia was delivered with 21% oxygen rather than 100% oxygen to avoid artificial elevation of normal hemoglobin saturation. Measurements of the dark offset and reflectance from a diffuse reflectance standard (Spectralon) were made before each imaging session. Hemoglobin saturation images were calculated as described above, providing 2-D spatial maps of hemoglobin oxygen saturation that have not been previously obtained in this model. For *in vivo* image processing, the effective attenuation coefficient (Eq. 1) for skin at each wavelength was incorporated into a modified version of the Beer-Lambert law (Eq. 2) to account for attenuation due to non-hemoglobin absorption and scattering effects [26-28]:

$$\mu_{eff} = \sqrt{3\mu_a(\mu_a + \mu'_s)} \quad \text{(Eq. 1)}$$

$$A(\lambda) = b_0 + b_1\mu_{eff}(\lambda) + \sum_i \varepsilon_i(\lambda)C_i \quad \text{(Eq. 2)}$$

where μ_{eff} is the effective attenuation coefficient calculated for representative skin optical properties (absorption coefficient μ_a and reduced scattering coefficient μ_s') as a function of wavelength [95], $A(\lambda)$ is the absolute tissue attenuation, b_0 is a constant term accounting for overall changes in signal, b_1 is a free parameter modulating the magnitude of the $\mu_{eff}(\lambda)$ term, $\varepsilon_i(\lambda)$ is the extinction coefficient of the i^{th} absorber as a function of wavelength (in this case, oxygenated and deoxygenated hemoglobin), and C_i is a composite term that is the product of the concentration and path length of light attenuated by each absorber [28]. For quantitative analysis of hemoglobin saturation images, regions of interest (ROI) in each image were defined by outlining the footpads using ImageJ software. Absolute hemoglobin saturation values were quantified for each footpad by averaging the values for all pixels contained with the ROI. The ratio of the hemoglobin saturation in the ischemic footpad to that in the control footpad was also computed to serve as an endpoint that is analogous to the quantification typically done with LDPI.

3.3.6 Laser Doppler perfusion imaging

Following hyperspectral imaging, perfusion in the footpads was measured by LDPI [11, 23] (Perimed) at 0, 3, 7, 14 and 21 days post-surgery under isoflurane anesthesia and normal body temperature maintained with a circulating water heating pad. The ambient light was consistent across all imaging days. For analysis of perfusion data sets, ROIs in each image were defined by outlining the footpads. Perfusion values were obtained for each footpad by averaging the values for all pixels contained with the ROI. Because LDPI is an intrinsically semi-quantitative and relative measurement, perfusion images were quantified as a ratio of the average perfusion value of the ischemic footpad to that of the control footpad.

3.3.7 OxyLite pO_2 measurements

Tissue oxygen tension (pO_2) was measured in the footpads of 5 mice under isoflurane anesthesia and maintained at normal body temperature at 0, 3, 7, 14 and 20 days post-surgery using the commercially-available fiber-optic OxyLite (Oxford Optronix) tissue oxygenation sensor. To measure oxygen tension, the probe tip was inserted into the superficial region of the footpad at a depth of approximately 1 mm with a needle, and pulses of LED light were transmitted along the fiber optic probe to excite a platinum-based fluorophore enclosed within a silicone matrix at the tip. The fluorescent light is quenched in the presence of oxygen and the instrument detects the fluorescence lifetime, which is inversely proportional to the concentration of dissolved oxygen. This value is used to calculate the absolute value of pO_2 in mmHg. The OxyLite system simultaneously corrects for temperature effects with an integrated temperature probe that provides the mouse core temperature during measurements. For this study, measurements were taken in two locations on each footpad. After insertion of the probe, the pO_2 reading was allowed to stabilize for 10-15 minutes. Once the reading stabilized, seven measurements were recorded over 30 seconds to obtain an average pO_2 value. Data were collected from two locations on the footpad and the two values were averaged to provide a single value for each footpad. The pO_2 data were analyzed as both absolute values in mmHg and as ratios of the ischemic footpad to the control footpad.

3.3.8 Optical coherence tomography

A spectral domain OCT system (Bioptigen) with 25 μm lateral resolution and an 860 nm center wavelength, 51 nm bandwidth superluminescent diode (SLD) source (6.4 μm axial resolution in air) was used (Fig. 3.2A). The SLD light is fiber coupled and split between a reference mirror and the sample arm using a 50/50 fiber coupler, while X-Y galvos in the sample

arm perform lateral scanning. An aiming beam (642 nm) was also used to facilitate positioning of the hind limb at the sample arm of the OCT system. Returning interference light is sent through an 860 nm center wavelength circulator to a spectrometer with a 2048 pixel line scan CCD (Atmel - AViiVA SM2). Prior to *in vivo* imaging of blood flow, Doppler OCT flow rate measurements were validated in an Intralipid flow phantom controlled with a syringe pump (Fig. 3.2B). The displacement sensitivity of the OCT system is ~6 nm, resulting in theoretical minimum and maximum detectable velocities [96, 97] of 0.08 mm/s and 11.6 mm/s, respectively, for an 80-µs integration time and a range of Doppler angles. This sensitivity is in line with other OCT blood flow detection techniques reported in literature [39, 97].

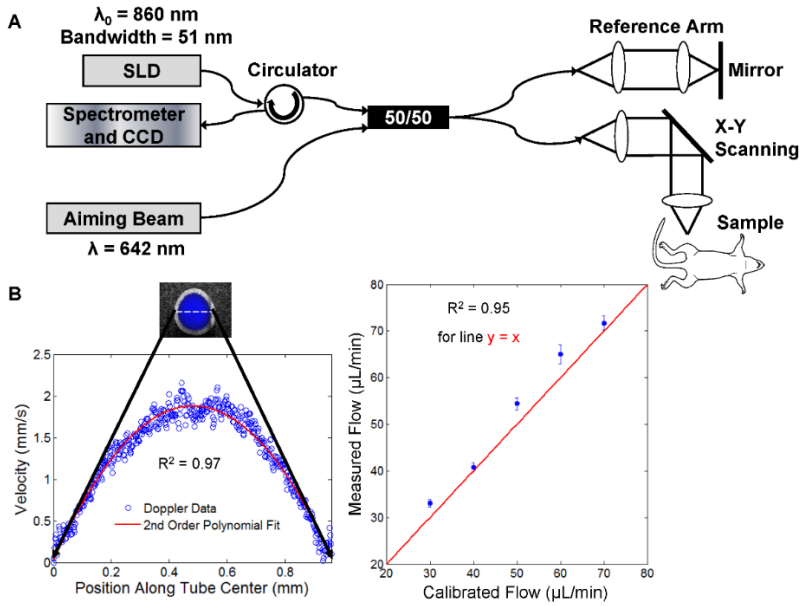

Figure 3.2: OCT system. (A) The spectral domain OCT system has a superluminescent diode (SLD) source centered at 860 nm with a 51 nm bandwidth. (B) Measurement of flow with Doppler OCT was validated with an Intralipid phantom for a range of flows controlled with a syringe pump. Cross sectional flow profiles were fit to a 2nd-order polynomial, assuming parabolic flow. The Doppler OCT-measured flow was calculated using the average velocity (half of maximum velocity) and the cross sectional area of the capillary tube.

For the hind limb ischemia study, two-dimensional B-scans and three-dimensional C-scan volumes of Doppler OCT data were collected from two locations on each hind limb (ischemic and contralateral) for mice (n=8) on days 0, 3, 7, 14 and 21 after surgery under isoflurane anesthesia and normal body temperature. During imaging, a thin layer of water-based index matching agent containing glycerin was applied to the skin and a glass cover slip was secured over the area to reduce bulk motion. Doppler B-scans spanning 4 mm in length were acquired with an 80 μs integration time per A-line (axial scan), 800 A-lines/B-scan (cross-sectional image), and a Doppler number of 8 (n=9 repeated A-lines), resulting in a frame rate of 1.7 frames/second for Doppler B-scans. Repeated B-scans were collected in each area to allow for temporal averaging and reduction in noise. For 3 mm by 3 mm speckle variance OCT volume scans ("C-scans"), an 80 μs integration time per A-line, 200 A-lines/B-scan, 200 B-scans/C-scan, and a Doppler number of 6 (n=7 repeated A-lines) were used, resulting in a total volume acquisition time of 22.4 seconds. OCT was evaluated in regions located proximally on the limb relative to the hyperspectral imaging site, because the adductor muscle of the thigh is where the arteriogenic collateral vessels form that are considered to be the most efficient mechanism for restoring flow to the limb [23]. The first imaging site (Area 1) contained segments of the femoral artery and vein distal to the ligation site and proximal to the popliteal/saphenous bifurcation. This region was selected to monitor restoration of blood flow over time as a biomarker for formation of functional vascular anastomoses that bypass the more proximal site of femoral artery obstruction. The second area (Area 2) was located in the adductor muscle region medial to the site of femoral artery resection and was chosen to directly monitor changes in the morphology and blood flow signal in anastomotic collateral vessels. Each limb was permanently marked with tattoo ink to provide fiducial markers on the skin, facilitating alignment of the OCT

beam at the defined areas at each time point. All OCT imaging was performed non-invasively through the skin, and longitudinal measurements were taken from the same set of mice, which is unique relative to any other intravital OCT imaging previously accomplished with the HLI model.

Doppler OCT B-scans containing cross-sectional images of the femoral artery and vein were processed to reduce speckle noise and bulk motion artifact. Phase noise due to signal fall-off with depth in the tissue was excluded by a threshold in the corresponding structural image, and the bulk motion artifact due to respiration was reduced using a histogram-based correction method [98]. The resulting tissue depth for which data was included for further processing was 0.92 ± 0.11 mm (mean ± SD) from the surface of the skin. Following this processing, the repeated B-scans from the same location were averaged temporally, and then a Doppler signal threshold was computed for each limb at each time point from a region of static tissue (skin) to further separate blood flow detection from background noise. Pixels with a Doppler signal greater than the threshold were summed across the cross-sectional images and divided by the total pixel area to define a vascular index for blood flow (including all arterial and venous vessels combined) in the detected vasculature [99]. The vascular index ratio is defined as the ratio of the vascular index in the ischemic limb to that in the control limb. It should be noted that that because Doppler OCT measures the velocity component that is parallel to the incident laser beam, the vascular index is Doppler-angle dependent. It is possible to underestimate total flow with this angle-dependent measurement, and vessels with high velocity can go undetected. We hypothesized that the femoral artery would have the highest flow in these images, and because Doppler signal was observed throughout the femoral artery in all of the quantified images, we do not believe that angle dependency had a significant effect on our flow index calculation.

In order to visualize projection images of the vasculature at the distal femoral artery and adductor muscle regions, volume data sets were processed with a speckle variance technique that computes the variance in each pixel over seven repeated A-lines at each lateral position [39]. The resulting speckle variance images represent OCT flow signal for perfused vessels within the imaged volume. Noise due to signal fall-off was excluded by thresholding the corresponding structural images to create a mask, and an average signal projection over the depth (approximately 1 mm) of the speckle variance OCT data was used to visualize all vessels present in the volume.

3.3.9 Correlations between techniques

The relationships between LDPI and our noninvasive optical techniques were tested with the Pearson's correlation coefficient [100] for the pooled data consisting of LDPI, hyperspectral imaging, and OCT measurements performed on the same animals, allowing for robust comparisons between techniques. Because the OxyLite probe was introduced with a needle, a cutaneous wound was created that affected LDPI and hyperspectral imaging data. Thus, a separate cohort of mice was used to obtain OxyLite pO_2 measurements for comparison, and mean values were used to obtain the Pearson's correlation coefficient between hemoglobin oxygen saturation measured with hyperspectral imaging and tissue pO_2 measured with the OxyLite probe.

3.3.10 Statistical analysis

All data are presented as mean ± SEM. Paired Wilcoxon Signed-Rank statistics were computed using MATLAB software (MathWorks) for comparisons between ischemic and control limb measurements within each animal for each time point. The effect of time post-surgery on the response variables within each animal was tested with the paired Wilcoxon

Signed-Rank test followed by a Bonferroni correction for multiple comparisons. Pearson's correlation coefficients were used to compare hyperspectral imaging and OCT endpoints to each other and to LDPI and OxyLite pO_2 endpoints. $P<0.05$ was interpreted as significant.

3.4 Results

Measures of vascular structure and function following induction of HLI were obtained using optical imaging methods (hyperspectral imaging and optical coherence tomography) and were compared to traditional methods of evaluating the mouse HLI model (laser Doppler perfusion imaging and tissue oxygen tension).

3.4.1 LDPI measurement of paw perfusion

LDPI-based perfusion in the footpads was analyzed in the same animals for which hyperspectral imaging and OCT data were collected. The ischemic-to-control perfusion ratio was severely reduced at day 0 as shown by a representative perfusion image (Fig. 3.3A), then increased significantly beginning at day 7 until perfusion was completely recovered in the ischemic limb by day 21 (Fig. 3.3B). Significant increases in the ratio were observed between days 3 and 7, 7 and 14, and 14 and 21 post-surgery ($p<0.05$).

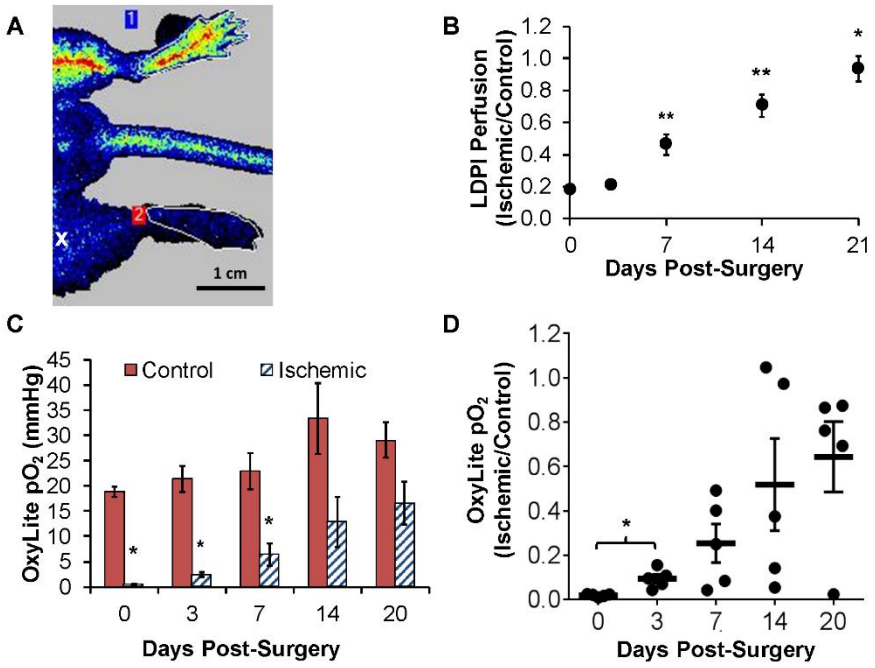

Figure 3.3: Measurements with LDPI and the OxyLite tissue oxygen tension sensor confirm time course of recovery in ischemic limb. (A) Representative LDPI image of ischemic (bottom) and control (top) footpads immediately post-surgery. The white "x" indicates the approximate location of the distal ligation site. (B) LDPI ratios demonstrate full recovery of perfusion in the ischemic footpad relative to the control footpad by day 21 (mean ± SEM with n=15). (C) Absolute pO_2 values from control and ischemic footpads measured with the OxyLite system (mean ± SEM with n=5). (D) Individual animal ratios (ischemic pO_2 normalized to mean control pO_2 for each animal) plotted with lines representing mean ratio ± SEM at each time point. * corresponds to a one-sided $p<0.05$, and ** corresponds to $p<0.01$ as determined by a Wilcoxon Signed-Rank test (B-D) followed by a Bonferroni correction for multiple comparisons (B, D) with respect to the corresponding control measurement (C) or the preceding time point (B, D).

3.4.2 Fiber-optic probe sensor measurement of paw tissue oxygen tension

Tissue pO_2 in the footpads measured with the OxyLite sensor showed significant differences between the control and ischemic footpads on days 0 through 7 (Fig. 3.3C). However, there was large standard deviation in the ischemic-to-control footpad ratio on days 7 through 20 (Fig. 3.3D). Figure 3.4 illustrates the variability between control footpad measurements taken at two different locations in each foot and also highlights the lack of precision of the OxyLite system to measure normoxic pO_2 levels (greater than 10 mmHg). Because the dynamic range of the OxyLite is better aligned with measurement of pO_2 in ischemic tissues, the data recorded in the ischemic footpad at early time points (days 0 and 3) was less variable than at later time-points (Fig. 3.4).

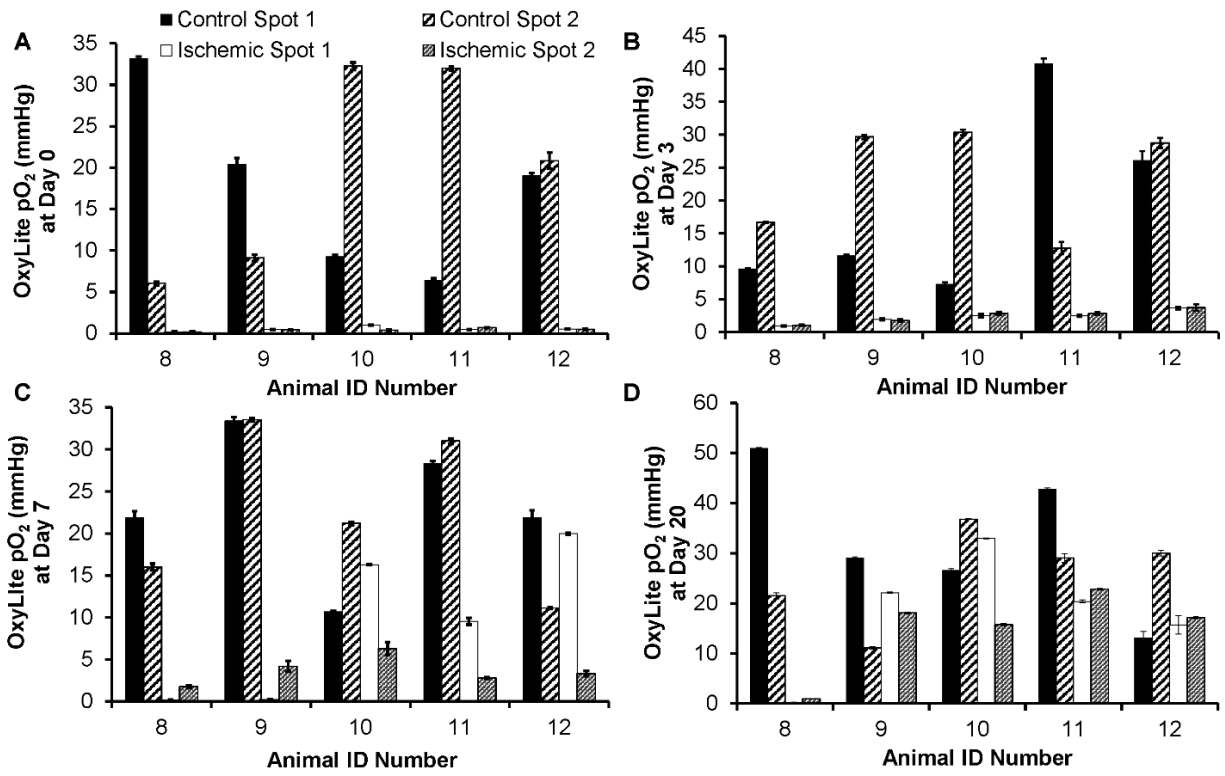

Figure 3.4: OxyLite measurements are variable at normal tissue pO_2 levels. OxyLite tissue oxygenation sensor measurements are more precise at low tissue pO_2 and show high spatial variability at normal pO_2 levels. Tissue pO_2 data are shown from each animal for two locations on each footpad at (A) day 0, (B) day 3, (C) day 7 and (D) day 20. Data presented as mean ± SDM of 7 readings in each location collected over 30 seconds.

3.4.3 Hyperspectral imaging of paw hemoglobin oxygen saturation

We used an LCTF-based hyperspectral imaging system to non-invasively acquire quantitative hemoglobin saturation measurements on the hind feet of mice after unilateral induction of ischemia. This method provides an absolute measurement and yields a value integrated over the entire footpad, unlike semi-quantitative LDPI and invasive probe-based pO_2 techniques. Analysis of hemoglobin saturation images (representative images, Fig. 3.5A-B)

revealed a significant reduction in oxygenation of the ischemic footpad relative to contralateral controls from day 0 through day 7 post-surgery (Fig. 3.5C). Normalized data (ischemic/control) shows that hemoglobin saturation in the ischemic footpad was reduced to approximately 40% of the control immediately following surgery (Fig. 3.5D) and that the ratio increased significantly at each subsequent time point relative to the prior time point (3 vs. 0, 7 vs. 3, 14 vs. 7, and 21 vs. 14) ($p<0.05$). The hemoglobin saturation ratio fully recovered by day 21. Because hyperspectral imaging acquires a 2-D image rather than a point measurement like the OxyLite system, we were able to obtain the distribution of hemoglobin oxygen saturation across all of the pixels within the footpad in addition to quantifying the mean value over the entire footpad (Fig. 3.6). The distribution peak is shifted toward zero in the ischemic footpad upon induction of ischemia, and the variance (s^2) in hemoglobin saturation values differed significantly between the ischemic and control footpads at days 0 ($p<0.05$), 7 ($p<0.05$), and 14 ($p<0.001$). The distribution of pixel values within hyperspectral images of the ischemic footpad shifts over time and is similar to the control footpad distribution by day 21 ($p=0.096$).

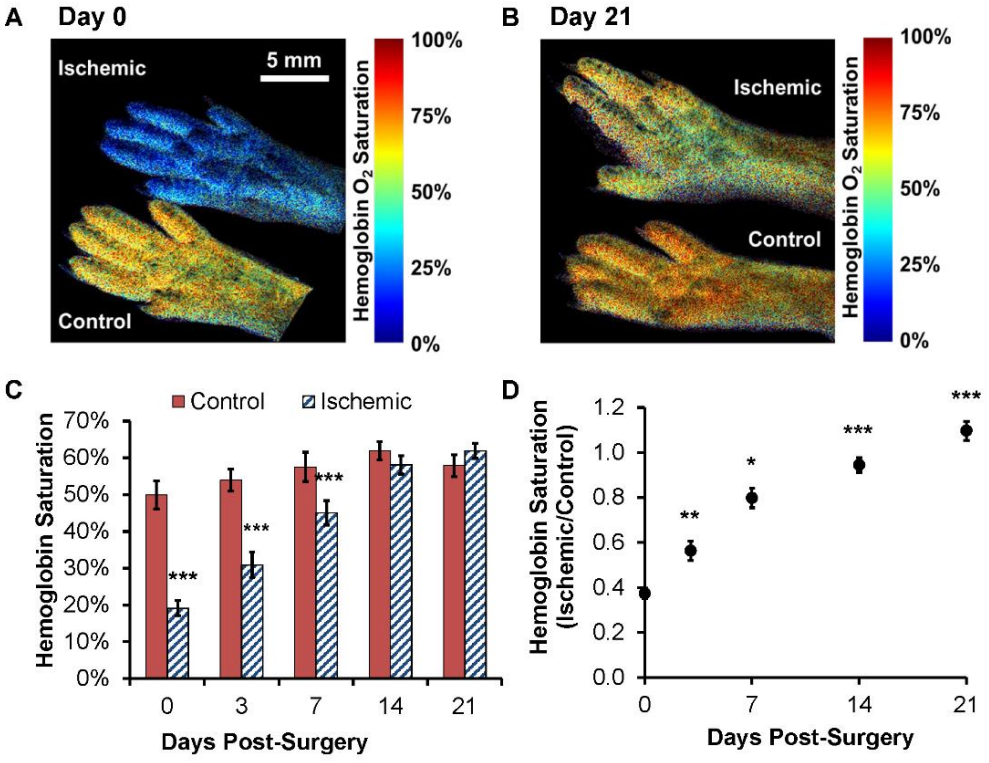

Figure 3.5: Hemoglobin oxygen saturation measured with hyperspectral imaging resolves ischemic recovery in the footpad. Representative hemoglobin saturation images of the ischemic (top) and control (bottom) footpads (A) at day 0 after surgery and (B) at 21 days post-surgery. (C) Absolute hemoglobin saturation was quantified as the mean of all pixels within each footpad. Significant differences existed between the ischemic and control footpads at days 0, 3 and 7. (D) Data normalized to the control footpad demonstrated complete recovery from hypoxia in the ischemic footpad relative to the control footpad with significant increases in the ratio between successive time points. Data presented as mean ± SEM with n=15. * corresponds to $p<0.05$, ** corresponds to $p<0.01$, and * corresponds to $p<0.001$ as determined with a Wilcoxon Signed-Rank test (C-D) and a Bonferroni correction for multiple comparisons (D) with respect to the corresponding control measurement (C) or the preceding time point (D).**

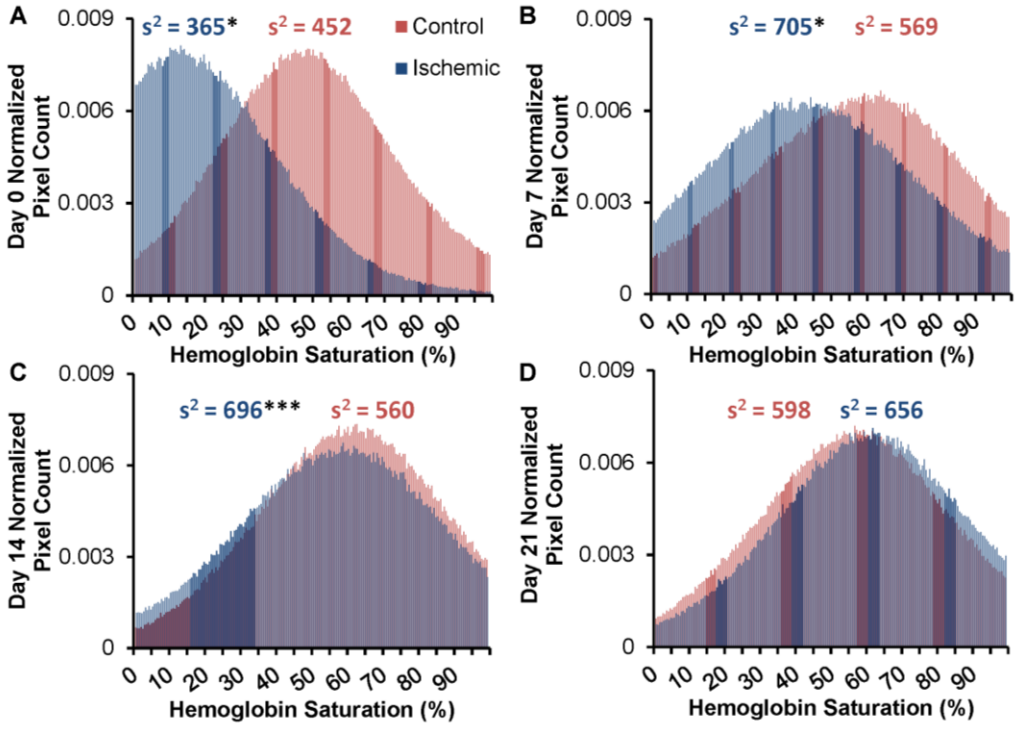

Figure 3.6: Average histograms of hemoglobin oxygen saturation in the control and ischemic footpads show the distribution of hemoglobin saturation over all pixels within the ROIs of all n=15 animals. Histograms of hemoglobin saturation were generated from all pixels within the control and ischemic footpads and normalized to the ROI pixel area at (A) day 0, (B) day 7, (C) day 14 and (D) day 21 post-surgery. The distribution of hemoglobin saturation values is shifted toward zero in the early time points for the ischemic footpad. This is followed by shifting of the peak to overlap with the control footpad data by day 14. The variance of hemoglobin saturation values within each footpad (average of n=15 animals) is indicated by s^2 above each histogram. The variance of the ischemic footpad differed significantly from that of the control footpad at days 0, 7, and 14. * corresponds to $p<0.05$ and * corresponds to $p<0.001$ as determined with a Wilcoxon Signed-Rank test with respect to the corresponding control measurement.**

3.4.4 OCT vascular imaging and blood flow measurement

OCT provides quantitative, three-dimensional, structure-function information that is complementary to the blood oxygenation measurements acquired with hyperspectral imaging. Here, images of newly-recruited collateral vessels in the adductor region (speckle variance OCT) and functional blood flow measurements in the distal femoral artery region (Doppler OCT) were both acquired non-invasively through the skin of the ischemic and control hind limbs.

Average intensity projections of speckle variance OCT images of the ischemic hind limb revealed restoration of blood flow in the femoral artery region distal to the ligation site (Area 1) and visible recruitment of collateral vessels in the adductor region (Area 2) over time (Fig. 3.7). Representative images of Area 1 at day 0 from the control (Fig. 3.7Ai) and ischemic (Fig. 3.7Aii-iv) limbs showed that anatomical images of the vasculature in the control limb could be resolved (Fig. 3.7Ai) and that the OCT flow signal was absent immediately following HLI surgery (Fig. 3.7Aii). Images from the same animal at days 14 and 21 post-surgery showed re-appearance of blood flow in the ischemic limb at this site (Fig. 3.7Aiii-iv). Small pre-existing arterioles were visible in the adductor muscle (Area 2) of both the control and ischemic limbs at day 0 (Fig. 3.7Bi-ii). By day 7, there was evidence of arteriogenic collateral recruitment based on appearance of new, larger vessels with increased OCT flow signal that were more clearly resolved than the small arterioles present in the same region at day 0 in the same animal (Fig. 3.7Biii). Vessels with corkscrew morphology characteristic of remodeling collateral vessels [23] were present at 7 and 14 days post-surgery (arrowheads, Fig. 3.7Biii-iv).

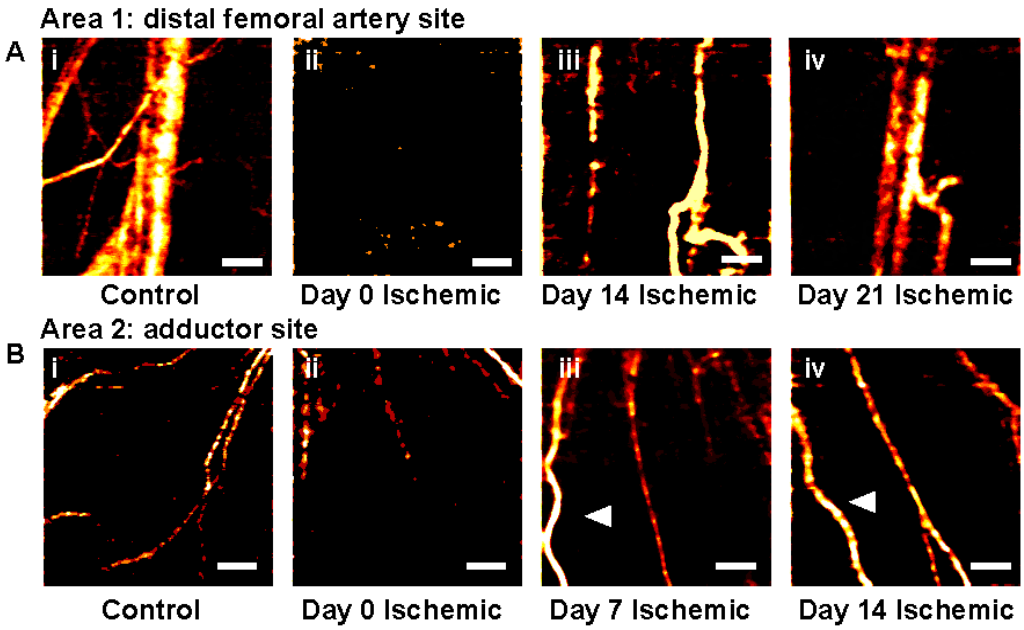

Figure 3.7: Speckle variance OCT volumes non-invasively illustrate reperfusion and collateral vessel formation *in vivo*. (A) Representative speckle variance OCT average intensity projections containing the distal femoral artery and vein in Area 1 (i) in a control limb and in an ischemic limb of the same animal at (ii) day 0, (iii) day 14, and (iv) day 21. (B) Representative speckle variance OCT average intensity projections containing collateral vessels in the adductor muscle in Area 2 (i) in a control limb and in an ischemic limb of one animal at (ii) day 0, (iii) day 7, and (iv) day 14. White arrowheads indicate collateral vessels with corkscrew morphology. All images collected through the skin; scale bars = 500 µm.

Color-coded Doppler OCT images were overlaid onto structural OCT images at day 0 for Area 1 (cross section over femoral artery/vein distal to the site of femoral artery resection and just proximal to the popliteal bifurcation). These images illustrated the presence of perfusion in the femoral artery (red) and vein (blue) in the control limb, while there was no Doppler OCT signal from these vessels in the ischemic limb immediately after surgery (Fig. 3.8A-B). The

corresponding structural OCT image provided confirmation that the vessels were located within the scanned area (Fig. 3.8B). The Doppler OCT vascular index in Area 1, which includes smaller vessels located near the obstructed femoral artery and vein, was reduced to approximately 30% of the contralateral control limb at day 0 (Fig. 3.8D). Recovery of functional blood flow in this region was delayed relative to recovery as measured by hyperspectral imaging and other gold standard methods, showing no significant increase at days 3 or 7 relative to measurements taken immediately post-surgery. However, by weeks 2 and 3 post-surgery, perfusion at this distal site increased significantly in the ischemic limb (Fig. 3.8C-D), with significant increases in the vascular index ratio at days 14 and 21 with respect to the preceding time point ($p<0.01$).

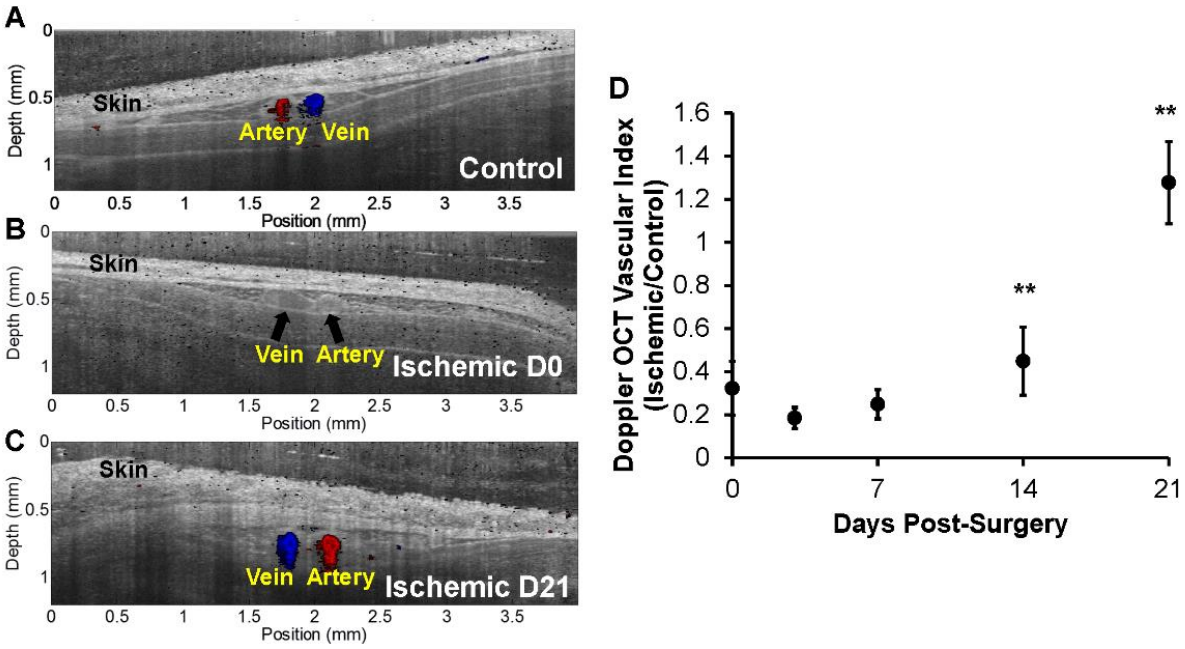

Figure 3.8: Perfusion measured with Doppler OCT resolves ischemic recovery in the hind limb distal to vessel occlusion. (A) Representative Doppler OCT B-scan of distal femoral artery (red) and vein (blue) in Area 1 (see methods) imaged through the skin in a control limb, (B) ischemic limb at day 0 post-surgery with occluded vessels indicated with black arrows, and (C) ischemic limb at day 21 post-surgery. Color Doppler OCT data is overlaid onto corresponding grayscale OCT intensity images. (D) Quantification of perfusion from the Doppler OCT vascular index ratio shows recovery of perfusion in these vessels at weeks 2 and 3 post-surgery. Data presented as mean ± SEM with n=8. ** corresponds to p<0.01.

3.4.5 Correlations between hyperspectral imaging, OCT, and gold standard techniques

The relationships between standard methods and our noninvasive optical techniques were tested across all animals and time-points, in order to define these new optical methods in the context of existing methods used to assess recovery in the mouse HLI model. The hemoglobin oxygen saturation ratio measured with hyperspectral imaging positively correlated with both

LDPI-measured perfusion and OxyLite-measured tissue oxygen tension ratios with Pearson's correlation coefficients (r) of 0.74 and 0.97, respectively (Fig. 3.9A-B). Though the Doppler OCT vascular index ratio appeared to better measure a later stage of recovery relative to the other techniques, it did positively correlate with LDPI perfusion and hemoglobin oxygen saturation ratios with correlation coefficients of 0.63 and 0.56, respectively (Fig. 3.9C-D). All correlations are statistically significant ($p<0.01$). The inter-animal variability observed with each technique is illustrated by plots of the longitudinal responses of individual animals in Figure 3.10.

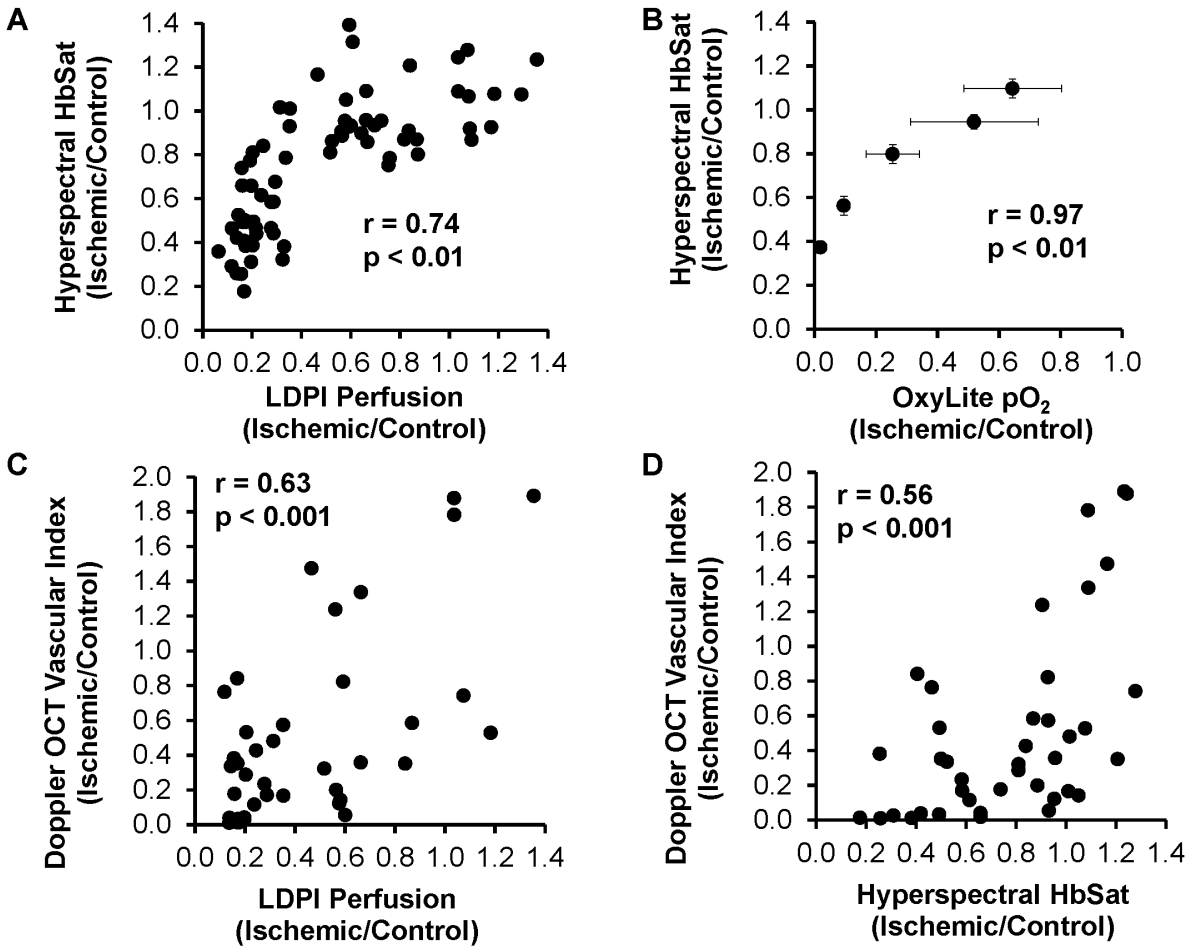

Figure 3.9: Vascular endpoints in the HLI model are positively correlated and exhibit differences in time rate of recovery due to measurement of distinct physiological processes. Correlations between hyperspectral imaging measurement of hemoglobin oxygen saturation (HbSat) and (A) LDPI perfusion and (B) OxyLite pO_2 ratios, and between the Doppler OCT vascular index and (C) LDPI perfusion and (D) HbSat ratios. In (A), (C), and (D) the data include measurements from all mice at all time points. In (B), mean values for each time point are compared since the invasiveness of the OxyLite sensor necessitated the use of a separate cohort of mice. The Pearson correlation coefficients for all four comparisons are significant ($p<0.01$).

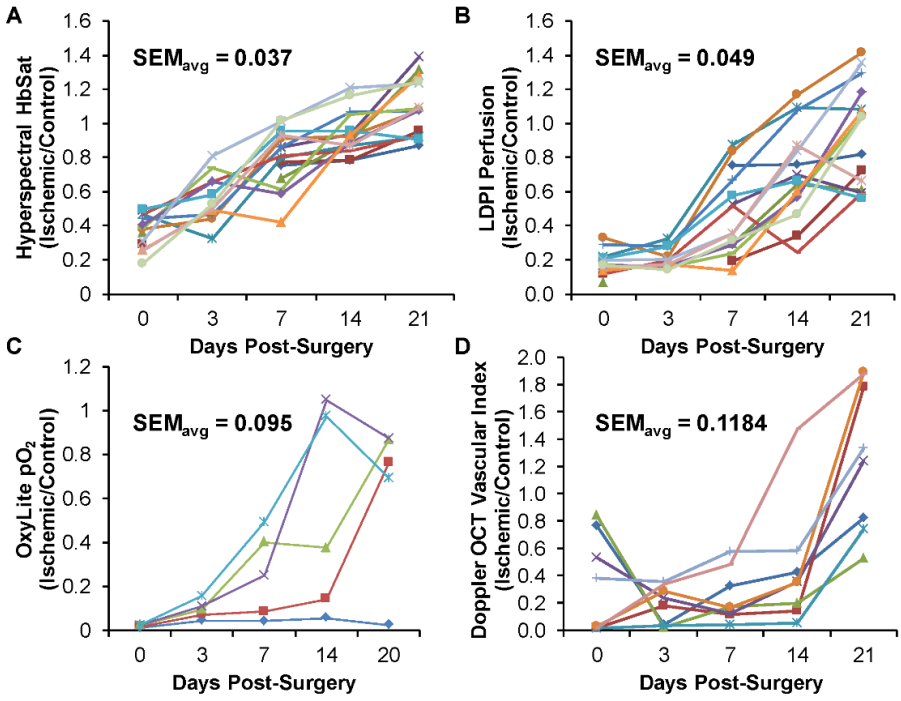

Figure 3.10: Inter-animal variability is smallest in hyperspectral imaging and largest in OxyLite pO_2. Hyperspectral imaging of hemoglobin oxygen saturation shows more consistent trends across all animals measured than both LDPI perfusion and OxyLite pO_2 in this model. (A) Hemoglobin saturation ratio for n=15 animals over 21 days shows a consistent increasing trend. (B) LDPI perfusion ratio for n=15 animals over 21 days shows an increasing trend with high inter-animal variation. (C) OxyLite pO_2 ratio for n=5 animals over 20 days is highly variable and lacks a consistent increasing or decreasing trend across all animals. (D) Doppler OCT vascular index ratios for n=8 animals shows inter-animal variability in the recovery of blood flow through vessels in the distal femoral artery region (Area 1) and a slower temporal response, indicating that the greater imaging depth of OCT provides insight into residual flow deficits not detectable by the superficial measurements obtained with hyperspectral imaging, LDPI, and OxyLite pO_2. This may represent a useful metric for analysis of the later stages of recovery. The average standard error over the time course is indicated by SEMavg for each technique.

3.5 Discussion

The mouse hind limb ischemia model is used extensively for preclinical studies of postnatal blood vessel formation and testing the efficacy of new therapies for PAD, but no single methodology currently used in this model provides multi-functional, quantitative information from the living mouse. The current standard approach, a combination of intravital (LDPI and MRI) and post-mortem (micro-CT, angiography, histology) techniques, to evaluate the vascular response over time is expensive and time consuming. Based on this toolset, researchers are disincentivized against completing more physiologically-relevant and thorough analyses because these techniques require a separate cohort of mice for each time point, time consuming post-mortem tissue preparations, and multiple methodologies for evaluation [6]. Therefore, the ability to identify and quantify robust biomarkers for angiogenesis and arteriogenesis and measure these endpoints repeatedly in a given animal provides valuable longitudinal data to complement traditional endpoints. This could significantly accelerate and improve the development of novel therapeutics for PAD.

The current study validates a new approach that combines hyperspectral imaging and OCT for intravital acquisition of comprehensive vascular structure and function information in the mouse HLI model. Hyperspectral and OCT images from the HLI model revealed previously-inaccessible insights into the dynamic changes of physiological endpoints at different tissue sites. Hemoglobin oxygen saturation and LDPI perfusion, both measured superficially in the footpads, have the strongest correlation within a single cohort of mice (Fig. 3.9A). However, hemoglobin saturation is recovered more rapidly in the first week with a significant increase in the ischemic-to-control ratio at day 3 (Fig. 3.5D). Hemoglobin oxygen saturation is also less severely reduced and recovered more rapidly than tissue pO_2 measured with the OxyLite sensor (Fig. 3.9B). All

three of these endpoints (hemoglobin saturation, pO_2, and LDPI perfusion) were measured superficially in a distal site of ischemia, the footpad, but the temporal differences observed between techniques suggests that they qualify as distinct physiological endpoints rather than being linearly correlated with each other. In addition to correlating with the LDPI and OxyLite pO_2 measurements performed in this study, the absolute hemoglobin oxygen saturation values measured by hyperspectral imaging of the control and ischemic footpads are similar to published data acquired with volume-averaged diffuse optical spectroscopy measures [65].

Hyperspectral imaging overcomes some limitations of current gold standards (LDPI and OxyLite pO_2 measurements). The pO_2 measurement technique was used as a comparison because of its similarity to the hyperspectral imaging endpoint of hemoglobin oxygen saturation, but its invasiveness further limits the potential usefulness of this technique for the HLI model. Interpretation of OxyLite pO_2 measurements is limited by the high inter-animal (Fig. 3.3D, 3.4, and 3.10C) and intra-animal (Fig. 3.4) variability, which is likely attributed to the small sampling area (0.038 mm^2) [101] and decreased accuracy at normoxic pO_2 levels. Our observations of significant variations in pO_2 measurements in tissues at normoxic pO_2 levels with the OxyLite system are aligned with published results [70]. Previous papers have also noted variable pO_2 values with the OxyLite system in hypoxic regions [70]. If the probe tip is placed in a poorly perfused or necrotic environment, it will measure a pO_2 value near 0. Since necrosis and perfusion are not uniform across the entire footpad, measurements in the ischemic footpad may show large variations. In addition to site-to-site variability, another potential source of variability is the exact depth of the measurement. To mitigate these potential variables, the probe was introduced with the same gauge needle each time, insertion into the tissue was halted once the probe tip passed completely through the skin, and measurements from two locations in each

footpad were averaged. The invasiveness of the pO_2 probe required the use of a separate cohort of mice for this endpoint, limiting subsequent correlations to mean pO_2 values rather than individual animal values, because the needle-guided insertion invoked perfusion changes in the footpad unrelated to femoral artery obstruction. In addition, hyperspectral imaging data are more consistent between animals than both LDPI data and single-point measurements of pO_2 (Fig. 3.10A-C). In order to determine whether the variation in control hemoglobin saturation values across multiple time points is due to physiological (rather than instrument) variability, repeated measurements were taken with the instrument on a whole-blood phantom (n=5). The resulting measurements varied by 4% of the mean, while repeated control footpad measurements across multiple days varied by 16% of the mean. The greater variability observed in the control limbs relative to the blood phantom suggests that the variation is largely due to physiological factors such as body temperature, depth of anesthesia, and recovery from surgery, rather than instrument variability. Although both hemoglobin oxygen saturation and LDPI perfusion are sensitive to changes in body temperature, inter-animal variability was lower for the hemoglobin oxygen saturation endpoint at later time points (Fig. 3.3B, 3.5D & 3.10A-B), suggesting that hyperspectral imaging may be less sensitive to extraneous variables than LDPI. Taken together, these data indicate that hyperspectral imaging provides an attractive non-invasive and absolute measure of blood oxygenation that can be used as a robust indicator of ischemic recovery over time at a cost competitive with that of an LDPI system.

Speckle variance OCT was successfully utilized to intravitally image changes over time in the femoral artery region distal to the site of arterial resection (Area 1) in order to assess formation of functional anastamoses that restore flow to the primary conduit arteries that feed the distal limb (Fig. 3.7A). Measurements at this site showed increased OCT flow signal from blood

vessels in the distal femoral artery region (Fig. 3.7A) over a time frame slightly delayed (14 vs. 7 days) relative to visualization of collateral vessels at the more proximal imaging site in the adductor muscle (Area 2) (Fig. 3.7B). Speckle variance OCT also enabled visualization of tortuous, enlarged collateral vessels in the adductor muscle region (Area 2) at 7 and 14 days post-surgery (Fig. 3.7B). The observed corkscrew vessel morphology is consistent with previous studies using post-mortem techniques to study arteriogenesis in the HLI model [21, 23, 69, 102]. Enlargement and remodeling of collateral vessels in the adductor muscle occur to compensate for increased hemodynamic demand caused by redirection of blood flow to these vessels following femoral artery ligation [67]. The ability to intravitally acquire high-resolution images to longitudinally visualize anatomical enlargement and increased hemodynamics within these collateral vessel networks is especially impactful because it provides a measure of arteriogenesis and development of stable anastamoses that bypass the arterial blockage and restore normoxia in the distal limb [13]. The use of OCT to acquire depth-resolved images that relate vessel structure and function through the skin represents a significant improvement over current methodologies used in the mouse HLI model.

The second type of OCT data was a Doppler-based endpoint and was used for transcutaneous measurement of perfusion in the femoral artery and its surrounding musculature just proximal to the popliteal bifurcation (Area 1). A vascular index calculated from this region showed slower temporal recovery from ischemia compared to more superficial measures of recovery at the paw such as hyperspectral imaging and LDPI. The Doppler OCT vascular index in the ischemic limb did not improve significantly until day 14 (Fig. 3.8D), and it did not correlate as strongly with LDPI, as compared to hyperspectral imaging (Fig. 3.9). This is likely because LDPI and hyperspectral imaging are more superficial, cutaneous measurements that

were both acquired on the paw and could be more sensitive to microvascular changes. The endpoint quantified from OCT images represents blood flow signal from deeper vasculature in a cross-sectional ROI located proximally to the paw that was defined to acquire a cross-sectional area 3 mm in length and 1-2 mm in depth centered on the distal femoral artery and vein. In this study, the Doppler OCT vascular index was measured for a single sampling volume, but future applications of OCT in the HLI model could provide an index of total blood flow by stitching together multiple volumes. Additionally, the Doppler angle could be measured from a corresponding 3-D structural image in order to study the changes in absolute blood flow that occur in the limb over time [103]. This approach would remove the angle-dependency of the vascular index used to quantify the Doppler OCT data and minimize the potential to underestimate flow as noted in the Methods. Other angle-independent parameters may also be derived from Doppler OCT data, including the pulsatility index [104] and power Doppler signal [105]. Although the imaging sites differed, the Doppler OCT vascular index correlated more strongly with LDPI than with hemoglobin saturation, likely due to the greater physiological similarity between these two measurements of perfusion. Notably, both Doppler OCT and LDPI perfusion values were reduced by about 80% in the ischemic limb in the first three days following induction of ischemia, even though data were not gathered at the same location. By day 21, the Doppler OCT vascular index of the ischemic limb exceeded that of the control limb, which is potentially the result of more smaller vessels compensating for the single, larger conduit vessel in the quantified cross-sectional area of the proximal limb. These collective data indicate that, because it is a deeper measurement that resolves flow in individual vessels (i.e. femoral artery), Doppler OCT may provide insight into the later stages of ischemic recovery that was previously inaccessible using intravital, superficial imaging techniques. This concept is

supported by previous studies suggesting that tissue recovery is heterogeneous with depth [65], and superficial measurements of resting blood flow can mask underlying flow deficits and falsely indicate full recovery of ischemic limb function that become apparent when the animal is physically challenged [106].

To our knowledge, this is the first study to measure functional and morphological data in the mouse hind limb noninvasively through the skin with OCT and quantify the response longitudinally. Speckle variance OCT provided three-dimensional images of microvessel morphology (Fig. 3.7), and Doppler OCT provided a quantitative measure of perfusion (Fig. 3.8) through the skin without contrast agents or invasive procedures. Recently, feasibility of obtaining depth-resolved microvascular images in skeletal muscle with ultrahigh sensitive optical microangiography, an extension of OCT, was demonstrated by Jia et al. [37]. In this study, tissue perfusion in the exposed gastrocnemius muscle (via incision in overlying skin) was quantified in the acute stage of ischemia (45 seconds) and qualitatively assessed over time following femoral artery ligation. Jia et al. observed pronounced reduction in blood supply within one hour of ligation followed by restoration of perfusion in the gastrocnemius at one week. Their images of blood flow in the gastrocnemius at one week agree with observations at the same time point in the current studies that tortuous collateral vessels had formed in the adductor and that flow could be detected at a distal site on the femoral artery (Fig. 3.7). However, this study did not present quantitative data to characterize the time course of recovery and required cutting the skin to expose the muscle for imaging at each time point. This uncontrolled wounding in the limb may alter the local vasculature independent of the induction of ischemia.

The combined OCT / hyperspectral imaging approach is attractive because multiple physiological parameters can be non-invasively measured through the skin at every time point

within the same animal. The inter-animal variability present in the measures of recovery even within inbred strains (Fig. 3.10) highlights the importance of longitudinally monitoring individual animals, in addition to traditional post-mortem data acquisition from separate animal cohorts at distinct time-points [50-52]. The ability to longitudinally track the response to regenerative therapies within each individual animal allows for more accurate estimations of treatment effects and better statistically-powered studies. It also enables one to study what effects discrete genetic differences in vascular morphology may have on response to specific therapeutic regimes [50, 69, 93]. In this study A/J mice were used, but these techniques are not limited to a particular mouse strain. In addition, *in vivo* imaging allows one to circumvent artifacts associated with post-mortem animal evaluation caused by injection of viscous contrast agents at super-physiologic pressures or masking of desired epitopes due to fixation [20-22].

This study validates that a combination of hyperspectral imaging and OCT allows for non-invasive *in vivo* imaging of vascular structure and function (microvessel morphology, perfusion, and blood oxygenation) over the time course of ischemic recovery. These new methods not only streamline *in vivo* evaluations, but also provide novel insights into ischemic recovery. For example, there is not an exact correlation between increases in vessel density, restoration of perfusion and oxygen delivery to the superficial tissues in anesthetized mice, and full recovery from induction of HLI (Fig. 3.9). These data suggest that biomarkers for recovery should be probed in multiple locations and tissue depths due to the heterogeneity in ischemic recovery as a function of these two parameters. Currently, most intravital assessments are superficial in nature, and the data presented herein confirm previous studies [106] suggesting that these superficial measurements in anesthetized animals can mask residual flow deficits. With current methods, a comprehensive assessment of response to HLI requires multiple modalities

and cumbersome post-mortem evaluations. Together, hyperspectral imaging and OCT provide *in vivo* images of microvessel structure and function that can be obtained in multiple locations and tissue depths for an unprecedented evaluation of vascular physiology in individual animals. This longitudinal, intravital data is complementary to standard, post-mortem micro-CT and histology endpoints that can be acquired at the end of an intravital study. Doppler OCT imaging appears to fill a unique niche relative to other intravital methods because it provides depth-resolved data and serves as an improved biomarker for the final stages of recovery from HLI. These combined techniques will facilitate the use of more complex and more physiologically relevant mouse models of PAD such as diabetic and aged animals through a reduction in both the number of cohorts required and the time required for acquisition of comprehensive data. This advance in preclinical methodologies is anticipated to accelerate the development of improved therapeutic clinical treatments for PAD.

3.6 Acknowledgments

The authors thank Anita Mahadevan-Jansen and Quyen Nguyen for the use of hyperspectral imaging equipment, Andrew Fontanella and Greg Palmer for hyperspectral algorithm assistance, and Lillian B. Nanney and Jeffrey M. Davidson for use of the LDPI.

CHAPTER 4

QUANTIFYING THE VASCULAR RESPONSE TO ISCHEMIA WITH SPECKLE VARIANCE OCT

Aim 1: Develop and validate OCT and hyperspectral imaging methods for imaging vascular morphology and function in the HLI model

Text for Chapter 4 taken from:

Poole KM, McComack DR, Patil CA, Duvall CL, Skala MC. Quantifying the vascular response to ischemia with speckle variance optical coherence tomography. Biomedical Optics Express. 2014; 5(12):4118-4130

4.1 Abstract

Longitudinal monitoring techniques for preclinical models of vascular remodeling are critical to the development of new therapies for pathological conditions such as ischemia and cancer. In models of skeletal muscle ischemia in particular, there is a lack of quantitative, non-invasive and long term assessment of vessel morphology. Here, we have applied speckle variance optical coherence tomography (OCT) methods to quantitatively assess vascular remodeling and growth in a mouse model of peripheral arterial disease. This approach was validated on two different mouse strains known to have disparate rates and abilities of recovering following induction of hind limb ischemia. These results establish the potential for speckle variance OCT as a tool for quantitative, preclinical screening of pro- and anti-angiogenic therapies.

4.2 Introduction

Vascular remodeling plays an important role in a broad range of pathological conditions including cancer [107, 108], wound healing [109], and cardiovascular disorders such as atherosclerosis, ischemia, stroke, and hypertension [107, 110, 111]. In cancer, tumor cells manipulate their microenvironment to drive remodeling and facilitate growth [112]. Wound

healing also requires angiogenesis to support transport of nutrients, inflammatory cells, and debris during the tissue repair process [109]. In cardiovascular diseases, vascular remodeling often involves insufficient vascular growth. The status of the local tissue environment, such as inflammation, hypoxia, and hemodynamics can drive these changes [107, 111]. In addition to the importance of understanding these processes at a basic science level, the ability to quantitatively evaluate the therapeutic potential of pro- and anti-angiogenic therapies in preclinical models is necessary to improve success in clinical trials [6, 107]. Characterization of vascular remodeling and screening of novel therapies are often performed in animal models of cancer [68, 107, 113], wounds [74, 114], and cardiovascular disease [6, 11, 66, 67, 111]. Vascular remodeling is a dynamic and complex process, so non-invasive tools that can quantify in vivo vascular remodeling over time are desirable.

Currently, a combination of post-mortem and in vivo methods is generally used to provide insight into vascular remodeling in a wide range of preclinical models. Information on vascular density (vessel number and lumen area) is often obtained from histological evaluation of CD31 and α-smooth muscle actin expression in excised tissue [11, 66-68]. However, this technique cannot provide longitudinal data in individual animals. Similarly, x-ray angiography [23, 66, 69] and microcomputed tomography (micro-CT) [21, 22] provide vessel morphology data, but are terminal endpoints that require contrast agents. Several in vivo imaging methods have also been employed to evaluate vascular remodeling over time, including fluorescence microscopy [28, 71], photoacoustic microscopy [72, 73], laser speckle imaging [74, 75], high frequency ultrasound [76], and magnetic resonance (MR) angiography [69, 77]. These methods provide the advantage of assessing dynamic changes in the vasculature within individual animals, but there are often trade-offs between resolution, field of view, and imaging depth. For

example, MR angiography and high frequency ultrasound provide relatively low resolution (~100 μm) images of vasculature but can penetrate deeper within tissue [76, 77], while microscopy provides higher resolution (sub-micron) images of vasculature at relatively shallow depths of approximately 0.2 mm [28]. Photoacoustic microscopy somewhat improves upon the penetration depth of fluorescence microscopy with a depth of ~0.5 mm while maintaining axial resolution on the order of 10 μm [73]. Laser speckle imaging provides vascular maps with approximately 10-25 μm resolution and covers larger spatial areas than microscopy, but data are two dimensional and superficial (< 1 mm) [74, 75]. While each of these methods has been successfully applied to assess vascular morphology in preclinical studies, there are trade-offs with each and the ideal methodology is application-specific. One widely used model of vascular remodeling and growth is the mouse hind limb ischemia (HLI) model of peripheral arterial disease (PAD), which is often used as a platform for testing novel therapies [11]. However, there is a lack of non-invasive techniques to quantitatively monitor relevant physiological endpoints longitudinally in the same animal. In the case of the mouse HLI model, methods that provide high resolution images of the vasculature (order of microns) over a depth and field of view (several millimeters) suitable for monitoring skeletal muscle are needed.

Optical coherence tomography (OCT) is well-suited to fill this niche for assessing vascular remodeling in the mouse HLI model [115]. In comparison to other imaging techniques, OCT fills a gap in resolution, field of view, and imaging depth [29, 116]. OCT collects three-dimensional data sets rapidly with resolution on the order of microns, imaging depths of ~1-3 mm, and fields of view consisting of several millimeters [29, 30, 79]. Furthermore, OCT imaging of the vasculature does not require exogenous contrast agents, since Doppler [31, 32] and speckle variance [39] OCT techniques provide spatially-resolved detection of blood flow. Vascular

imaging with OCT has been demonstrated in humans for ophthalmology applications [33, 117-121], oral microvasculature [122], and microcirculation in the skin [123, 124]. OCT has also been applied to image vasculature in numerous preclinical studies, including normal [125] or tumor [35, 36, 116] vasculature in window chamber models, cortical microvasculature [79], photodynamic therapy effects in a Barrett's esophagus model [99], retinal blood flow [126], burn wounds [114], developing vasculature in embryos [127], and ischemia effects in skeletal muscle [37, 115, 128]. Although the utility of OCT for providing high resolution images of microvasculature has been well established and significant advances have been made in image processing and quantification methods, there remains a lack of quantitative metrics for assessment of vascular morphology over extended time courses (days to weeks) that are relevant in the model of hind limb ischemia.

In this work, we have applied swept-source speckle variance OCT for quantitative, longitudinal assessment of vascular formation and remodeling over 3 weeks in the mouse HLI model of PAD. In contrast to vascular imaging studies in which the skin covering tumors is replaced with a window [35, 36, 116] or a skin incision is made to expose skeletal muscle [37], this study implements non-invasive imaging through the skin of the hind limb. As a result, confounding factors that can influence the vascular response to ischemia are minimized, and individual animals can be tracked over time, thus minimizing the effects of inter-animal variability [50]. In prior work, the use of OCT in this model was validated against standard techniques, and qualitative assessment of morphological changes with time was performed using a 20 kHz 860 nm spectral domain OCT system [115]. Here, we have extracted quantitative morphology metrics using a 100 kHz 1060 nm swept-source OCT system capable of imaging

over a wider area with improved imaging depth. We tested our metrics using the well-known phenomenon of strain-dependent variation in recovery from hind limb ischemia [23, 69, 93].

4.3 Methods

4.3.1 Animal model

Mouse strains with known robust (FVB) and poor (Balb/c) recovery to hind limb ischemia [23, 69, 93, 129] were used in this study to show that quantitative vascular imaging with OCT can resolve known differences in recovery over time. Unilateral hind limb ischemia [11] was surgically induced in male FVB and Balb/c mice (Jackson Laboratories) by ligation of the right femoral artery and vein with 6-0 silk sutures at two locations: immediately proximal to the origins of the superficial epigastric artery and deep branch of the femoral artery, and proximal to the vessels that branch toward the knee (Fig. 4.1A). Side branches between these points were also ligated, and the segment of the femoral artery and vein between the most proximal and distal ligation points was excised. The skin incision was closed with interrupted 5-0 nylon sutures. Surgery was performed under isoflurane anesthesia with animals maintained at normal body temperature. Analgesia (10 mg/kg ketoprofen) was administered subcutaneously pre-operatively and every 24 hours post-operatively until animals exhibited normal appearance and behavior. Each animal's contralateral limb served as an internal control. Mice were fed a standard chow diet ad libitum and had free access to water. All protocols were approved by the Institutional Animal Care and Use Committee of Vanderbilt University and done in accordance with the National Institutes of Health Guide for the Care and Use of Laboratory Animals.

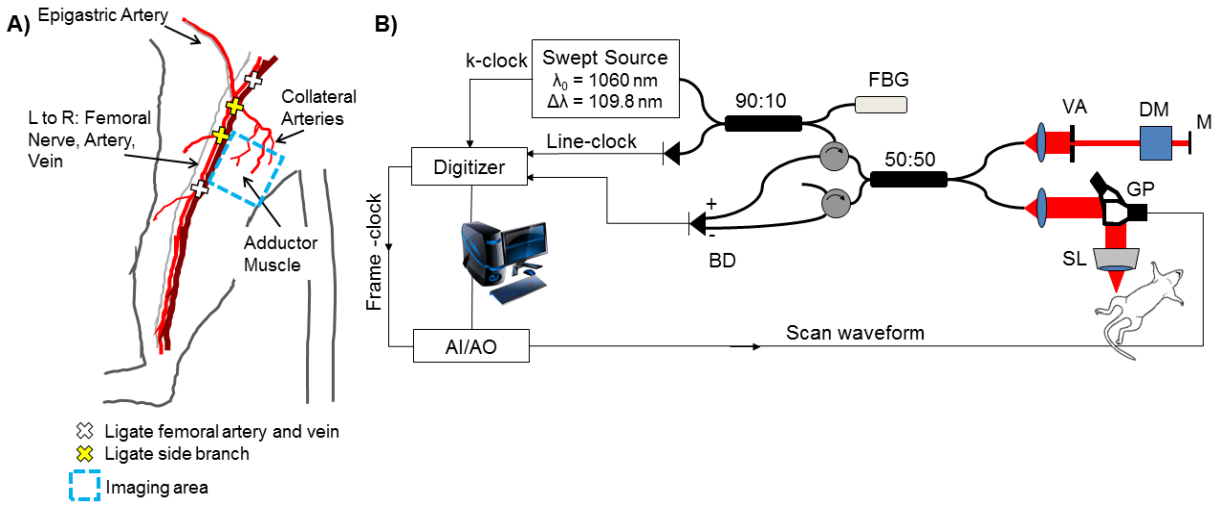

Figure 4.1: The hind limb ischemia model is depicted in (A) with vessel ligation points and the imaging area of interest in the adductor muscle region. A schematic of the swept-source OCT system with a 1060 nm center wavelength, 100 kHz sweep-rate source (Axsun) is shown in (B). Lateral and axial resolution are 16 µm and 6.5 µm in air, respectively. FBG – fiber Bragg grating. BD – balanced detector. AI/AO – Analog input/analog output. VA – variable attenuator. DM – dispersion matching cube. M – mirror. SL – scan lens. GP – galvo pair.

4.3.2 Swept-source optical coherence tomography

The swept-source OCT system (Fig. 4.1B) has a center wavelength of 1060 nm, line rate of 100 kHz (Axsun Technologies, Inc.), lateral / axial resolution of 16 µm / 6.5 µm in air, and 5.7 mW incident at the sample [128]. Speckle variance OCT volumes were collected over a 4 mm x 4 mm area in the adductor muscle region medial to the site of femoral artery excision to monitor remodeling of collateral vessels during recovery from HLI. Mice were imaged under isoflurane anesthesia (1.5%), and secured in a supine position on top of a heating pad to maintain normal body temperature. The imaged area was further stabilized with a coverslip and index matching

media. Reference marks were made on the skin of the limb with tissue marking dye to assist in alignment of the OCT system at the same region of interest for each time point. OCT volumes were 1334 A-lines per B-scan, 667 B-scans per C-scan, and 1024 pixels in the depth dimension. The resulting B-scan time was 13.34 ms, with a duty cycle of 80% and B-scan rate of 59.97 Hz. The oversampled A-lines (1334 per B-scan) were averaged over every two lines after computing the magnitude of the complex OCT data, in order to increase the signal-to-noise ratio of the magnitude data and produce higher quality speckle variance maps of the microvasculature. The resulting 6-μm sampling density (667 lines per 4 mm B-scan) exceeds the Nyquist criterion with 2.5 samples within the 16-μm lateral resolution and produces images that maximize the optical performance of the system.

Eight repeated B-scans were collected for each spatial position to allow for speckle variance image processing (Fig. 4.2), resulting in an acquisition time of 133.4 ms for each speckle variance frame and a total of 88.98 s for each volume. To visualize vascular morphology from the OCT volumes, the variance in structural images was computed over the repeated B-scans [39]. In order to best visualize the slowest flowing vessels, we selected the longest speckle observation time over which decorrelation due to bulk tissue motion did not degrade contrast in the speckle variance projections [125]. In our system, this resulted in a gate length of eight frames. The tissue was segmented in each structural (OCT magnitude) image by applying edge-detection to determine the tissue surface and an intensity threshold to exclude noise due to signal fall-off in depth. The segmented tissue mask was first applied to the speckle variance maps, which were then median filtered and de-shadowed using a step-down exponential filter [130]. Next, bulk motion artifacts were minimized by plotting the average speckle variance for each B-scan in the volume (Fig. 4.2), and identifying B-scans with high average variance which

corresponded with bulk motion artifacts. The speckle variance B-scans with motion artifacts were then replaced with the average of the nearest bulk motion-free speckle variance B-scans, and an average intensity projection over ~1.5 mm in the depth dimension (starting from the tissue surface in each axial scan) was computed to visualize all vessels within the volume in a 2D image. A Hessian filtering algorithm was then used to enhance contrast and connectivity in the depth-projected images of the vasculature [131-133]. In this step, vessels are detected using the eigenvalues of the image [132], and detection is sensitive to vessels in any orientation. Vessel detection was performed over multiple vessel scales (from ~6 to 270 μm in diameter), and the maximum filter response for each pixel was used to scale the input projection image. The resulting scaled image was thresholded to produce a binary mask of the vasculature. Quantitative vascular morphology metrics including vessel area density [134], vessel length fraction [134, 135], and vessel diameters [116] were extracted from the Hessian-filtered projection images (Table 4.1). These metrics were obtained from the projection images in the xy plane, because the de-shadowing process can potentially alter vessel morphology in the xz or yz planes [116]. Vessel area density is defined as the vessel area in the Hessian-derived mask divided by the total image area. Vessel length fraction was computed from a skeletonized image of the vessels and is defined as the total length of centerline pixels divided by the total image area. In some cases, these parameters may follow similar trends, but it is important to measure multiple endpoints to determine whether an increase in the vascular area is due to an increase in the number of vessels (total length), an increase in the size of existing vessels (diameter), or both [23]. The vessel diameter distribution indicates the relative contributions of small and large vessels to these metrics, and was extracted by determining the vessel width at each centerline pixel and computing a histogram.

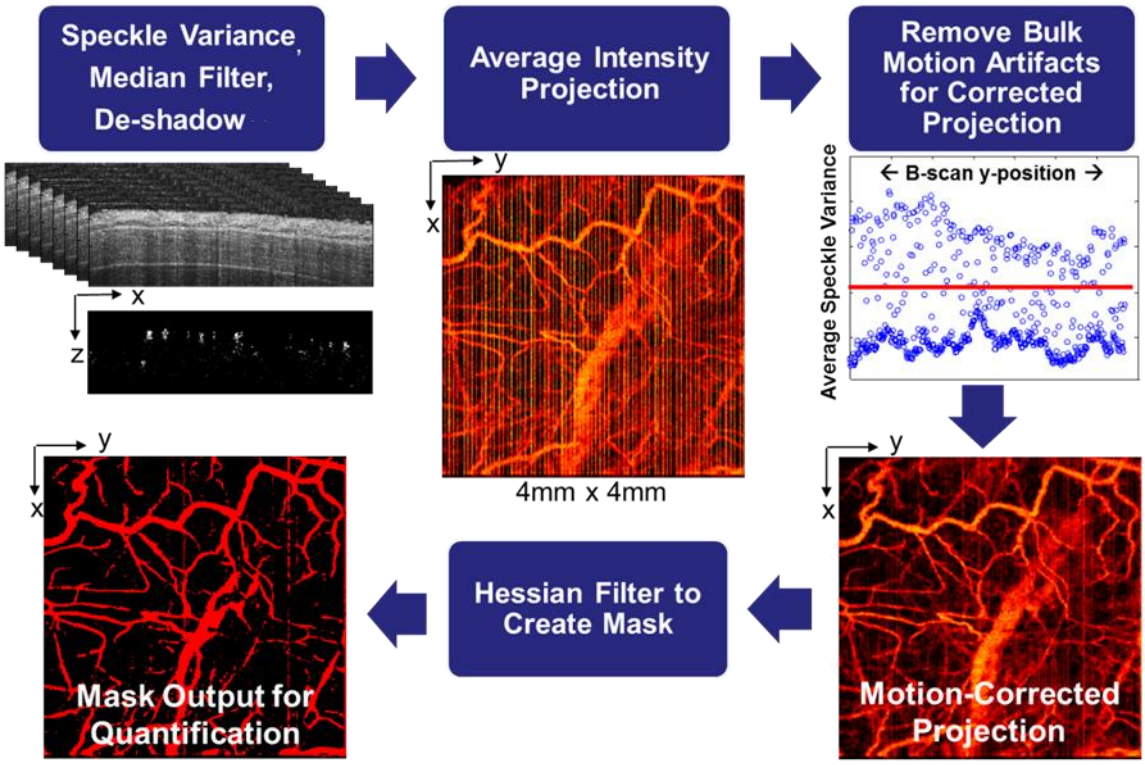

Figure 4.2: Flow chart of image processing procedures for speckle variance images of the vasculature. Speckle variance [39] was computed over eight repeated B-scans collected at each spatial position in the volume, and the tissue was segmented using the corresponding structural image. The resulting speckle variance B-scans were then median filtered, de-shadowed [130], and projected in the depth dimension. B-scans with a high average speckle variance signal due to bulk motion artifacts were identified and replaced with the average of the nearest bulk motion-free B-scans, and a corrected average intensity projection was computed. The projected image was then Hessian filtered [131-133] to derive a vessel mask from which quantitative morphology metrics were extracted.

Table 4.1. Quantitative morphology metrics extracted from speckle variance OCT projection images.

Morphology Metric	*Definition*
Vessel Area Density[134]	Vessel mask area / total image area
Vessel Length Fraction[134, 135]	Total vessel length / total image area
Vessel Diameter[116]	Diameter at each vessel centerline pixel, represented with a histogram to show distribution

4.3.3 Statistical analysis

All data are reported as mean ± standard error of the mean (SEM). A Wilcoxon Rank Sum test was performed to compare the two strains within each time point. The effect of time post-surgery on ischemic limb vessel area density and vessel length fraction within each animal was tested with a Kruskal-Wallis ANOVA followed by a post-hoc Tukey test for multiple comparisons. $P < 0.05$ was interpreted as significant.

4.4 Results

Speckle variance OCT of the ischemic limb adductor region enabled visualization of vessel remodeling over time in the Balb/c and FVB strains (Fig. 4.3). Quantification of vascular morphology metrics from average intensity projections of speckle variance volumes over ~1.5 mm in depth revealed significant differences in the vascular response to ischemia between the two strains. In the control (non-ischemic) limb, the vessel area density was significantly greater in Balb/c mice (Fig. 4.4A). At 3 days post-surgery, the vessel area density in the ischemic limb was equivalent for the two strains. At days 7, 14, and 19 (Balb/c) / 21 (FVB), the vessel area density in FVB mice was significantly greater than that in Balb/c mice ($p<0.05$). Vessel length fraction followed a similar trend, with a significant increase in this parameter for the FVB strain relative to Balb/c mice at days 7, 14, and 19/21 ($p<0.05$) (Fig. 4.4B). Furthermore, the temporal changes in these parameters were evaluated for each strain using a Kruskal-Wallis ANOVA and

post-hoc Tukey test. In Balb/c mice, vessel area density and vessel length fraction in the ischemic limb did not increase significantly over time; rather, there was a significant decrease in both parameters between day 7 and day 19 ($p<0.05$). In contrast, vessel area density increased significantly from day 3 to day 7 and vessel length fraction increased significantly between days 3 and 14 in the FVB strain.

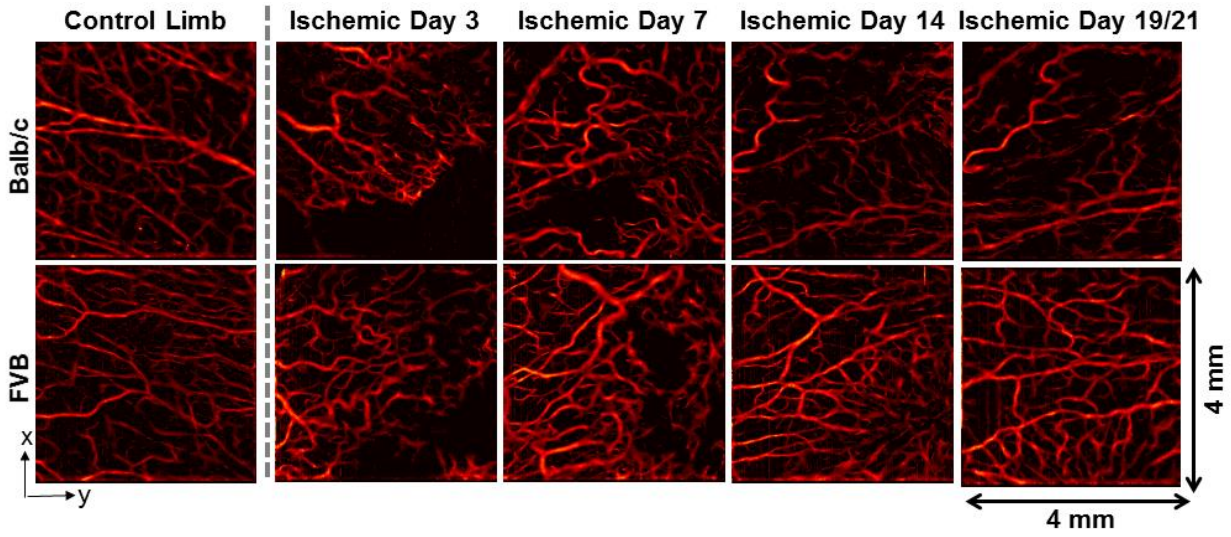

Figure 4.3: Representative speckle variance OCT images of the adductor muscle from each mouse strain, including the contralateral control limb (far left) and the ischemic limb imaged non-invasively over a time-course. Images are shown for both Balb/c (top row) and FVB (bottom row) mice. The last imaging time point was day 19 for Balb/c mice and day 21 for FVB mice.

Strain-dependent differences were also observed in distribution of vessel diameters in the ischemic limb during recovery from HLI (Fig. 4.4C). At day 3, FVB mice had a greater length of vasculature with diameters less than 24 µm, while the distribution was similar between the two strains for larger vessel diameters at this time point. At day 7 post-surgery, the length of vessels

with diameters from 36 to 124 μm was significantly greater in the FVB strain. Similar differences in the diameter distributions were observed at days 14 and 19/21 post-surgery in the 24-124 μm and 36-136 μm diameter ranges, respectively. In addition to the quantified differences in vessel morphology between the two strains in the proximal limb, differences in distal tissue fate were qualitatively observed that correlated with the OCT data. The ischemic paws of Balb/c mice had visible tissue necrosis, while the FVB strain did not suffer from this functional consequence of HLI. Lastly, structural OCT images from the adductor muscle region show changes in tissue structure beneath the skin that occur in the ischemic limb post-surgery, presumably due to inflammation (Fig. 4.5).

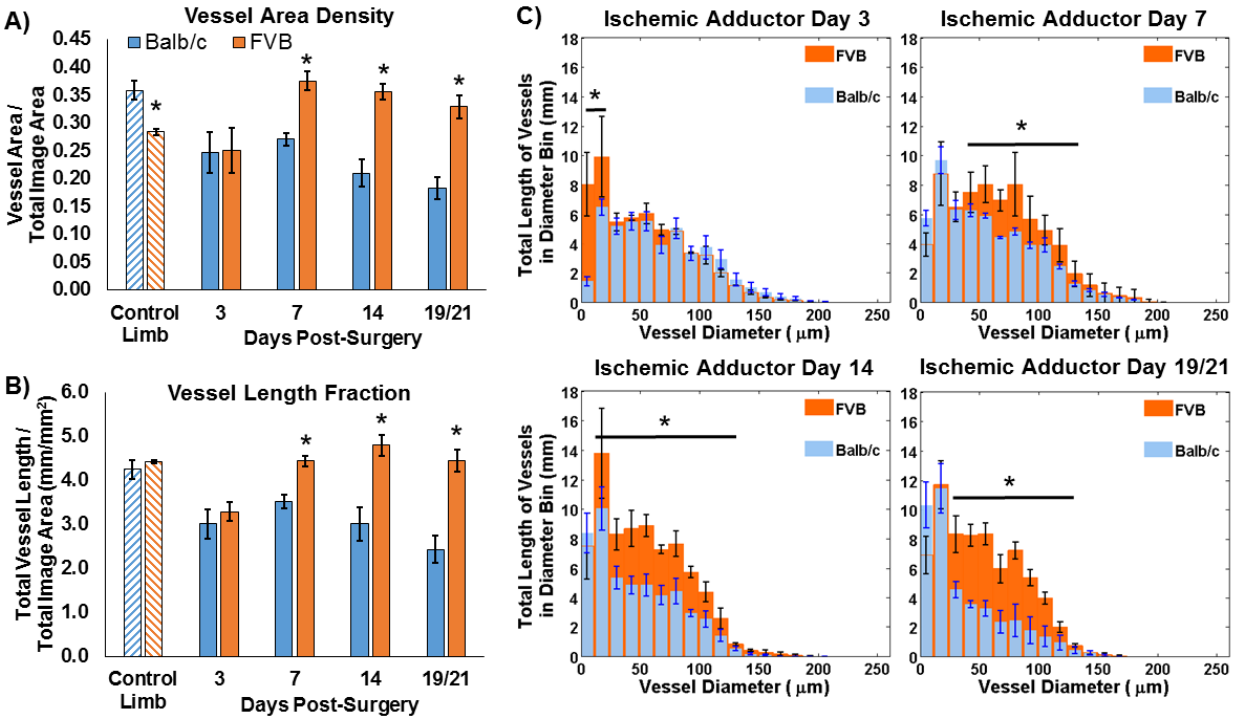

Figure 4.4: Vascular morphology metrics were quantified from speckle variance OCT projection images for Balb/c (n=4) and FVB (n=3) mice. FVB mice showed increased (A) vessel area density and (B) vessel length fraction at day 7 and subsequent time points post-surgery in the ischemic adductor region relative to Balb/c mice (*p<0.05 between strains). Balb/c mice also showed a decrease in both parameters between days 7 and 19 (p<0.05), while vessel area density and length fraction increased for FVB mice between days 3 and 7 and days 3 and 14, respectively (p<0.05). (C) Significant differences in the length of vasculature within a given range of vessel diameters were also detected (*p<0.05 for indicated range of diameters). The last imaging time point was day 19 for Balb/c mice and day 21 for FVB mice.

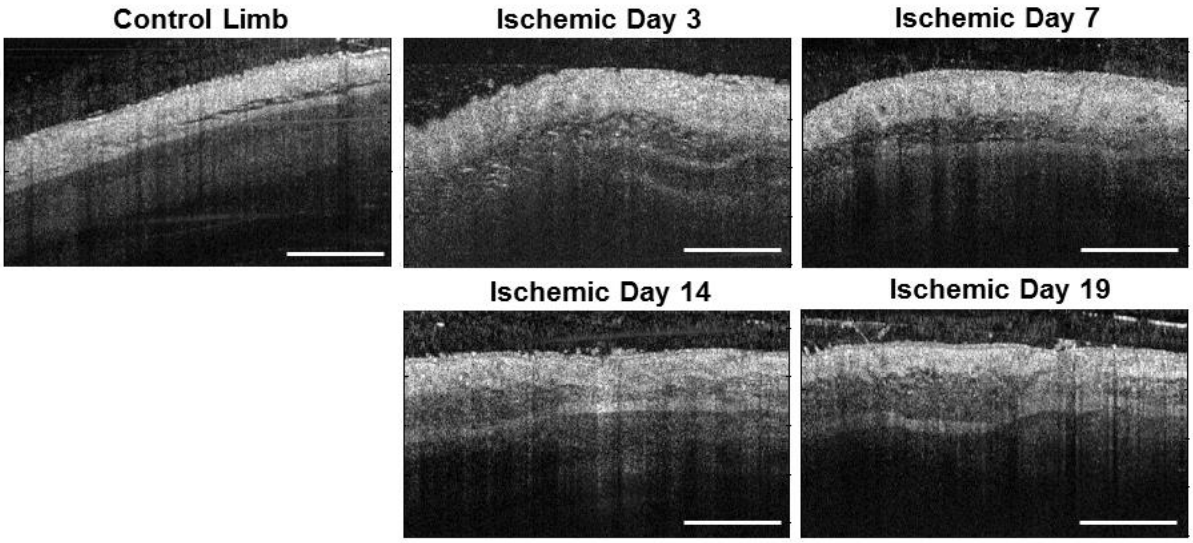

Figure 4.5: Representative structural OCT images from the adductor muscle region, including the contralateral control limb (left) and the ischemic limb imaged non-invasively over a time-course. A change in tissue structure beneath the skin is observed in the ischemic limb, presumably due to inflammation. Scale bar is 1 mm.

4.5 Discussion and Conclusions

In this work, we have demonstrated the utility of speckle variance OCT [39, 125, 130] for quantitative, non-invasive monitoring of vascular remodeling in the mouse hind limb ischemia model of PAD. OCT fills a gap in the existing toolset for evaluating this model, with micron-scale resolution, imaging depth and field of view of several millimeters, and endogenous vessel contrast [29, 116]. The speckle variance method for imaging vessel morphology has several strengths, including sensitivity to flow in microvessels, angle-independence, fast acquisition, and little increase in computational complexity [130]. The application of speckle variance OCT for quantitative imaging of the vascular response to HLI has potential to provide new insight into the

dynamics of vascular remodeling, as well as streamline the evaluation of novel therapies in preclinical trials.

To validate the OCT system, image preprocessing routines, and techniques for data analysis that are collectively necessary for investigation of vascular remodeling in the HLI model, it was necessary to first identify a reliable experimental model. The ability to differentiate the responses of two groups was validated through the comparison between a mouse strain with a robust response to ischemia (FVB) and a strain known to have poor recovery (Balb/c) [23, 69, 93, 129]. Variations in native collateral conductance and collateral remodeling have been observed among commonly used inbred strains, with Balb/c mice in particular exhibiting less collateral remodeling accompanied by severe ischemic tissue injury compared to other strains (e.g. A/J, C57BL/6) [93]. Additionally, tissue loss due to severe ischemia may reduce the speed and extent of collateral artery growth, since fluid shear stress and total flow are reduced [23]. In the current study, *in vivo* longitudinal quantification of vascular morphology in FVB mice reflected a greater vessel area density, length fraction, and diameter compared to Balb/c mice (Fig. 4.3-4.4). Balb/c mice demonstrated impaired recovery based on these metrics and also suffered from ischemic paw necrosis. Our results are similar to those in previous studies showing a lack of change in vessel density in the adductor of Balb/c mice using post-mortem histology [23], and a decreasing trend for Balb/c adductor perfusion at later time points using laser Doppler perfusion imaging [93]. Differences in trends between studies can be attributed to the severity of the surgical model, which ranges from a single ligation of the femoral artery [23] to multiple ligations and transection of a vessel segment as performed in the current work [21]. In contrast, FVB mice respond similarly to the A/J strain, with small native collaterals that undergo greater

remodeling after femoral artery ligation (determined from laser Doppler perfusion imaging and post-mortem X-ray angiography and histology) [93].

The quantitative metrics for vessel density, length, and diameter quantified for this model are comparable and complementary to endpoints of vascular morphology collected with traditional post-mortem methods. At the terminal endpoint of a longitudinal vascular remodeling study, morphological parameters such as number of collateral vessels, vessel volume, vessel thickness and connectivity may be obtained from x-ray angiography [23, 66, 69] or micro-CT [21, 22], and high resolution capillary or arteriole density can be measured with histology by staining for CD31 or smooth muscle actin, respectively [11, 66-68]. Angiography and micro-CT provide a global view of the hind limb vasculature, while speckle variance OCT fills a gap in field of view between these global measurements and the two dimensional slices that are sampled with histology. Additionally, speckle variance OCT detects perfused vessels with contrast based on blood flow, while staining fixed tissues for histological examination will label all endothelial and/or smooth muscle cells regardless of whether the vessels were perfused *in vivo*. These data sets are complementary because they provide assessments of both functional vessel density (with OCT) and total vessel density (i.e. counting capillaries stained with CD31). In addition to providing important intravital measurements of vascular remodeling that are not captured with post-mortem analyses, non-invasive speckle variance OCT enables us to track these metrics in individual animals over time. Longitudinal assessment of individuals is particularly important for minimizing inter-animal variability, because even inbred strains of mice can have variability in pre-existing vasculature that impacts ischemic recovery [50]. Furthermore, in preclinical assessment of novel therapies, long term studies should be performed in order to capture the late-stage regression phase of the response that occurs in more relevant

models of PAD such as diabetic mice, which is often omitted in studies where researchers must choose a few, terminal endpoints to analyze [136].

Although long term visualization of vasculature is valuable in itself as a qualitative endpoint, quantitative assessment of vascular remodeling enables a more robust evaluation of disease status or therapeutic efficacy [137]. Previous studies have applied quantitative analysis of OCT angiography data in several preclinical models, although to our knowledge, long term, non-invasive (through the skin) quantitative vascular metrics have not been previously demonstrated in ischemic skeletal muscle. Commonly used metrics for vascular morphology studies performed with OCT include vessel area density and vessel length fraction, which represent the area filled by vessels and the total length of vessels, respectively [134, 135, 137]. Vessel diameters have also been extracted [116], and the distribution provides insight into the contributions of vessels of various sizes to global measurements of length and density. Other parameters of interest include tortuosity and fractal dimension, which provide a measurement of vessel branching and architecture [116, 134, 137, 138]. Although longitudinal changes in blood flow have been quantified in the HLI model using Doppler OCT [115] and optical microangiography techniques [37], assessment of vessel morphology has been limited to qualitative observations [37, 115]. In this work, we applied quantitative morphology metrics that have been used in preclinical studies of tumors [116, 137], burn wounds [114], and healthy tissue [134] to non-invasively monitor the response to ischemia in skeletal muscle vasculature, and demonstrated their sensitivity for discriminating groups with different responses.

In comparison with OCT systems used in previous studies [115], the speed and penetration depth of the 100 kHz, 1060 nm swept-source system used here is well suited to imaging in the HLI model. While previous studies have utilized an 860 nm spectral domain

system, the 1060 nm swept-source used here increases the theoretical depth limit for capturing flow in skeletal muscle vessels due to reduced scattering at longer wavelengths, and also reduces roll-off in imaging sensitivity with depth due to the improved spectral resolution at which the interference signal is sampled [139]. Previous studies have noted that arterioles lie in a deeper layer of the muscle (beginning >700 μm from surface) [37], and these vessels are critical to delivering oxygenated blood to peripheral tissues. For this reason, imaging deeper with OCT allows for a more thorough assessment of blood supply in the hind limb ischemia model that is not available using techniques with relatively shallow penetration such as microscopy. Additionally, swept-source lasers near 1300 nm will further improve imaging depths in the HLI model. Ideally, imaging should be performed over an area large enough to cover a region of interest such as the adductor, gastrocnemius, or distal femoral artery to comprehensively cover areas where vascular remodeling occurs. In previous studies [115], limitations to the OCT instrument necessitated acquisition of multiple C-scans to achieve this goal, and minimizing motion artifacts during long acquisition times was a significant challenge. The fast 100 kHz A-scan rate improves upon the 20 kHz imaging speed of the previous system used to image HLI, and thus volumes can be collected with reduced motion artifacts. Furthermore, larger areas can be scanned without increasing the acquisition time compared to the previous work.

Although the imaging speed was a significant improvement in this study, *in vivo* OCT is still susceptible to bulk motion artifacts due to respiration and heartbeat. Streaks due to motion artifacts (Fig. 4.2) may affect subsequent vessel segmentation procedures and quantification of morphology [140], so minimizing artifact signal while preserving vessel contrast in the image is desired. In this work, we developed an approach to minimizing these artifacts in the resulting vascular maps which consisted of identifying frames with bulk motion using an average B-scan

variance threshold. After the motion artifact frames were replaced with the average of the nearest motion-free frames, the depth projections were largely free of high intensity bands corresponding to motion. Other post-processing techniques for reducing motion artifacts include frequency rejection filters [141] and segmentation of vessels in B-scans with a classifier algorithm [140]. The former is effective for periodic motion artifacts but may be less so for removal of bulk motion that is non-periodic [140, 141]. The latter can be applied to both periodic and non-periodic bulk motion, but the classifier algorithm requires a training set of manually segmented images [140]. There are also several methods available for addressing the challenge of motion artifacts in speckle variance OCT during acquisition, including the use of orthogonal scan patterns [117, 142], short acquisition times [138], optimizing frame rates (field of view) and gate length [125]. However, additional scans increase acquisition time and data storage/processing, and acquiring faster scans may compromise field of view and sensitivity to slow flow. We must cover a relatively large region of interest in the HLI model, so we developed a robust post-processing approach to minimize motion artifacts.

Similarly, several methods have been established for vessel segmentation and filtering in OCT angiography data sets. Approaches range from intensity thresholding and band pass filtering [138] to clutter rejection [143] and directional filters (Gabor) [117]. Here, we chose to implement a Hessian filter [131-133] due to speed of computation and the multi-scale estimation of vessel-like structures that is compatible with segmenting the range of vessel sizes observed in the HLI model. The Hessian filter extracts the principle directions of the image, detects vessels at any orientation, and is computed at multiple vessel scales [131]. In comparison, the Gabor filter requires a convolution at evenly spaced rotations to determine the orientation of maximum response, and the response must be computed at multiple scales [117]. This results in a greater

computational burden compared to the Hessian filter approach. Compared to intensity-based methods, Hessian filters are less sensitive to noise and intensity variations, and are more selective in identifying vessel shape as the eigenvalues of the Hessian are used to locally detect vessels [131, 132]. Hessian filtering does not require prior manual removal of noise, and the resulting vessels are smoother in comparison to vessels segmented based on an intensity threshold [132]. Furthermore, the quantification of closeness (or likelihood) to a vessel structure for each pixel enables additional control in excluding noise from the segmented vessel mask.

In conclusion, understanding the mechanisms and dynamics of vascular remodeling processes is critical to the development of new pro- and anti-angiogenic therapies for treating pathological conditions from ischemia to cancer. Although models such as mouse HLI are widely used to assess the therapeutic potential of new treatments for PAD and other ischemia-related diseases, quantitative, high resolution methods for intravital, longitudinal measurements are lacking. To address this need, we developed speckle variance OCT methods for assessment of remodeling in the ischemic limb and demonstrated the sensitivity of our approach to detect strain-dependent recovery from ischemic injury. In this context, the quantitative morphology metrics (vessel area density, length fraction, and diameter) obtained from speckle variance OCT data were sensitive to differences in the vascular response to ischemia. Overall, this work confirms that quantitative speckle variance OCT is a promising technique for robust preclinical evaluation of novel therapies, an essential step for successful translation to early clinical trials.

4.6 Acknowledgments

The authors thank Megan Madonna and Constance Lents for assistance with experiments, and Andrew Fontanella for assistance with vascular image processing.

CHAPTER 5

ROS-RESPONSIVE MICROSPHERES FOR ON DEMAND ANTIOXIDANT THERAPY IN A MODEL OF DIABETIC PERIPHERAL ARTERIAL DISEASE

Aim 3: Apply optical imaging and conventional methods to develop new and more effective therapeutic interventions for improving HLI recovery

Text for Chapter 5 taken from:

Poole KM, Nelson CE, Joshi RV, Martin JR, Gupta MK, Haws SC, Kavanaugh TE, Skala MC, Duvall CL. ROS-responsive microspheres for on demand antioxidant therapy in a model of diabetic peripheral arterial disease. Biomaterials. 2015; 41(0):166-175.
DOI link: http://dx.doi.org/10.1016/j.biomaterials.2014.11.016

5.1 Abstract

A new microparticle-based delivery system was synthesized from reactive oxygen species (ROS)-responsive poly(propylene sulfide) (PPS) and tested for "on demand" antioxidant therapy. PPS is hydrophobic but undergoes a phase change to become hydrophilic upon oxidation and thus provides a useful platform for ROS-demanded drug release. This platform was tested for delivery of the promising anti-inflammatory and antioxidant therapeutic molecule curcumin, which is currently limited in use in its free form due to poor pharmacokinetic properties. PPS microspheres efficiently encapsulated curcumin through oil-in-water emulsion and provided sustained, on demand release that was modulated *in vitro* by hydrogen peroxide concentration. The cytocompatible, curcumin-loaded microspheres preferentially targeted and scavenged intracellular ROS in activated macrophages, reduced *in vitro* cell death in the presence of cytotoxic levels of ROS, and decreased tissue-level ROS *in vivo* in the diabetic mouse hind limb ischemia model of peripheral arterial disease. Interestingly, due to the ROS scavenging behavior of PPS, the blank microparticles also showed inherent therapeutic properties that were synergistic with the effects of curcumin in these assays. Functionally, local delivery of curcumin-PPS microspheres accelerated recovery from hind limb

ischemia in diabetic mice, as demonstrated using non-invasive imaging techniques. This work demonstrates the potential for PPS microspheres as a generalizable vehicle for ROS-demanded drug release and establishes the utility of this platform for improving local curcumin bioavailability for treatment of chronic inflammatory diseases.

5.2 Introduction

Elevated levels of reactive oxygen species (ROS) cause oxidative stress that contributes to inflammation-related pathologies such as peripheral arterial disease (PAD) [144-146]. Under pathological conditions, leukocytes that are recruited to inflamed sites produce and then release an excess of ROS, causing harm to the surrounding tissues through DNA damage and lipid peroxidation [82, 144, 146]. This process is self-propagating, as the ROS released by inflammatory cells can increase the expression of leukocyte adhesive factors on the endothelium, resulting in local extravasation of additional leukocytes that produce additional ROS [147, 148]. Diabetic patients are especially susceptible to oxidative stress and inflammatory diseases, because excessive glucose increases expression of endothelial cell nitric oxide synthase (eNOS) and the production of superoxide, leading to increased generation of hydroxyl radicals, hydrogen peroxide, and peroxynitrite [41, 55, 56]. In diabetes, there is a chronic pro-inflammatory environment, where ROS contributes to both endothelial dysfunction and a predisposition to PAD [41, 42]. The strong relationship between hyperglycemia, oxidative stress, and microvascular complications is also supported by observations that compared to the general population, diabetic patients have a four times greater risk of developing PAD [5], worse lower-extremity function [14], and a greater risk of amputation [2, 15]. Furthermore, preclinical studies have shown that animals with type 1 diabetes have an impaired vascular response to ischemia [43-45] and that decreasing oxidative stress improves post-ischemic neovascularization [43, 44].

Therefore, therapeutics that locally reduce oxidative stress have significant potential for treatment of inflammatory diseases such as diabetic PAD.

Curcumin, a natural molecule derived from turmeric, is an anti-inflammatory and antioxidant agent that acts through inhibiting the pro-inflammatory transcription factor nuclear factor kappa B (NF-κB) [149, 150] and by scavenging oxidative free radicals through H-atom donation and/or electron transfer [151]. These therapeutic effects would be beneficial for treatment of PAD in the context of chronic, diabetes-induced oxidative stress, and curcumin has shown promise in preclinical ischemia/reperfusion studies [152, 153]. However, therapeutic use of curcumin is limited due to its extreme hydrophobicity which reduces absorption and leads to rapid metabolism and elimination [154]. One approach to overcoming the poor aqueous solubility and stability of curcumin for clinical applications is to deliver it locally from a depot [80]. In order to improve bioavailability of curcumin, sustained/targeted delivery approaches including hydrogels [80], exosomes [81], and stimuli-responsive nanoparticles [82] have been pursued. Microparticles comprising hydrophobic, biodegradable polymers also offer a useful approach for creating an injectable, local depot for controlled drug release [83]. However, conventionally used PLGA-based microparticles are degraded by non-specific hydrolysis and produce acidic degradation products that can exacerbate local inflammation [84] and activate autocatalytic degradation of the particles [85]. This autocatalytic degradation leads to an uncontrolled drug release profile that limits the effectiveness of these particles as vehicles for sustained drug release.

Here, poly(propylene sulfide) (PPS) has, for the first time, been fabricated into microparticles and explored as a candidate for encapsulation and “on demand” delivery of curcumin at sites of oxidative stress. The hydrophobicity of PPS makes it a good candidate for

efficient encapsulation of curcumin via oil-in-water (O/W) emulsion methods [83, 155]. Hydrophobic PPS undergoes a morphological transition to more hydrophilic poly(propylene sulfoxide) and poly(propylene sulfone) upon exposure to ROS. Oxidation-responsive polymersomes [86], nanoparticles [87, 88], micelles [89, 90], and hydrogels [49] have been applied; however, there is no example of formulated micron-scale particles that are more effectively retained at the tissue site and generate a stable, local depot for sustained, oxidation-responsive, on demand delivery. This system was designed to leverage the oxidative conversion of PPS to more hydrophilic forms as a trigger for on demand release of the anti-inflammatory/antioxidant molecule curcumin. The ability to modulate therapeutic release based upon environmental demand [46-49] is anticipated to yield more efficient and sustained local delivery, particularly when applied in the context of diabetic PAD. The studies presented herein include microparticle fabrication and characterization, assessment of on demand release kinetics, and testing for therapeutic effects *in vitro* and *in vivo*. The *in vivo* studies were carried out in the diabetic mouse hind limb ischemia model and showcase new, non-invasive imaging techniques for measuring ischemic limb recovery [115].

5.3 Materials and Methods

5.3.1 Materials

All chemicals were purchased from Sigma–Aldrich (St. Louis, MO, USA) and used as received unless otherwise described. Curcumin (368.38g/mol; ≥94% curcuminoid content) was obtained from Sigma. Propylene sulfide was purchased from Acros Organics (NJ, USA) and purified by distillation just before polymerization. 87-90% hydrolyzed poly(vinyl alcohol) (PVA) of average molecular weight 30,000-70,000 was prepared into a 1% w/v solution in deionized water. Transwell inserts with 0.4 μm pore polycarbonate membranes (Corning,

Lowell, MA, USA) were used in 24 well plates for curcumin release experiments. SIN-1 was purchased from Invitrogen (San Diego, CA, USA) as a package of 1 mg vials. Cell culture reagents, including fetal bovine serum (FBS), Dulbecco's Modified Eagle Medium (DMEM), and penicillin-streptomycin (p-s) were supplied by Gibco Cell Culture (Carlsbad, CA, USA). 4-Cyano-4-(ethylsulfanyltiocarbonyl) sulfanylpentanoic acid (ECT) was synthesized following the previously reported procedure [156].

5.3.2 Microsphere synthesis and characterization

5.3.2.1 Synthesis of poly(propylene sulfide) (PPS)

To prepare PPS as previously described [90, 157], propylene sulfide (3.16 mL, 40.4 mmol), ECT (52 mg, 0.20 mmol), TPPCl (tetraphenylphosphonium chloride – $Ph_4P^+Cl^-$) (14.9 mg, 0.040 mmol), and dry NMP (N-methyl pyrolidone) (10 mL) were placed in a dry glass ampoule equipped with a magnetic stirring bar, and the solution was degassed by three freeze-evacuate-thaw cycles. The reaction mixture was stirred at 60°C for 20 hours, and the resulting polymer (Fig. A.1) was purified by precipitation twice into a large excess of methanol and dried at 60°C under vacuum to yield a red/yellow polymer oil. ^{1}H-NMR ($CDCl_3$, 400 MHz): = 1.25-1.45 (s, C**H**$_3$), 2.5-2.7 (m, C**H**), 2.85-3.0 (m, -C**H**$_2$).

5.3.2.2 Characterization of PPS

PPS was characterized for molecular weight and polydispersity by gel permeation chromatography (GPC, Agilent Technologies, Santa Clara, CA, USA), and the chemical structure of the polymer was also analyzed by ^{1}H NMR spectra recorded in $CDCl_3$ (Brüker 400 MHz spectrometer). Molecular weight was measured using GPC with DMF + 0.1 M LiBr mobile phase at 60°C through three serial Tosoh Biosciences TSKGel Alpha columns (Tokyo, Japan). An Agilent refractive index (RI) detector and a Wyatt miniDAWN Treos multi-angle light

scattering detector (Wyatt Technology Corp., Santa Barbara, CA, USA) were used to calculate absolute molecular weight based on dn/dc values experimentally determined using offline injections into the RI detector.

5.3.2.3 Microsphere fabrication and drug loading

Curcumin encapsulated PPS microspheres were prepared using a modification of the oil-in-water (O/W) emulsion solvent evaporation method [83, 155]. Briefly, curcumin (20 mg) and PPS (20 mg) were dissolved in a 10:1 mixture of chloroform (1.5 mL) and methanol (0.15 mL) and ultrasonicated (Cole-Parmer, USA) until both polymer and curcumin were completely dissolved to form the oil (O) phase. The 10% methanol was necessary to achieve curcumin solubility. The O phase was then emulsified in 1% (w/v) aqueous PVA solution (6 mL) using an Ultra-Turrax TP 18-10 homogenizer (Janke and Kunkel KG, IKA-WERK) at 20,000 rpm for 1 minute. For solvent removal, the emulsion was then subjected to high vacuum (~635 mm Hg) using a rotary evaporator (Rotavapor RII, BUCHI, Switzerland). Microspheres were then recovered by centrifuging (Allegra X-12 Centrifuge, Beckman Coulter, USA) the remaining aqueous solution at 16,500xg for 5 minutes. The microspheres were then washed once with deionized water and lyophilized (Labconco Freezone 4.5, USA). Unloaded control PPS microspheres were made using the same method described above but without addition of curcumin.

5.3.2.4 Microsphere characterization

Curcumin encapsulated microspheres were characterized for size and morphology by scanning electron microscopy (SEM, Hitachi S-4200, Hitachi Ltd, Tokyo, Japan). The microspheres were suspended in a water drop and placed on a double sided carbon tape attached to an aluminum stub, air dried, and then sputter coated with gold for 30 seconds. Curcumin

encapsulation was confirmed by fluorescent microscopy using a Nikon Eclipse Ti inverted fluorescence microscope (Nikon Instruments Inc., Melville, NY). To do so, microspheres were suspended into a water drop on a glass slide and imaged after covering with a glass cover slip. Drug loading in the microspheres was determined by fully dissolving microspheres in DMSO (1 mg/mL) overnight, centrifuging at 16,500xg for 3 min, and quantifying the curcumin concentration in the supernatant using fluorescence of curcumin (excitation 488 nm, emission 535 nm) in a plate reader (Tecan Group Ltd., Mannedorf, Switzerland). Drug loading and encapsulation efficiency were calculated from the extracted curcumin using established methods [158]. Size of the microspheres was quantified using ImageJ 1.45s software (Freeware, NIH, Bethseda, MD) by measuring SEM diameters of >100 microspheres.

5.3.3 ROS-dependent curcumin release kinetics *in vitro*

In vitro release profiles of curcumin from PPS microspheres were obtained by exposing the PPS microspheres to 0, 0.5, 5, 50, 500, and 882 (3 wt%) mM concentrations of H_2O_2 for 56 days and quantifying the amount of released curcumin by fluorescence (excitation 488 nm, emission 535 nm). PBS (1X, pH 7.4) containing 0.1% w/v N-acetylcysteine (NAC) and 0.01% w/v butylated hydroxytoluene (BHT) was used as the release buffer. Microspheres containing 5 µg curcumin were suspended in 1 mL release buffers with H_2O_2 and placed in the top of transwell inserts (pore size of 400 nm) in 24-well plates. The wells were sealed with parafilm and incubated at 37°C under constant shaking (30 rpm). Releasate was collected from the bottom chamber at regular time intervals and the release buffer was removed and replaced with fresh buffer. Removed release buffer was diluted 2X with 100% ethanol for complete dissolution and evaluated by fluorescence on a plate reader (Tecan Group Ltd., Mannedorf, Switzerland) at excitation 488 nm, emission 535 nm based on a curcumin fluorescence standard curve prepared

in the same buffer. Control experiments were performed after 14 hours of incubation to ensure no effect of H_2O_2 on quantification of free curcumin (data not shown). All release experiments were performed in triplicate. Release experiments were repeated with 3-morpholinosydnonimine (SIN-1) which generates nitric oxide, superoxide, and peroxynitrite [159, 160]. Release buffers containing 0.1 mM, 1 mM, and 2 mM SIN-1 were prepared. In order to measure on demand delivery of encapsulated curcumin, microspheres placed in the top of transwell inserts were subjected to intermittent SIN-1 for 4 day intervals for a maximum of 72 days. Microspheres were subjected to control buffer for 4 days for the "off" phase, and the respective SIN-1 concentration was added at the beginning of each "on" phase of the experiment. Buffer containing SIN-1 was replaced with control buffer at each subsequent "off" interval.

5.3.4 *In vitro* curcumin delivery

5.3.4.1 Curcumin-mediated cell survival

NIH-3T3 fibroblasts were transduced with lentivirus to express luciferase (LR-3T3s) as described previously [161]. LR-3T3s were cultured in DMEM supplemented with 10% FBS and 1% p-s, then seeded at 5000 cells/well in a black-walled 96-well plate and incubated at 37°C overnight. The media was replaced with fresh media containing no microspheres, blank PPS microspheres, or PPS microspheres containing curcumin. Varying concentrations of H_2O_2 were added ranging from 0-1 mM. The cells were then incubated at 37°C for 24 hours. Fresh media containing D-luciferin (Biosynth, Itasca, IL) was added to each well at a final concentration of 5 µg/mL, and the luminescence from the viable cells was measured using an IVIS 200 (Xenogen). Luminescence images were analyzed with Living Image® software Version 3.2 (Perkin Elmer).

5.3.4.2 Cellular internalization of microspheres

3T3 fibroblasts and RAW 264.7 macrophages were seeded in 6-well plates (230,000 cells/well for flow cytometry) or an 8-well chamber cover slip (12,000 cells/well for microscopy) in DMEM supplemented with 10% FBS and 1% p-s and allowed to adhere overnight. Cells were then treated with fresh DMEM with curcumin-loaded PPS microspheres at a curcumin dose of 3.4 μM. One cohort of RAW macrophages were activated to a pro-inflammatory M1 phenotype with 100 ng/mL of LPS and 100 U/mL of interferon-gamma (IFN-γ) [162, 163] to assess the effect of macrophage phenotype on microparticle uptake. All groups were incubated with treatments for 24 hours, then cells were washed 3 times with PBS. For confocal microscopy, cells were imaged in phenol-red free DMEM media with 0.05% trypan blue in order to determine intracellular uptake of microspheres by different cell types. For flow cytometry (FACSCalibur, BD Biosciences), cells were harvested in 0.05% trypan blue in PBS prior to measurement of intracellular curcumin fluorescence.

5.3.4.3 Macrophage intracellular ROS production in vitro

RAW 264.7 cells were seeded at 230,000 cells/well in 6-well plates in DMEM supplemented with 10% FBS and 1% p-s and were allowed to adhere overnight. Cells were then treated for 1 hour with either blank PPS microspheres or curcumin-loaded PPS microspheres in fresh DMEM medium at a curcumin concentration of 3.4 μM, and then 100 ng/mL of LPS and 100 U/mL of IFN-γ was added to the media prior to an additional 24 hours of incubation to stimulate production of ROS. Control groups consisted of cells without LPS/IFN-γ stimulation and stimulated cells with no microparticle treatment. After 24 hours of stimulation, cells were washed with PBS and then incubated with 5 μM H2-DCFDA in phenol red-free, serum-free DMEM for 25 minutes. Cells were washed with PBS and harvested in 0.05% trypan blue in PBS.

ROS-induced, intracellular fluorescence was measured via flow cytometry (FACSCalibur, BD Biosciences) and analyzed using FlowJo software. Curcumin fluorescence was compensated for using cells receiving the same treatments but without addition of the DCFDA dye.

5.3.4.4 ELISA to measure effects of curcumin microspheres on MCP-1

RAW 264.7 macrophages were seeded at 20,000 cells/well in a 96-well plate in DMEM supplemented with 10% FBS and 1% p-s and were allowed to adhere overnight. Cells were then treated for 1 hour with either blank PPS microspheres or curcumin-loaded PPS microspheres in fresh DMEM medium (phenol red-free, 1% FBS, 1% p-s) at a curcumin concentration of 3.4 μM, and then the media was supplemented with 100 ng/mL of LPS and 100 U/mL of IFN-γ for an additional 2 hours to stimulate production of ROS. Unstimulated cells were used as a control. After incubation with microspheres and LPS/IFN-γ, the treatments were removed and the cells were given fresh, phenol-red free DMEM (1% FBS, 1% p-s). After 24 hours of incubation, culture media was harvested for measurement of monocyte chemoattractant protein-1 (MCP-1) concentration using an ELISA kit (PeproTech). Protein concentration was normalized to relative cell number using a lactate dehydrogenase (LDH) assay (Promega) performed on lysed cells (KDalert lysis buffer, Life Technologies).

5.3.5 *In vivo*

5.3.5.1 Mouse hind limb ischemia model

Type 1 diabetes was induced in 8-week-old male FVB mice (Jackson Laboratories) with daily intraperitoneal injections of streptozotocin (50 mg/kg) for 5 consecutive days after a 5 hour fast [164]. Glucose levels were measured immediately before induction of hind limb ischemia, and mice with levels above 300 mg/dl were considered diabetic. After 4 weeks of hyperglycemia, hind limb ischemia [11] was surgically induced as described previously [128].

Briefly, the femoral artery and vein of the right hind limb were ligated with 6-0 silk sutures at two locations: immediately proximal to the origins of the superficial epigastric artery and deep branch of the femoral artery, and proximal to the vessels that branch toward the knee. Major side branches were also ligated, and the ligated segment of the femoral artery and vein was excised. The skin incision was closed with interrupted 5-0 nylon sutures. Surgery was performed under isoflurane anesthesia at normal body temperature. Analgesia (10 mg/kg ketoprofen) was administered subcutaneously pre-operatively and every 18-24 hours post-operatively until animals exhibited normal appearance and behavior. At 4 hours post-surgery, the ischemic hind limb was treated with saline, blank PPS microspheres, or curcumin-loaded PPS microspheres at 5 mg/kg curcumin and 10.3 mg/kg PPS via intramuscular injection into the gastrocnemius and adductor muscles (5 x 20 µL injections). Mice were fed a standard chow diet ad libitum and had free access to water. All protocols were approved by the Institutional Animal Care and Use Committee of Vanderbilt University and done in accordance with the National Institute of Health's *Guide for the Care and Use of Laboratory Animals*.

5.3.5.2 In vivo local retention of curcumin delivered from PPS microspheres

In a separate cohort of mice, hind limb ischemia was induced, and at 4 hours post-surgery, curcumin-loaded microspheres were injected into both the ischemic and control limbs (5 mg/kg curcumin in 10.3 mg/kg PPS) via intramuscular injection. The kinetics of local release of curcumin from PPS microspheres was imaged non-invasively using a Xenogen IVIS 200 to measure curcumin fluorescence (ex: 445-490 nm, em: 515-575 nm).

5.3.5.3 ROS measurement in extracted gastrocnemius

After 7 days of ischemia, the gastrocnemii of mice from the different treatment groups were extracted immediately postmortem and transferred into PBS in a 24-well plate. A

background image of both sides of the gastrocnemius was collected with a Xenogen IVIS 200 (ex: 670 nm, em: 700 nm). The gastrocnemius was then incubated with an ROS-sensitive, fluorescent hydrocyanine dye at a concentration of 100 µM (ROSstar 650, Li-Cor Biosciences, Lincoln, NE) [165] for 45 minutes in the dark then washed with PBS. Both sides of the gastrocnemius were then imaged again with an IVIS 200 (ex: 670 nm, em: 700 nm). ROS was also measured with the hydrocyanine dye method in one untreated animal at day 1 to confirm increased ROS levels in the gastrocnemius at an early time point. The average radiance from the ROS-sensitive fluorescence was quantified for all gastrocnemii images using Living Image® software Version 3.2 (Perkin Elmer).

5.3.5.4 Intravital hyperspectral imaging of hemoglobin oxygen saturation

Hyperspectral imaging of the footpads was performed at days 0, 2, 4, and 6 post-surgery as described previously [115, 128]. Briefly, a halogen lamp coupled into a liquid light guide provided sample illumination, and the collection arm consisted of a variable focal length camera lens (Navitar, f = 18-108 mm) and liquid crystal tunable filter (CRi, Inc.) mounted on a cooled CCD camera (Andor, 1392 x 1040 pixel). Diffuse reflectance images were collected from 500–620 nm in 8-nm increments and calibrated with measurements of the dark offset and reflectance from a diffuse reflectance standard (Spectralon). Hemoglobin oxygen saturation was then calculated from a modified version of Beer's law that solves for the hemoglobin saturation in each pixel using linear least-squares regression [26-28, 115]. Average hemoglobin saturation values were computed for each footpad by averaging all pixels, and the ischemic footpad measurement was normalized to that of the contralateral footpad.

5.3.5.5 Perfusion imaging

Perfusion images of the footpads were acquired at days 0, 2, and 7 post-surgery with a commercial laser speckle perfusion imager (Perimed). An average perfusion value was computed for each footpad, and the ischemic footpad perfusion was normalized to that of the contralateral footpad.

5.3.5.6 Intravital imaging of vascular morphology with optical coherence tomography

At day 7 post-surgery, images of the hind limb vasculature were collected through the skin non-invasively using a swept-source optical coherence tomography (OCT) system with a 1060 nm, 100 kHz source (Axsun Technologies, Inc.) [128, 166]. Speckle variance OCT volumes [39] were collected in a 4 mm x 4 mm area covering the gastrocnemius muscle region to monitor remodeling of vessels in response to hind limb ischemia [115]. The speckle variance B-scans were processed as described previously [128, 166], and an average intensity projection over ~1.5 mm in depth was computed to visualize all vessels within the volume in a 2D image. The projection images of the vasculature were filtered to enhance contrast and connectivity [128, 132, 166], and the distribution of vessel diameters in each image was quantified.

5.3.5.7 Histological evaluation of host response to microspheres

At 7 days post-surgery, the mice were sacrificed and the gastrocnemii were removed, fixed with 10% formalin for 24 hours, and embedded in paraffin. Histological sections (4 μm) were cut and stained with hematoxylin and eosin (H&E) in order to assess the host response to the microsphere injections.

5.3.6 Statistical analysis

All data are reported as mean ± standard error of the mean (SEM). Analysis of Variance (ANOVA) with a post-hoc Tukey test for multiple comparisons was used to determine treatment

effects and $p<0.05$ was considered significant. For *in vivo* hemoglobin oxygen saturation and perfusion endpoints, an ANOVA general linear model analysis with a post-hoc Tukey test for multiple comparisons was performed to determine the treatment effect over the full time course. For comparisons between groups within individual time points, a Wilcoxon Rank Sum test was performed.

5.4 Results

5.4.1 Microsphere synthesis and characterization

5.4.1.1 Synthesis and characterization of PPS

PPS was synthesized by ring opening polymerization of propylene sulfide using ECT as initiator and TPPCl as catalyst at 60^{o}C through thioacyl group transfer (TAGT) polymerization. The molecular weight and polydispersity of PPS as determined by GPC were M_n = 17,700 g/mol and PDI = 1.36, respectively. The polymer structure was confirmed by ^{1}H NMR spectra recorded in $CDCl_3$: 1.25-1.45 (s, C**H**$_3$), 2.5-2.7 (m, C**H**), 2.85-3.0 (m, -C**H**$_2$). The polymer synthesis scheme and PPS structure are depicted in Supplemental Fig. A.1.

5.4.1.2 Microsphere characterization

Curcumin-loaded microspheres were characterized for size and morphology by SEM (Fig. 5.1). Measurements from SEM images indicated that the microspheres had an average diameter of 1.33 ± 0.55 μm (mean ± SD, n > 100). Curcumin encapsulation was qualitatively confirmed by fluorescent microscopy. Drug loading and encapsulation efficiency were 49% w/w curcumin/PPS and 40%, respectively, as determined by extraction of the drug from the microspheres using DMSO.

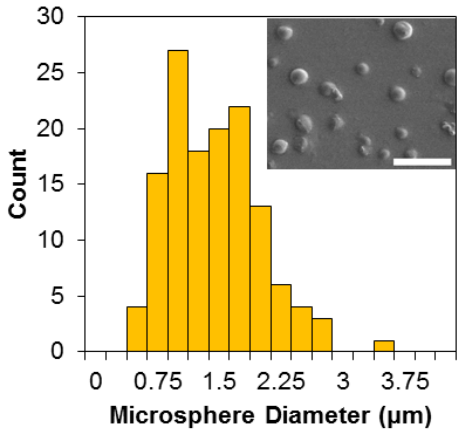

Figure 5.1: The size distribution of curcumin-PPS microspheres, as analyzed by SEM, indicated that average microparticle diameter was 1.33 µm with a standard deviation of 0.55 µm. Scale bar is 10µm.

5.4.2 Curcumin ROS-dependent release kinetics

For *in vitro* release kinetics experiments (Fig. 5.2A), the rate of curcumin release was dependent on the concentration of H_2O_2. There was little release in the absence of H_2O_2, and only approximately 20% of the curcumin was released over the entire 56-day period in PBS. For other conditions, the rate of release of curcumin correlated to the dose of H_2O_2.

On demand release of curcumin was exhibited by PPS microspheres intermittently exposed to SIN-1 which rapidly degrades (half-life of 1-2 hours [167]) to simultaneously produce nitric oxide and superoxide. These free radicals combine to form the oxidant peroxynitrite [159]. The samples were exposed to SIN-1 off/on cycles for 4 day intervals for a maximum duration of 72 days to assess whether on demand release could be achieved over an extended timeframe. When microspheres were incubated in a range of SIN-1 concentrations, including 1 mM which has been used to mimic oxidative stress conditions *in vitro* [90, 160, 168], a concentration-dependent and on demand release profile was observed (Fig. 5.2B, green bars =

+ SIN-1, white bars = no SIN-1). The slope of the release curve was higher during the SIN-1 "on" phases than the "off" phases for all doses tested. Together, the H_2O_2 and SIN-1 release experiments demonstrate ROS concentration-dependent, on demand release of the antioxidant curcumin from PPS microspheres.

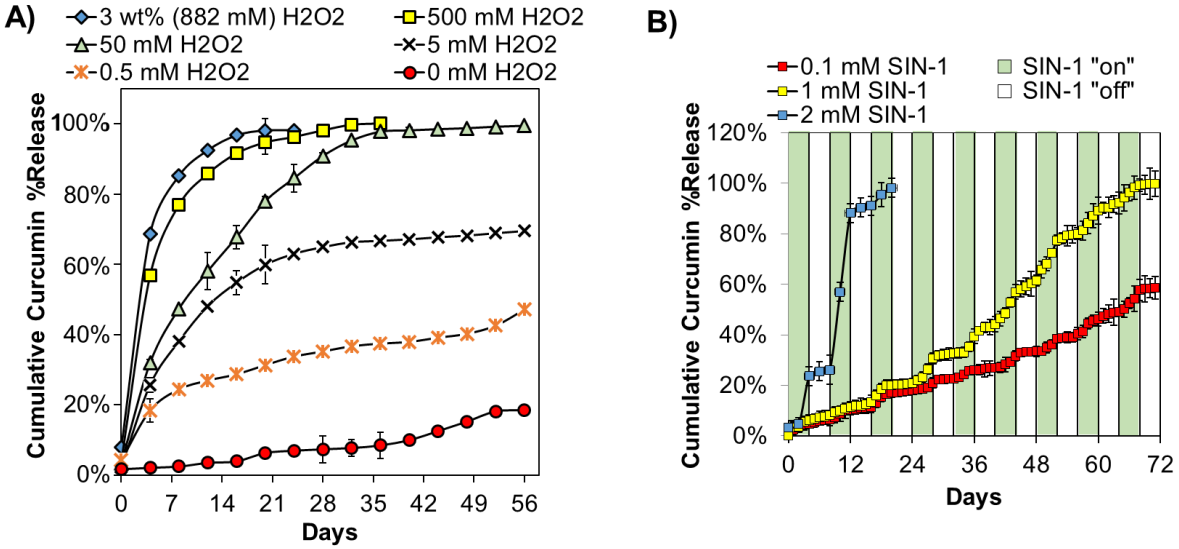

Figure 5.2: Curcumin release from PPS microparticles was ROS dose-dependent and "on demand". A) *In vitro* release of curcumin from PPS microspheres exposed to temporally-constant H2O2 concentrations ranging from 0 mM to 3 wt % (882 mM) showed H2O2 dose-dependent release . B) *In vitro* release of curcumin from PPS microspheres with intermittent exposure to 0.1 mM, 1 mM, and 2 mM SIN-1 showed SIN-1 dose-dependent, "on demand" release during temporal phases when SIN-1 was present. n=3 for all samples.

5.4.3 *In vitro* curcumin delivery

5.4.3.1 Curcumin-PPS microspheres enhance cell survival in vitro

Next, the ability of curcumin-PPS microspheres to salvage cell viability under cytotoxic levels of ROS was assessed. For a low dose of curcumin-PPS (3.4 μM curcumin, 2.5 μg/mL PPS), it was found that microspheres were cytocompatible and showed a significant therapeutic benefit up to 0.5 mM H_2O_2 ($p<0.05$) (Fig. 5.3A). At this level of ROS, both blank PPS and curcumin-PPS showed a protective effect since PPS itself scavenges H_2O_2 (Fig. 5.3A, Suppl. Fig. A.2) [88]. A higher dose of curcumin-PPS (27.1 μM curcumin, 20.4 μg/mL PPS) was then tested (Fig. 5.3B). Although approximately 40% baseline toxicity was seen in the curcumin-PPS treated cells in the absence of H_2O_2, there was a greater therapeutic effect with curcumin-PPS under higher levels of ROS (up to 1 mM H_2O_2). Blank PPS microspheres did not rescue cell viability under these higher H_2O_2 concentrations. Together, these data indicate that both blank PPS and curcumin-PPS microspheres improve cell viability under oxidative stress conditions in a dose-dependent manner. Under greater oxidative stress levels, curcumin-PPS is superior to PPS alone. The lower dose of microspheres was sufficient to improve cell survival in 0.5 mM H_2O_2 conditions without baseline cytotoxic effects, so this microsphere dose was selected for use in further *in vitro* experiments.

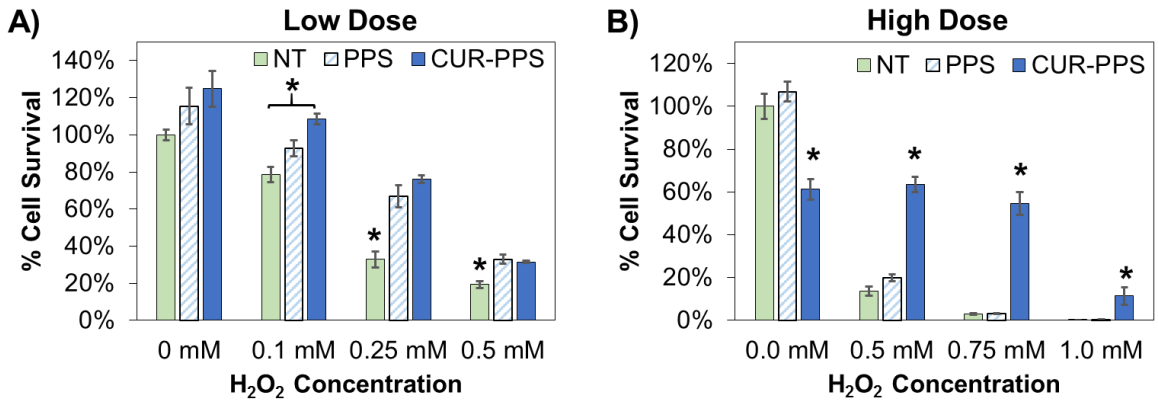

Figure 5.3: Curcumin loaded PPS microparticles reduce the cytotoxicity of H_2O_2. Cell survival was measured for luciferase-expressing 3T3 fibroblasts incubated for 24 hours with empty PPS microspheres, curcumin-PPS microspheres, or vehicle in media containing varied doses of H_2O_2. Curcumin dose is 3.4 µM in (A) and 27.1 µM in (B). Blank PPS microparticles represent the equivalent polymer dose needed to deliver the corresponding curcumin dose. *$p<0.05$ relative to other treatments within each H_2O_2 dose. n=3 /group.

5.4.3.2 Microspheres are preferentially internalized by LPS/IFN-γ-activated macrophages

In order to test whether the microparticles may preferentially target activated, phagocytic cells *in vivo* based on their physical characteristics, *in vitro* cellular internalization of curcumin-loaded PPS microspheres was assessed in 3T3 fibroblasts, RAW cells at baseline, and RAW cells activated to a pro-inflammatory M1 phenotype through a combination of LPS and IFN-γ [162, 163]. After 24 hours of treatment, confocal microscopy and flow cytometry qualitatively and quantitatively indicated that stimulated RAWs internalized the microspheres at a significantly higher rate than control cell types (Fig. 5.4A-B). Confocal microscopy z-stacks confirmed that microspheres were internalized rather than adsorbed to the outside of the cell membrane (Fig. 5.4A). Quantification of curcumin-PPS microsphere uptake with flow cytometry confirmed that

curcumin-PPS microspheres were preferentially internalized by pro-inflammatory M1 macrophages (Fig. 5.4B).

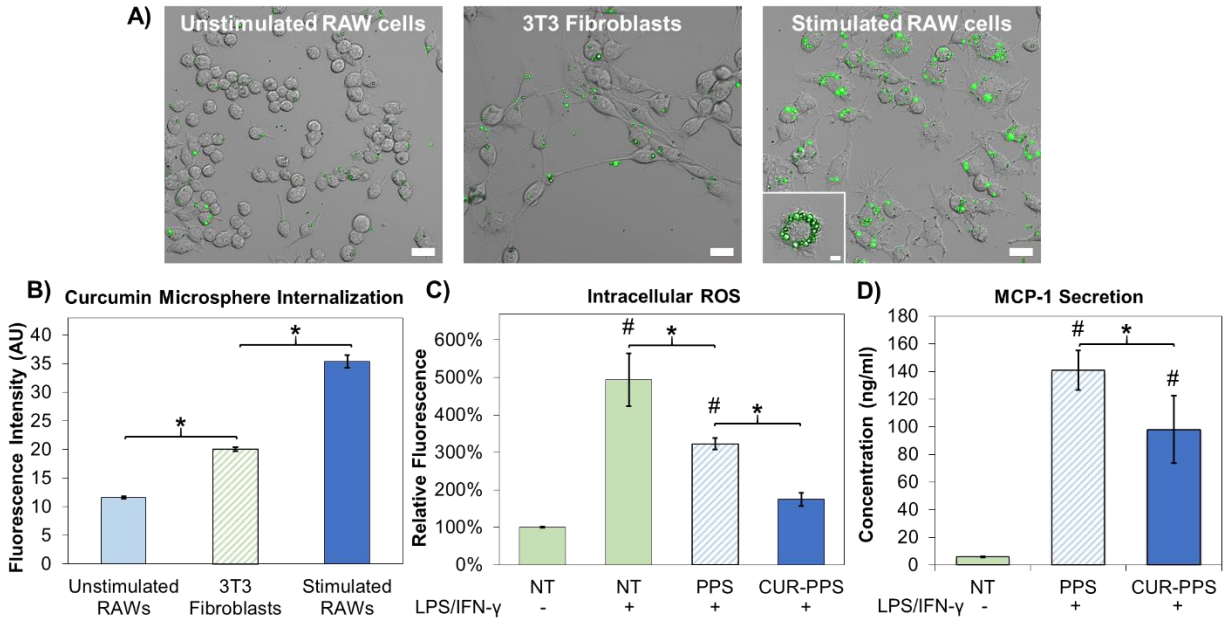

Figure 5.4: Curcumin-PPS microspheres are preferentially internalized by activated macrophages and exert functional effects on ROS generation and MCP-1 secretion. A) Confocal microscopy revealed that curcumin-PPS microspheres were internalized to a greater degree by LPS/IFN-γ stimulated RAW cells relative to non-activated macrophages and fibroblasts, suggesting size dependent targeting of the microparticles to pro-inflammatory macrophages. Scale bar is 20 μm. Inset in stimulated RAW macrophages is the center slice of a z-stack, confirming cell internalization of microspheres. Inset scale bar is 5 μm. B) Quantitative analysis of microsphere uptake was performed using flow cytometry to measure intracellular curcumin fluorescence, and significant differences were observed between all groups ($p<0.05$). C) Intracellular ROS levels are reduced in LPS/IFN-γ-stimulated RAW macrophages by treatment with PPS microspheres and Cur-PPS

microspheres ($p<0.05$). Intracellular ROS levels in activated macrophages treated with CUR-PPS microspheres were statistically equivalent to the non-activated RAW cells. D) Secretion of MCP-1 is reduced in LPS/IFN-γ-stimulated RAW macrophages by treatment with Cur-PPS microspheres relative to blank PPS microspheres ($p<0.05$). Microsphere doses contain 3.4 μM curcumin or the equivalent polymer dose. *$p<0.05$ for differences between indicated groups. #$p<0.05$ relative to unstimulated macrophages (LPS/IFN-γ(-)/NT group).

5.4.3.3 Curcumin-PPS reduces intracellular ROS levels in vitro

Curcumin-PPS microspheres exerted a functional effect on intracellular ROS levels in RAW cells activated by LPS and IFN-γ. Flow cytometry quantification of intracellular ROS showed that activated RAWs treated with either blank PPS microspheres or curcumin-loaded PPS microspheres had significantly lower levels of ROS than untreated, activated RAWs ($p<0.05$) (Fig. 5.4C). Additionally, ROS levels in activated RAWs treated with curcumin-PPS microspheres were approximately 50% lower than in blank PPS-treated cells ($p<0.05$) and statistically equivalent to ROS levels in non-activated RAW cells ($p>0.05$).

5.4.3.4 Secretion of chemokine MCP-1 is reduced by curcumin-PPS in vitro

After characterizing the antioxidant activity of both unloaded and curcumin-loaded PPS microspheres, we sought to confirm that curcumin loading provides additive anti-inflammatory activity relative to blank PPS microspheres through suppression of the NF-κB pathway [149, 150]. To do so, we compared the effect of curcumin-loaded PPS microspheres to that of blank PPS microspheres on secretion of MCP-1, an inflammatory chemokine whose expression is mediated by NF-κB activity [169, 170], in activated macrophages. Curcumin-loaded

microspheres significantly reduced MCP-1 secretion in activated macrophages in comparison to blank PPS-microspheres ($p<0.05$) (Fig. 5.4D).

5.4.4 Response to curcumin-PPS *in vivo*

5.4.4.1 Curcumin-PPS microspheres are retained locally and reduce ROS levels in the ischemic hind limb muscle

Local retention of curcumin-PPS microspheres in the hind limb muscle was assessed using an IVIS system to non-invasively image curcumin fluorescence over time after induction of hind limb ischemia (n=5 mice, representative time course in Fig. 5.5A). In the ischemic limb, curcumin was released more rapidly than in the control limb, presumably due to the increased level of ROS present during ischemia. ROS levels are increased in an untreated ischemic muscle as early as 1 day post-surgery as indicated by a greater than 2-fold increase in fluorescence of the ROS-sensitive hydrocyanine dye relative to the control muscle (Fig. 5.5B). During the 3 week period following surgery, the average curcumin fluorescence signal in the control limb remained ~4.8x greater than tissue background fluorescence, while the average ischemic limb signal decreased from 6.4x to 3.2x greater than background fluorescence by day 3 post-injection then leveled off to 2.6x from day 3 to day 21 as the limb recovered from hypoxia.

After 7 days of ischemia, the levels of ROS-sensitive fluorescence in the extracted gastrocnemius muscles were significantly lower for mice receiving treatment with either blank or curcumin-loaded PPS microspheres relative to the saline-treated group ($p<0.05$) (Fig. 5.5C). Additionally, there was a statistically insignificant trend ($p=0.07$) for decreased ROS with curcumin-PPS treatment relative to blank-PPS treatment.

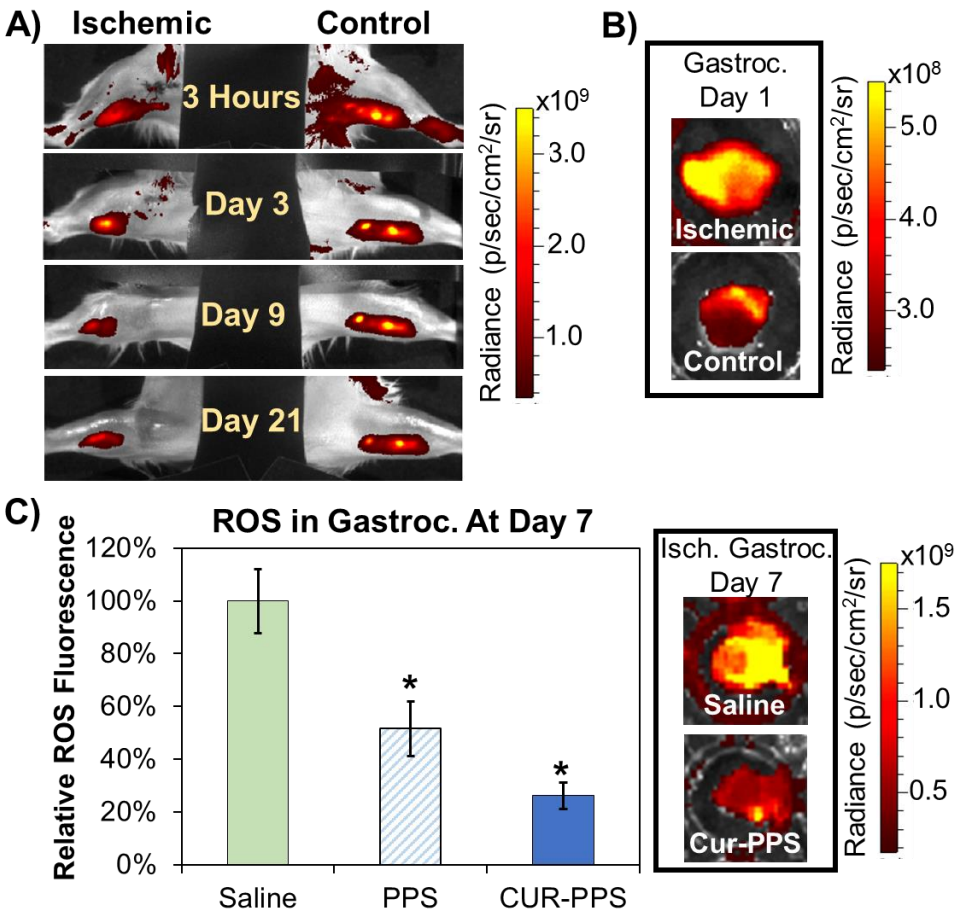

Figure 5.5: PPS microspheres provide sustained, on demand local curcumin release and reduce tissue ROS levels in the ischemic limb *in vivo.* A) Curcumin-PPS microspheres release curcumin more rapidly in the ischemic limb in comparison to the control limb. B) ROS levels in the gastrocnemius muscle are increased at day 1 post-surgery (level of ROS is 2.3-fold greater in ischemic versus control gastrocnemius). C) Blank PPS microspheres and curcumin-loaded PPS microspheres significantly reduce ROS in gastrocnemius muscles extracted from ischemic limbs. Data presented as mean ± SEM. Saline group n=8, blank PPS group n=11, curcumin-PPS group n=10. *p<0.05 relative to saline treatment.

5.4.4.2 Enhanced recovery of blood oxygenation and perfusion in the ischemic limb

Functional recovery from ischemia was evaluated over a one week period in order to assess the therapeutic effect of curcumin-PPS during a time frame in which ROS overproduction in the ischemic limb is known to occur [43, 171]. Hemoglobin oxygen saturation measured non-invasively with hyperspectral imaging (representative images Fig. 5.6A) is significantly increased in the curcumin-PPS treated group relative to the blank PPS and saline-treated groups over the time course of ischemic recovery (days 2, 4 and 6 combined, $p<0.05$) (Fig. 5.6B). At day 2, the curcumin-PPS group has a significantly higher hemoglobin saturation ratio compared to the saline group, while the PPS and saline groups are not significantly different across the time course ($p>0.9$) (Fig. 5.6B). Similarly, perfusion imaging of the footpads indicated that curcumin-PPS microsphere treatment significantly increases recovery of distal blood flow over the time course of one week relative to blank PPS treatment (days 2 and 7 combined, $p<0.05$). At day 2, the curcumin-PPS group has a significantly greater perfusion ratio than the saline and blank PPS groups (Suppl. Fig. A.3).

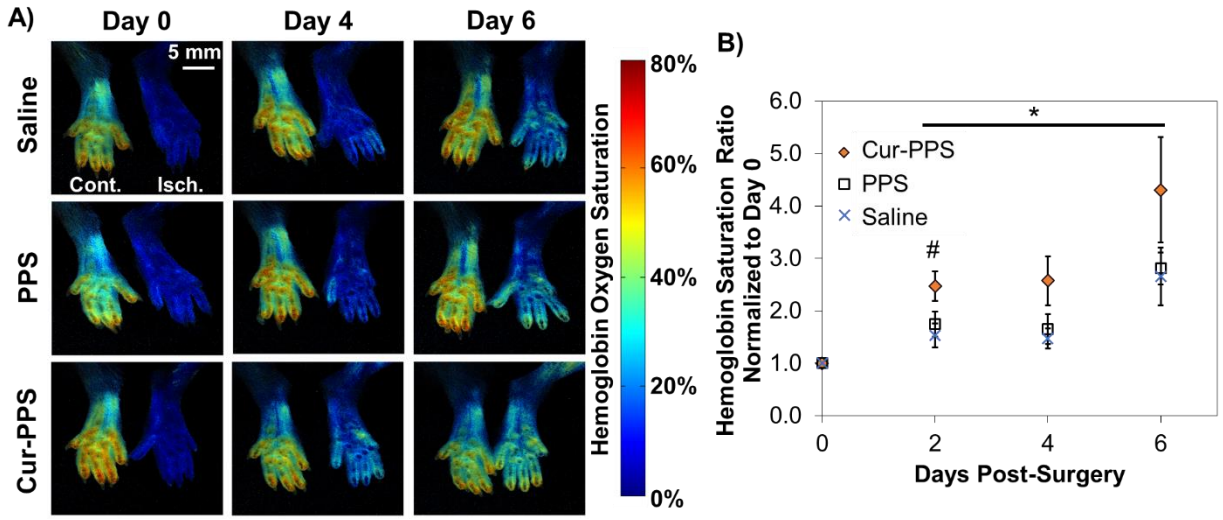

Figure 5.6: Curcumin-loaded PPS microspheres improved ischemic limb recovery in the setting of diabetes *in vivo*. A) Representative images from the time course of hemoglobin oxygen saturation recovery from each treatment group delivered to the ischemic limb of diabetic mice. B) Hemoglobin saturation is significantly increased in the curcumin-PPS treated group (n=10) relative to the blank PPS (n=11) and saline-treated (n=8) groups over the time course of ischemic recovery. At day 2, the curcumin PPS group has a significantly higher hemoglobin saturation ratio compared to the saline group. Data presented as mean ± SEM. *Cur-PPS group is significantly different from PPS and Saline groups over the time course from day 2 to 6 ($p<0.05$). PPS and Saline groups are not significantly different ($p>0.9$). #Cur-PPS and Saline differ significantly ($p<0.05$).

5.4.4.3 Intravital imaging of vascular morphology in the ischemic gastrocnemius

The effect of microsphere treatments on vessel remodeling in the ischemic hind limb was imaged non-invasively using speckle variance OCT [39, 115, 128]. Representative images in Fig. 5.7A provide visualization of vessel morphology in the gastrocnemius muscle at day 7 post-

surgery, and the diameter distribution for the curcumin-PPS treated mice showed a significant increase in the length of vasculature with diameters between 25 µm and 125 µm relative to the blank PPS microsphere group ($p<0.05$) (Fig. 5.7B).

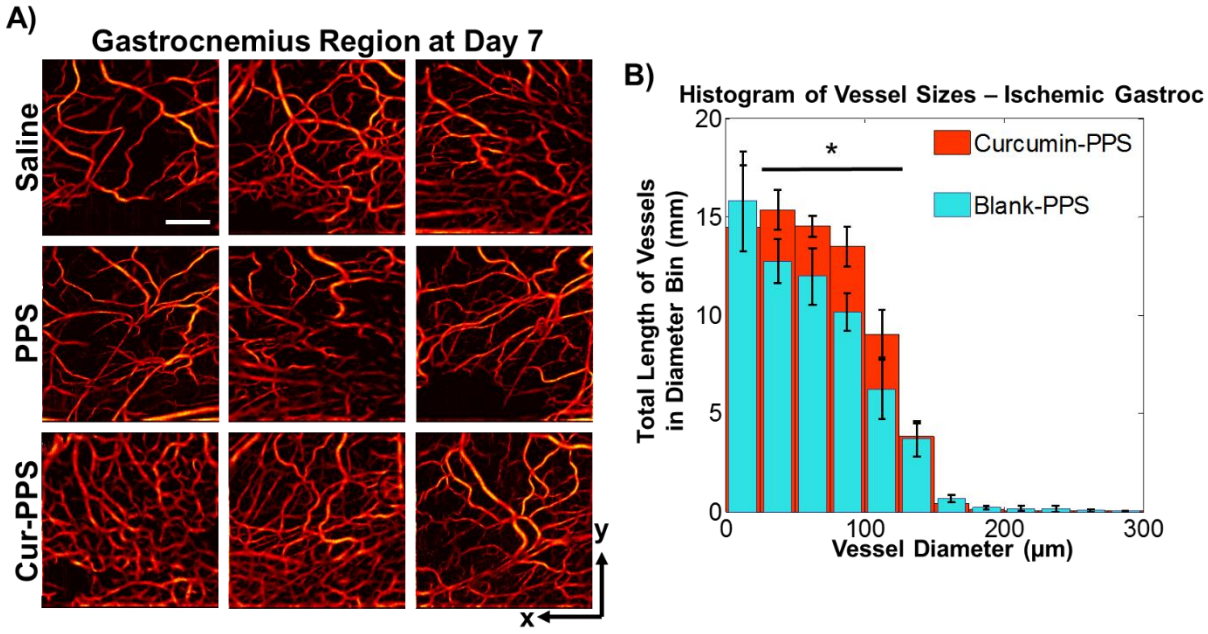

Figure 5.7: Vessel morphology was imaged non-invasively on day 7 with speckle variance OCT (n=4-5/group). A) Representative images of vessel morphology from each treatment group. Scale bar is 1 mm. B) Curcumin-PPS treated mice had a significant increase in length of vasculature with diameters between 25 µm and 125 µm relative to the blank PPS microsphere group ($p<0.05$).

5.4.4.4 Microspheres are histocompatible in the ischemic limb

H&E staining showed that the muscle status was heterogeneous across cross-sections of the ischemic limb gastrocnemius for all treatment groups at day 7 following induction of ischemia (Suppl. Fig. A.4). The majority of the muscle fibers within the gastrocnemius appeared healthy, but there were interspersed regions showing significant mononuclear cell infiltration

associated with fibrous tissue and apparent muscle fiber necrosis. These observations suggest that some negative tissue response to ischemia and/or tissue damage due to syringe insertion into the muscle was present for all groups but that there was no apparent, deleterious host response to the microsphere treatments.

5.5 Discussion

Therapies that target oxidative stress and inflammation in ischemic tissue environments have potential to improve the impaired neovascularization associated with diabetes [43, 44]. Curcumin is a promising candidate due to its demonstrated safety in humans and its combined anti-inflammatory and antioxidant properties; however, curcumin bioavailability is limited by low serum and tissue levels (irrespective of administration route), rapid metabolism, and systemic elimination [149, 151, 154]. For local delivery applications, delivery vehicles are needed that can overcome the limitations of bioavailability due to the extreme hydrophobicity and instability of free curcumin under neutral-basic pH conditions [172, 173]. Previous approaches to improving curcumin bioavailability *in vivo* have included exosomes [81] and liposomes [153] for systemic administration, and stimuli-responsive nanoparticles for local injections at sites of inflammation [82]. However, micron-sized particles may be better suited for forming a stable depot for sustained, localized delivery to an ischemic tissue site. In comparison to nanoparticles, microparticles have reduced systemic absorption and are less apt to diffuse away from the injection site, thus providing sustained, local drug release over a longer time frame [174]. Additionally, particles from 0.5 to 5 μm in diameter could be used to selectively target uptake by phagocytic cell types [175-177], as we have shown *in vitro* in activated macrophages for our particles with an average diameter of 1.3 μm (Fig. 5.4A-B). Microparticles composed of PLGA have been used to encapsulate curcumin for sustained release as a cancer

therapeutic [83]. However, the release kinetics can be affected by PLGA autocatalytic degradation, and the degradation products of PLGA cause a local acidification and inflammatory response [84, 85]. To accomplish the goals of providing sustained, local, on demand antioxidant and anti-inflammatory therapy to ischemic tissues under oxidative stress, we have pursued ROS-sensitive PPS microspheres as a delivery vehicle.

PPS was selected as the vehicle for curcumin in this application because its hydrophobicity allows for efficient encapsulation of hydrophobic curcumin via O/W emulsion, and the cargo is released in a bioresponsive, ROS-dependent manner as shown by exposure of the curcumin-loaded microspheres to H_2O_2 and SIN-1 *in vitro* (Fig. 5.2). While a bolus delivery of ROS was used for these cell free experiments in contrast to the continuous ROS generation that occurs in inflamed tissues *in vivo*, the ranges of H_2O_2 and SIN-1 doses were selected to include physiologically-relevant ROS concentrations [90] as well as higher doses that demonstrate the ROS concentration-dependency of curcumin release. Though it is difficult to precisely mimic the complex milieu of ROS present *in vivo*, the dose range of peroxynitrite-generating SIN-1 tested in this work corresponds with doses of up to 1 mM SIN-1 that have been used to mimic pathological conditions on cells [160, 168]. While some of the doses of H_2O_2 and SIN-1 used in these drug release studies may be superphysiologic, these results demonstrate that the microspheres respond to multiple sources of ROS which contribute to oxidative stress in inflamed tissues. With regards to the PPS microsphere drug-release mechanism, the hydrophobic sulfide is converted to more hydrophilic sulfoxide/sulfone by ROS-mediated oxidation [86]. We expect that this phase change causes swelling and then gradual disassembly of the PPS microparticle matrix into water soluble, unimeric polymers and that progression of this process triggers release of the microsphere cargo. Unlike PLGA, the byproducts of PPS microsphere

degradation do not acidify the local environment [84], and PPS has been safely used as a component in nanoparticle and polymersome drug carriers *in vitro* and *in vivo* [87, 90, 178].

In addition to its cytocompatibility and utility for drug loading, PPS has inherent therapeutic properties as a H_2O_2 scavenger [88]. To our knowledge, our group was the first to demonstrate the cell-protective effects of PPS in the presence of cytotoxic levels of ROS in recent work with PPS-containing hydrogels [49]. We have also observed this benefit here with our PPS microparticle-based injectable drug depot as shown in experiments with 3T3 fibroblasts (Fig. 5.3 and Suppl. Fig. A.2). Importantly, curcumin was synergistic with PPS, and the curcumin-loaded microparticles showed superior therapeutic benefit compared to blank particles under higher H_2O_2 concentrations. In this context, it is presumed that curcumin microparticles injected into tissue would remain within the tissue stroma and release therapeutic curcumin and/or scavenge extracellular ROS to reduce oxidative stress on surrounding skeletal muscle and other resident cells. However, it was also found that fabrication into micron-sized particles enabled preferential curcumin-PPS microsphere uptake by more phagocytic, activated macrophages (Fig. 5.4A-B), as these particles fall within the size range that is not efficiently internalized by non-phagocytic cell types [175-177]. This preferential targeting to inflammatory cells is desirable since these cells are the primary producers of damaging ROS and pro-inflammatory signals [144, 146, 147]. Furthermore, ROS may also be produced and accumulate in intracellular compartments such as phagosomes and endosomes/lysosomes [179], and targeting antioxidant enzymes to endocytic vesicles may be an effective approach for quenching endosomal superoxide [180]. Thus, tuning of PPS microparticle size to be optimized for phagocyte internalization may enable direct targeting to ROS at their subcellular source. In the current study, blank and curcumin-loaded PPS microspheres significantly reduced intracellular

ROS levels in activated macrophages (Fig. 5.4C). PPS microsphere-mediated ROS scavenging in living cells is a novel finding for PPS, to our knowledge, and the synergy with curcumin is in agreement with previous studies demonstrating the antioxidant effects of curcumin *in vitro* [82, 181]. Thus, these data suggest that curcumin-loaded PPS microparticles would potentially have a combined mechanism *in vivo* where curcumin would be released extracellularly and also intracellularly primarily within activated, phagocytic macrophages. Curcumin-PPS microspheres also reduced secretion of chemokine MCP-1 in activated macrophages (Fig. 5.4D), confirming anti-inflammatory activity through inhibition of the NF-κB pathway [169].

Diabetes-induced oxidative stress impairs post-ischemic neovascularization, and reduction of ROS represents a promising approach to remedy PAD [43, 44]. Curcumin is a promising candidate in this context, and it has been shown to have therapeutic benefit in preclinical models of inflammation and ischemia/reperfusion injury using delivery approaches such as systemic injection of free curcumin [152], systemic injection of exosomes [81] and liposomes [153], and local injection of stimuli-responsive nanoparticles [82]. However, sustained, ROS-demanded delivery of curcumin from a local depot has yet to be investigated in a model in which ischemia and ROS production are exacerbated by diabetes. In the current work, we have shown that *in vitro* rate of release of curcumin from PPS microparticles is modulated by environmental levels of ROS such as H_2O_2 and peroxynitrite over a sustained time frame (Fig. 5.2). This on demand delivery mechanism was also demonstrated *in vivo*. Increased ROS in the ischemic hind limb mediated rapid release of curcumin from PPS microspheres (Fig. 5.5A-B), while in the normoxic control limb, microspheres were retained at the site of injection without significant drug release over the 21-day time frame tested. The stable curcumin fluorescence signal observed in the control limb over time suggests that the microsphere depot remained intact

in the absence of pathological levels of ROS. This on demand release mechanism was also found to have significant ROS scavenging effects *in vivo,* and the curcumin-PPS microspheres significantly reduced ROS in the ischemic muscle 7 days following delivery. In this study, the blank PPS microspheres again showed an intermediate reduction of local ROS (Fig. 5.5C). These *in vivo* therapeutic studies focused on the acute phase of recovery since the control animals in this model also showed functional improvements at later time points (Fig. 5.6B and Suppl. Fig. A.3). Based on pilot studies in which free curcumin formed crystals *in vitro* (Suppl. Fig. A.5A) and exacerbated ROS levels in ischemic tissue (Suppl. Fig. A.5B), we did not pursue free curcumin treatments in this work.

The functional effects on vascular recovery in the diabetic mouse hind limb ischemia model were investigated with non-invasive optical imaging techniques [115, 128]. Hyperspectral imaging of hemoglobin oxygen saturation (Fig. 5.6), perfusion imaging of the footpads (Suppl. Fig. 5.3), and OCT of vessel morphology in the gastrocnemius (Fig. 5.7) revealed that the curcumin-PPS microspheres significantly improved recovery in this model of diabetic PAD. Controlled, on demand release of PPS and curcumin may help keep local levels of ROS within an optimal range, since both too much [43, 44, 182] and too little ROS [171, 183] are detrimental to angiogenesis and ischemic recovery. The greater functional benefit observed from curcumin-PPS microspheres relative to blank PPS particles in this study may be due to the multi-targeted effects of curcumin in addition to scavenging ROS, including inhibition of NF-κB activity, reduction of proteolytic enzyme levels, inhibition of platelet aggregation, and other anti-inflammatory, antioxidant, and antidiabetogenic effects [149]. Overall, these results are promising for the context of excessive ROS and inflammation in diabetes, and there is an

opportunity to optimize dosing and pharmacokinetics *in vivo* to achieve maximal therapeutic benefit.

5.6 Conclusions

ROS-responsive PPS microspheres were successfully utilized for encapsulation and sustained, on demand delivery of curcumin in the diabetic mouse hind limb ischemia model of peripheral arterial disease. The PPS microspheres were found to be cytocompatible, improved cell survival under exogenous oxidative stress, and reduced ROS levels *in vitro* and *in vivo*. Interestingly, blank PPS microspheres also showed some therapeutic function *in vitro*, although curcumin-loaded PPS microspheres were significantly more effective overall, especially in functional measures of recovery in the ischemic hind limb. The use of PPS microsphere-based environmentally-sensitive depots represents a compelling approach to provide on demand bioavailability of curcumin or other antioxidants for treatment of diabetic PAD or other localized tissue sites affected by chronic inflammatory diseases.

5.7 Acknowledgments

The authors thank Constance Lents, Kameron Kilchrist, Jinjoo Lee, Devin McCormack, Megan Madonna, and Chetan Patil for assistance with experiments and image processing, and Lillian B. Nanney for use of the perfusion imager. SEM was conducted through the use of the core facilities of the Vanderbilt Institute of Nanoscale Sciences and Engineering (VINSE). IVIS imaging was performed in the Vanderbilt University Institute of Imaging Science (VUIIS, supported by NCI P30 CA068485). Confocal Imaging was performed using a Zeiss LSM 510 Inverted Confocal Microscope through the use of the VUMC Cell Imaging Shared Resources, (supported by NIH Grants CA68485, DK20593, DK58404, DK59637, and EY08126).

CHAPTER 6

EVALUATING A DUAL-ANTIOXIDANT THERAPY AND THE EFFECT OF DIABETES DURATION ON THE VASCULAR RESPONSE TO ISCHEMIA

Aim 2: Apply the optical imaging platform to study the effect of diabetes on the response to ischemia

Aim 3: Apply optical imaging and conventional methods to develop new and more effective therapeutic interventions for improving HLI recovery

6.1 Abstract

A reactive oxygen species (ROS)-sensitive microsphere system consisting of poly(propylene sulfide) (PPS) and superoxide dismutase mimetic 4-hydroxy-TEMPO benzoate was synthesized through oil-in-water emulsion, and the ability to target multiple ROS was evaluated. The hydrogen peroxide (H_2O_2) and peroxynitrite-scavenging activity of PPS and the superoxide-scavenging activity of tempo benzoate were confirmed *in vitro* using cell-free, ROS-producing systems. A mouse model of diabetic peripheral arterial disease (PAD) with a significant therapeutic window for reducing oxidative stress and improving the vascular response to hind limb ischemia was identified for use in evaluating the effects of the tempo-PPS microspheres *in vivo*. Both blank PPS and tempo-PPS microspheres improved recovery from hind limb ischemia as measured by functional endpoints of hemoglobin saturation and perfusion in the footpads and vessel morphology in the proximal limb acquired using non-invasive imaging techniques. These results suggest that targeting H_2O_2 and peroxynitrite in this model with a local depot of PPS is an effective strategy for improving the impaired vascular response associated with chronic hyperglycemia. Overall, this work validates the use of the PPS microsphere system as a promising therapeutic treatment for diabetic PAD and other pathologies with localized oxidative stress.

6.2 Introduction

Diabetes is known to be a major cardiovascular risk factor, and peripheral arterial disease (PAD) is a common comorbidity [41, 56]. In addition to its association with an increased risk of critical limb ischemia, ulceration, and limb amputation [2, 15], diabetes complicates the treatment of PAD by causing diffuse, systemic manifestation of disease, increased surgical complications, longer hospitalization, and lower rates of amputation-free survival [184]. The link between diabetes and vascular dysfunction has been well established, with hyperglycemia, oxidative stress, formation of advanced glycation end products, and protein kinase C production considered to be among the important factors [56, 184].

Oxidative stress in particular has been identified as a common process linking the various pathways of hyperglycemia-induced pathologies [56]. Overproduction of reactive oxygen species (ROS) is implicated in diabetic vascular dysfunction through several mechanisms, including impaired shear stress-mediated activity of extracellular-signal-regulated kinase-5 (ERK5) through post-translational modification [185], impaired hypoxia-inducible factor 1 (HIF-1) function by modification of HIF-1α by methylglyoxal [44], impaired endothelial progenitor cell function [186], decreased nitric oxide (NO) bioavailability due to its reaction with superoxide forming peroxynitrite [187], and eNOS uncoupling due to upregulation of NADPH oxidases and eNOS and subsequent oxidation of eNOS cofactor tetrahydrobiopterin (BH_4) by peroxynitrite [43, 187, 188]. Due to the complexity of the pathways through which diabetes impairs angiogenesis and arteriogenesis, new therapies for diabetic PAD should have a multi-level effect and target an upstream factor such as eNOS or overproduction of ROS [56, 184, 187]. Administration of vitamins C and E for reducing oxidative stress has been tested in large-scale clinical trials, but long-term results regarding their effect on cardiovascular outcome have proven

disappointing compared with preclinical studies [56, 187, 189]. However, antioxidant therapies using low-molecular-weight compounds that act as superoxide dismutase (SOD) or catalase mimetics may be promising due to the advantage of catalytically scavenging ROS continuously, rather than acting in a stoichiometric manner [44, 56, 190].

Preclinical studies have demonstrated improvement of vascular function and the response to ischemia through treatment with SOD mimetics in models of elevated ROS production [44, 182, 191, 192]. However, these treatments are often administered via systemic injection or in drinking water, which requires multiple injections and/or continuous delivery. Sustained delivery depots may be more convenient for patients with localized disease and will help to minimize off-target effects that can occur such as impairment of the mitochondrial electron transport chain [193, 194]. Several particle-based systems have been employed to improve delivery of native SOD and catalase enzymes [180, 195-198] including a hybrid system consisting of SOD conjugated to polysulfide-containing micelles [88]. Recently, polymeric systems have also been investigated for delivery of SOD mimetics including nanoparticles with nitroxide radical moieties [199], hydrogels containing nitroxide radicals [193], and pH-responsive microparticles [200]. Here we build from these concepts to develop and test multi-ROS scavenging particles composed of a hydrogen peroxide and peroxynitrite-scavenging poly(propylene sulfide) (PPS) matrix encapsulating a synthetic SOD mimetic in a diabetic PAD model.

Previously, we demonstrated the utility of an ROS-responsive, hydrogen peroxide (H_2O_2)-scavenging microsphere system for delivery of hydrophobic drugs such as the anti-inflammatory and antioxidant molecule curcumin from a local depot [91]. This system is based on PPS, which undergoes a phase change from a hydrophobic to a hydrophilic state upon oxidation [86], permitting on-demand release of encapsulated drug [49, 90]. In addition to the

therapeutic effects of curcumin, the PPS alone was shown to scavenge ROS *in vitro* and in ischemic muscle, although unloaded PPS microspheres did not induce a functional improvement in the vascular response to ischemia [91]. In the present work, we have characterized the ROS scavenging capabilities of encapsulated hydrophobic nitroxide radical (4-hydroxy-TEMPO benzoate) in PPS microspheres for dual-targeting of both superoxide and H_2O_2 and have extended functional testing into a more relevant animal model of sustained diabetes.

6.3 Materials and Methods

6.3.1 Materials

All chemicals were purchased from Sigma-Aldrich (St. Louis, MO, USA) except the following. Propylene sulfide (>96%) was purchased from Acros Organics through Fisher Scientific (Pittsburgh, PA, USA) and was purified by distillation just before polymerization. Dihydroethidium (DHE) and Amplex Red Hydrogen Peroxide/Peroxidase Assay kit were purchased from Thermo Fisher Scientific (Molecular Probes, Waltham, MA, USA). Peroxynitrite was purchased as a solution in 0.3 M sodium hydroxide from Cayman Chemical (Ann Arbor, MI, USA).

6.3.2 Microsphere synthesis

6.3.2.1 Synthesis of poly(propylene sulfide) (PPS)

Poly(propylene sulfide) (PPS) was prepared as previously described [49] by anionic polymerization of propylene sulfide using DBU/1-buthane thiol as an initiator. Briefly, in a dried and nitrogen flushed 50 mL RB flask, 1,8-diazabicyclo[5.4.0]undec-7-ene (DBU) (4.5 mmol, 0.673 mL) in dry tetrahydrofuran (THF) (25 mL) was degassed for 30 minutes, and the reaction mixture temperature was lowered to 0°C. To this flask, a 30 minute degassed solution of 1-butane thiol (1.5 mmol, 0.161 mL) in THF (20 mL) was added drop wise and allowed to react for

30 minutes. Later, freshly distilled and degassed propylene sulfide (120 mmol, 9.39 mL) monomer was added to the reaction mixture, and the temperature was maintained at 0°C for 2 h. The reaction was quenched by addition of 2-iodoethanol (2 mmol, 0.40 g) and stirred overnight at RT. The next day, the polymer solution was filtered to remove precipitated salt and further purified by three precipitations into cold methanol before vacuum-drying to yield a colorless viscous polymer.

6.3.2.2 Characterization of PPS

PPS was characterized for structure, molecular weight, and polydispersity as described previously [49, 91]. The number average molecular weight (M_n) and polydispersity (PDI) of PPS were assessed by gel permeation chromatography (GPC, Agilent Technologies, Santa Clara, CA, USA) using dimethylformamide (DMF) + 0.1 M lithium bromide mobile phase at 60°C through three serial Tosoh Biosciences TSKGel Alpha columns (Tokyo, Japan). An Agilent refractive index (RI) and Wyatt miniDAWN TREOS light scattering (LS) detector (Wyatt Technology Corp., Santa Barabara, CA, USA) were used to calculate absolute molecular weight based on dn/dc values experimentally determined through offline injections into the RI detector. The chemical structure of the PPS was analyzed by ^{1}H nuclear magnetic resonance spectroscopy (NMR) recorded in $CDCl_3$ with a Brüker 400 MHz spectrometer. ^{1}H NMR (400 MHz; $CDCl_3$, δ): = 1.3-1.4 (s, CH_3), 2.5-2.8 (s, -CH), 2.8-3.1 (s, CH_2), 3.72 (t, CH_2-OH).

6.3.2.3 Microsphere fabrication and drug loading

PPS microspheres encapsulating tempo-benzoate (referred to as "tempo-PPS" microspheres) were prepared using a modification of the oil-in-water (O/W) emulsion solvent evaporation method [83, 155] as described previously [91]. Briefly, tempo-benzoate (5 mg) and PPS (60 mg) were dissolved in chloroform (1 mL) and ultrasonicated (Cole-Parmer, USA) until

both PPS and tempo-benzoate were completely dissolved to form the oil (O) phase. The O phase was then added drop-wise in 1% (w/v) aqueous poly(vinyl alcohol) (PVA) solution (7 ml) and emulsified using an Ultra-Turrax TP 18-10 homogenizer (Janke and Kunkel KG, IKA-WERK) at 20,000 rpm for 1 minute. The emulsion was transferred to a round-bottom flask and subjected to high vacuum (~635 mm Hg) using a rotary evaporator (Rotavapor RII, BUCHI, Switzerland) for one hour to remove the chloroform. Microspheres were then recovered by centrifuging the remaining aqueous solution at 7500xg for 8 minutes. The microspheres were then washed once with deionized water to remove excess PVA. To remove free tempo-benzoate crystals, the microspheres were filtered using a Buchner flask and funnel with a fritted disk (10-15 μm porosity) (Sigma-Aldrich, St. Louis, MO, USA). Lastly, the microspheres were lyophilized (Labconco Freezone 4.5, USA) prior to storage. Unloaded blank PPS microspheres were made using the same protocol without the addition of tempo-benzoate. This method produces microspheres with an average diameter of ~1.3 μm [91].

6.3.2.4 Microsphere characterization

Tempo-benzoate loading efficiency in the microspheres was determined using high performance liquid chromatography (HPLC). Lyophilized microspheres were dissolved in HPLC grade acetonitrile (with the aid of heating and ultrasonication) and the solution was filtered. Tempo-benzoate concentration was measured using a Luna® 5 μm C18(2) 100Å, 250 x 4.6 mm semi-prep column (Phenomenex, Torrance, CA, USA) under a linear gradient from 90% water (0.05% formic acid), 10% acetonitrile to 5% water (0.05% formic acid), 95% acetonitrile over 30 minutes. Absorbance of tempo-benzoate was measured at 425 nm after establishing that there was no absorbance interference from a filtered blank PPS sample under the same conditions. Drug incorporation efficiency was expressed as drug content (mass of tempo-benzoate / mass of

microspheres) and drug encapsulation efficiency ((actual tempo-benzoate mass / microspheres mass) / (input tempo-benzoate mass / total mass of PPS and tempo-benzoate)).

6.3.3 ROS scavenging activity of microspheres *in vitro*

6.3.3.1 Superoxide scavenging in vitro

In vitro superoxide scavenging activity of the tempo-PPS microspheres was evaluated using a dihydroethidium (DHE) fluorescence assay. DHE has been widely used to detect superoxide, which reacts with DHE to form a specific fluorescent product, 2-OH-ethidium (2OH-E) [201, 202]. The effects of PPS and tempo-benzoate on superoxide were determined using a superoxide-generating, cell-free enzymatic system containing 0.046 U/ml xanthine oxidase and 0.2 mM xanthine. Xanthine was prepared in PBS-/- as a stock solution (1.21 mg/mL), and the appropriate volume of xanthine stock solution was added to the xanthine oxidase solution to reach the required final concentration. The xanthine / xanthine oxidase solution (100 µL) was added to wells in a black-walled, 96-well plate containing the following treatments: PBS, blank PPS microspheres (55 µg/mL), free tempo-benzoate (dissolved in acetonitrile then diluted to 5% acetonitrile, 55 µg/mL tempo-benzoate), and tempo-PPS microspheres (55 µg/mL microsphere concentration). Each well contained 10 µL of a treatment. 20 uM DHE from dimethylsulfoxide (DMSO) stock solution was freshly prepared in PBS with a final DMSO content of 0.2%. After 10 minutes, 100 µL of the DHE solution was added to each well (10 uM final DHE concentration) and the fluorescence intensity was measured in a plate reader (Tecan Group Ltd., Mannedorf, Switzerland) over a time frame of 1 hour with an excitation of 405 nm and an emission of 570 nm. These excitation/emission wavelengths were selected in order to improve the specificity of the assay for measuring the superoxide-specific product of DHE oxidation [202]. Specificity of the assay for superoxide detection was confirmed

by using bovine SOD (20 U/ml) as a negative control treatment in a well containing xanthine / xanthine oxidase and DHE.

6.3.3.2 Hydrogen peroxide scavenging in vitro

H_2O_2-scavenging activity of the PPS microspheres was verified *in vitro* using an Amplex Red Hydrogen Peroxide/Peroxidase Assay kit according to the manufacturer's instructions. Xanthine and xanthine oxidase were used at the same concentrations as described in the DHE assay to generate a reaction solution containing both superoxide and hydrogen peroxide. The reaction solution was added to wells in a black-walled, 96-well plate containing either PBS, blank PPS microspheres (final concentrations of 60 µg/mL and 7 µg/mL), or free tempo-benzoate (final concentrations of 0.5 mg/mL and 60 µg/mL). The Amplex Red working solution was freshly prepared as described in the kit instructions using the included Amplex Red, horseradish peroxidase, and 1x reaction buffer. The working solution was then added to the wells and fluorescence was measured in a plate reader at 1 hour with an excitation of 530 nm and an emission of 590 nm.

6.3.3.3 Peroxynitrite scavenging in vitro

The ability of PPS microspheres to scavenge peroxynitrite was tested *in vitro* using a Pyrogallol Red (PGR) bleaching assay. Treatment groups consisting of PBS, blank PPS microspheres (0.5-1.5 mg/mL), tempo-PPS microspheres (0.5 mg/mL), tempol (0.2 mg/mL, hydrophilic analog of tempo-benzoate), and ascorbic acid (negative control, pH adjusted to 7.4) were prepared in a 48-well plate with 500 µL volume per well. A PGR stock solution was prepared in PBS (0.025 µM) and 10 µL was added to each well. Peroxynitrite stock solution was thawed on ice and diluted to a concentration of 1 mM in 0.3 M NaOH. After baseline absorbance

of the dye was measured in a plate reader at 540 nm, 5 µL of peroxynitrite was added to each well (final concentration of 10 µM) and absorbance measurements were collected for one hour.

6.3.4 *In vivo*

6.3.4.1 Diabetes model development

Three variations on a Type 1 diabetes model were compared prior to selecting the model for the therapeutic studies. In all three variations, male FVB mice (Jackson Laboratory) were given daily intraperitoneal injections of streptozotocin (STZ, 50 mg/kg) for 5 consecutive days after a 5 hour fast [164]. One group was given STZ at 9 weeks of age and was hyperglycemic for 5 weeks prior to surgical induction of ischemia. The second group was given STZ at 9 weeks of age, but surgery was delayed until 15 weeks of hyperglycemia. The third group was given STZ at 19 weeks of age, and underwent surgery after 5 weeks of hyperglycemia (at same age as second group). The three groups are respectively referred to as the "younger cohort", "older cohort – 15 weeks diabetic", and "older cohort – 5 weeks diabetic". Non-diabetic mice that were age-matched to the younger and older cohorts at the time of surgery were included to assess the effects of hyperglycemia in each variation of the model. In all groups, fasting blood glucose levels were measured via tail prick at the onset of hyperglycemia following the STZ treatment, and again at the time of surgery (AlphaTrak 2 monitor, Abbott). Mice with levels above 300 mg/dL were considered diabetic.

6.3.4.2 Mouse hind limb ischemia model

After 5 or 15 weeks of hyperglycemia, hind limb ischemia [11] was surgically induced in diabetic and age-matched non-diabetic mice as described previously [91]. Briefly, the femoral artery and vein of the right hind limb were ligated with 6-0 sutures proximal to the origins of the superficial epigastric artery and deep branch of the femoral artery, and proximal to the vessels

the branch from the femoral artery near the knee. Major side branches were also ligated with 6-0 sutures before the ligated segment of the femoral artery and vein was excised. The incision was closed with interrupted 5-0 nylon sutures. In therapeutic experiments, treatments were injected intramuscularly in the ischemic limb following closure of the skin incision. Treatment injections were administered in a total of 100 µL divided among 3 injection sites in the adductor muscle and 3 injection sites in the gastrocnemius muscle. Surgery was performed under isoflurane anesthesia at normal body temperature. Analgesia was administered subcutaneously pre-operatively and every 24 hours post-operatively until animals exhibited normal appearance and behavior (5-10 mg/kg ketoprofen). Mice were fed a standard chow diet *ad libitum* with free access to water. All protocols were approved by the Institutional Animal Care and Use Committee of Vanderbilt University and done in accordance with the National Institute of Health's *Guide for the Care and Use of Laboratory Animals.*

6.3.4.3 ROS measurement in extracted muscle tissue

After 8 or 14 days of ischemia, the gastrocnemius and adductor muscles were extracted immediately post-mortem and dissected pieces of tissue were weighed and transferred into Krebs HEPES Buffer (pH 7.35) on ice. Amplex Red working solution was prepared using components from the Molecular Probes Amplex Red Hydrogen Peroxide/Peroxidase Assay kit as follows: 1 vial of Amplex Red (154 µg) was dissolved in 60 µL DMSO and added to 11.82 mL of Krebs HEPES Buffer along with 120 µL of horseradish peroxidase (from a stock solution of 10 U/ml in 0.05 M sodium phosphate at pH 7.4). 300 µL of working solution was added to each well in a 48-well plate. Tissue samples were transferred into the Amplex Red solution and incubated in the dark for 1 hour at 37 °C. Tissue samples weighing approximately 20 mg were used to ensure proper H_2O_2 diffusion out of the tissue. A standard curve of hydrogen peroxide was prepared in a

black-walled 96-well plate at the same time that the tissue incubation began. After 1 hour, 150 µL of solution from each sample was transferred to the black 96-well plate and Amplex Red fluorescence was measured on an IVIS imaging system (Lumina Series III, PerkinElmer) with 530/590 nm excitation/emission filters. Tissue hydrogen peroxide concentration was normalized to tissue mass, and ischemic limb values were normalized to the contralateral control muscle for each animal.

6.3.4.4 Hyperspectral imaging of hemoglobin oxygen saturation

Hemoglobin oxygen saturation (HbSat) was measured in the footpads of the hind limbs using hyperspectral imaging as described previously [91, 115] at days 0, 3, 7, 14, 21, and 28 post-surgery. Briefly, diffuse reflectance images were collected in the visible light range from 500 to 620 nm in 8-nm increments using a liquid crystal tunable filter (CRi, Inc.) mounted on a cooled CCD camera (Andor, 1392 x 1040 pixel) with a variable focal length camera lens (Navitar, f = 18-108 mm). Illumination was provided by a halogen lamp. HbSat was calculated for each image pixel using a modified version of Beer's law [27, 28, 115]. Average HbSat values were computed for each footpad, and the ischemic footpad HbSat was normalized to that of the contralateral footpad for each animal.

6.3.4.5 Perfusion imaging

Perfusion images of the footpads were acquired at days 0, 3, 7, 14, 21, and 28 post-surgery with a laser Doppler perfusion imager (LDPI) (Perimed PeriScan PIM II). An average perfusion value was computed for each footpad, and the data are presented as the ratio of the ischemic footpad perfusion to that of the control footpad for each animal.

6.3.4.6 Intravital imaging of vascular morphology with optical coherence tomography

At 0, 3, 7, 14, 21, and 28 days post-surgery, the hind limb vasculature in the adductor and gastrocnemius muscle regions was imaged using a swept-source optical coherence tomography (OCT) system as described previously [91, 166]. The OCT system has a 100 kHz source with a center wavelength of 1060 nm (Axsun Technologies, Inc.). Speckle variance OCT volumes were acquired non-invasively through the skin in 4 mm x 4 mm areas covering the two muscle regions, and average intensity projections in depth were used to visualize all vessels detected within the imaged volume. After image processing was performed to enhance contrast and enable vessel segmentation [128, 166], morphological parameters including vessel area density (total area filled by vessels / total area of imaged region) and vessel length fraction (total vessel length / total area of imaged region) were quantified.

6.3.4.7 Histological evaluation of response to microspheres

A subset of mice from each treatment group was sacrificed at day 8 post-surgery. The gastrocnemius and adductor muscles were removed, and a portion of each muscle was fixed with 10% formalin for 24 hours and embedded in formalin. Histological sections (5 μm) were cut for CD68 (MCA1957, Bio-Rad, Raleigh, NC) and nitrotyrosine (AB5411, Millipore, Billerica, MA) immunohistochemistry (Supplemental Methods in Appendix B).

6.3.5 Statistical analysis

All data are reported as mean ± standard error of the mean (SEM). Kruskal-Wallis Analysis of Variance (ANOVA) with a post-hoc Tukey test for multiple comparisons was used to determine treatment effects and $p<0.05$ was considered significant. For comparisons between only two groups, a Wilcoxon Rank Sum test was used. For longitudinal imaging endpoints, an

ANOVA general linear model analysis was performed to model the response curves and compare treatment effects at each time point. $p<0.05$ was considered significant.

6.4 Results

6.4.1 Microsphere synthesis and characterization

6.4.1.1 Synthesis and characterization of PPS

PPS was synthesized by anionic polymerization of propylene sulfide as described previously [49] and depicted in Suppl. Fig. B.1.The molecular weight and polydispersity of PPS as determined by GPC were M_n = 5000 g/mol and PDI = 1.3, respectively. The polymer structure was confirmed by ^{1}H NMR spectra recorded in $CDCl_3$: 1.3-1.4 (s, CH_3), 2.5-2.8 (s, -CH), 2.8-3.1 (s, CH_2), 3.72 (t, CH_2-OH).

6.4.1.2 Microsphere characterization

Tempo-benzoate loading efficiency in the microspheres was quantified using HPLC to measure tempo-benzoate concentration in dissolved microspheres. Drug content was 5.5% w/w tempo-benzoate/microspheres and drug encapsulation efficiency was 71% (average of 2 independent batches of microspheres).

6.4.2 ROS-scavenging *in vitro*

ROS-dependent drug release from the PPS microspheres upon exposure to both H_2O_2 and peroxynitrite has been previously demonstrated by our lab using curcumin as a model hydrophobic drug [91]. Here, the ROS-scavenging activity of the microspheres and the encapsulated tempo-benzoate was evaluated using assays for detection of superoxide, hydrogen peroxide, and peroxynitrite. A schematic of how the synthetic system mimics the native superoxide dismutase / catalase system is shown in Suppl. Fig. B.1C.

6.4.2.1 Free and encapsulated tempo-benzoate scavenge superoxide in vitro

The superoxide scavenging activity of the tempo-PPS microspheres was evaluated in a cell free xanthine/xanthine oxidase system using fluorescence of oxidized DHE to measure superoxide [202]. Compared to no treatment, blank PPS microspheres do not reduce the fluorescent signal from the DHE oxidation product, while both free tempo-benzoate and tempo-PPS microspheres significantly reduce fluorescence (Fig. 6.1A) (one-way ANOVA $p<0.0001$). The fluorescent signal is further inhibited in the presence of SOD as a negative control (data not shown).

6.4.2.2 PPS microspheres scavenge H_2O_2 in vitro

The H_2O_2-scavenging activity of PPS was confirmed using Amplex Red as a reporter molecule in a xanthine/xanthine oxidase system that produces both superoxide and H_2O_2. Treatment with blank PPS microspheres significantly reduces Amplex Red fluorescence, while treatment with free tempo-benzoate significantly increases the fluorescent signal after 1 hour of incubation as tempo-benzoate converts superoxide into H_2O_2 (Fig. 6.1B) (one-way ANOVA $p<0.001$).

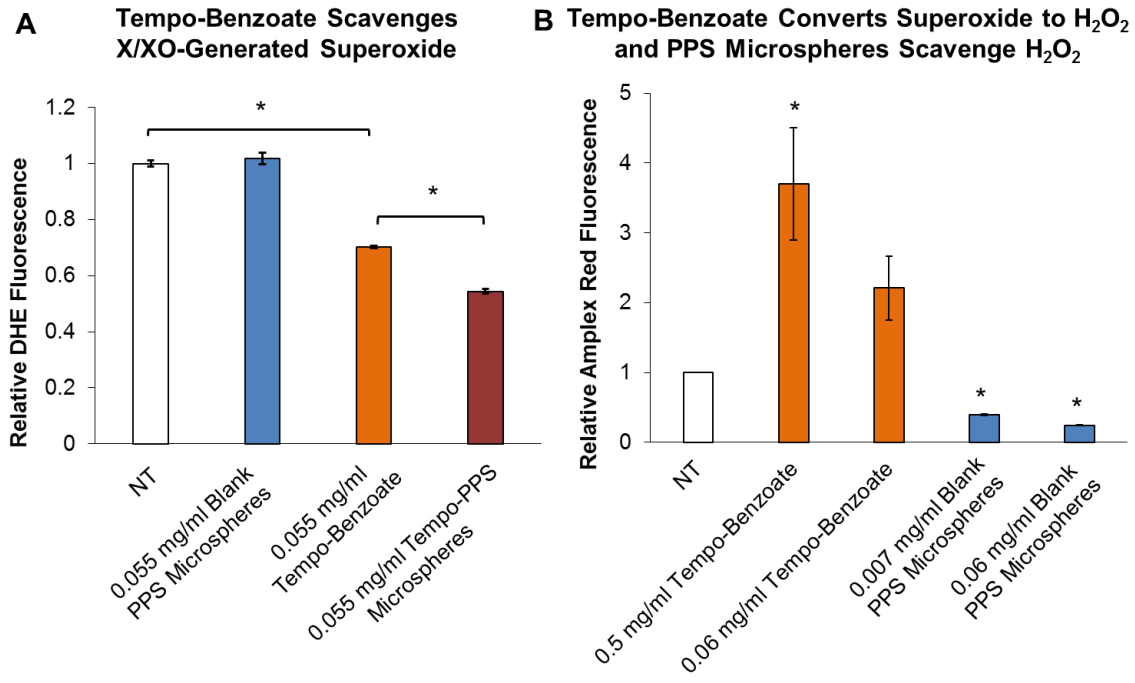

Figure 6.1: Free and encapsulated tempo-benzoate scavenge superoxide, while blank PPS microspheres scavenge H_2O_2 *in vitro*. A) Free tempo-benzoate and tempo-PPS microspheres significantly reduce fluorescence from oxidized DHE relative to no treatment and blank PPS microspheres in a superoxide-generating system containing xanthine and xanthine oxidase (one-way ANOVA $p<0.0001$, *significant post-hoc comparison). B) Blank PPS microspheres significantly reduce Amplex Red fluorescence in a superoxide and H_2O_2-producing xanthine/xanthine oxidase system. Tempo-benzoate treatment significantly increases Amplex Red fluorescence as the superoxide in the system is converted to H_2O_2 (one-way ANOVA $p<0.001$, *significant post-hoc comparison relative to no treatment). Data presented as mean ± SD.

6.4.2.3 PPS microspheres have peroxynitrite scavenging activity that protects PGR from bleaching

Pyrogallol Red is bleached in the presence of peroxynitrite, and this bleaching effect can be reduced or inhibited by antioxidant compounds such as ascorbic acid [203]. In the presence of blank-PPS and tempo-PPS microspheres, PGR is protected from bleaching in a dose-dependent manner (Fig. 6.2, one-way ANOVA $p<0.0001$). Tempol, a hydrophilic analog of tempo-benzoate, shows that the nitroxide radical provides no protection for PGR from peroxynitrite. Ascorbic acid was tested as a negative control and resulted in only 2% relative bleaching (nearly complete protection for PGR from peroxynitrite) (data not shown).

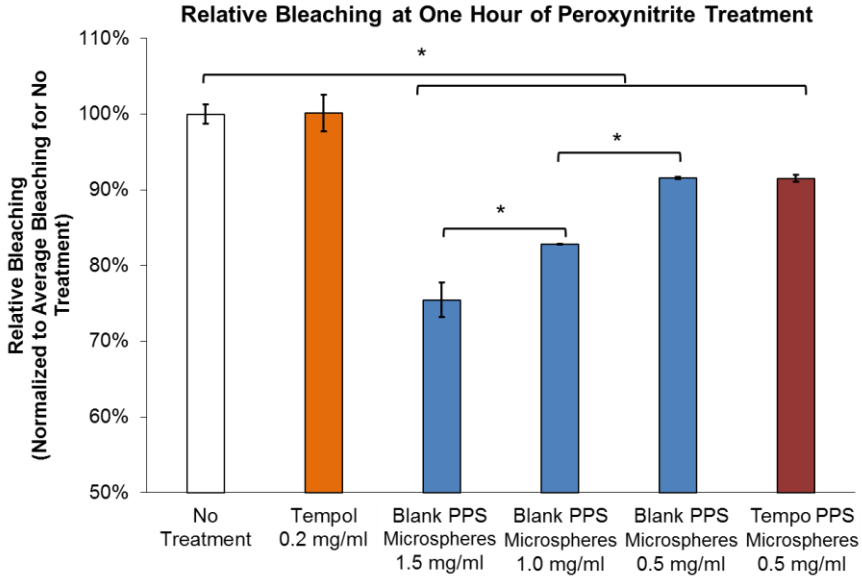

Figure 6.2: Blank PPS and tempo-PPS microspheres protect PGR from bleaching by peroxynitrite in a dose-dependent manner (one-way ANOVA $p<0.0001$, *significant post-hoc comparisons). Doses are presented as microsphere mass / volume. Data presented as mean ± SD.

6.4.3 Diabetes model characterization

Three induction protocols were compared for the STZ-induced model of Type 1 diabetes prior to selecting a model for therapeutic studies with tempo-PPS microspheres. The three variations consisted of 5 weeks of hyperglycemia in a younger cohort, 15 weeks of hyperglycemia in an older cohort, and 5 weeks of hyperglycemia in an older cohort. Age-matched, non-diabetic mice were included in both the younger (~15 weeks old at time of surgery) and older (~25 weeks old at time of surgery) cohorts.

6.4.3.1 Hemoglobin saturation and perfusion recovery in diabetes models

Longitudinal recovery of hemoglobin oxygen saturation (HbSat) in the footpads was measured using hyperspectral imaging. In the younger cohort, the diabetic mice responded to ischemia with a significant "overshoot" response in comparison to the age-matched non-diabetic mice ($p<0.05$ with a rank sum test at days 14, 21, and 28). This response peaks at day 14 and is followed by regression in the HbSat ratio (Fig. 6.3A). In contrast, the older cohort does not have any significant differences between groups with the exception of a higher HbSat ratio in the group with 15 weeks of hyperglycemia at day 14 ($p<0.05$ between 15-week diabetic mice and 5-week diabetic mice), and the HbSat ratio is highest at day 28 post-surgery (Fig. 6.3B).

The footpad perfusion ratio was imaged over time using LDPI. In the younger cohort, an early overshoot response is apparent in the diabetic mice ($p<0.05$ at days 7, 14, and 28 compared to non-diabetic, age-matched mice) (Fig. 6.3C). In a manner similar to the HbSat response, this overshoot peaks early in the time course (day 7) and is followed by regression of the LDPI ratio. In the older cohort of mice, there are no significant differences between the groups at any point in the time course, and the LDPI ratio peaks at day 21 (Fig. 6.3D).

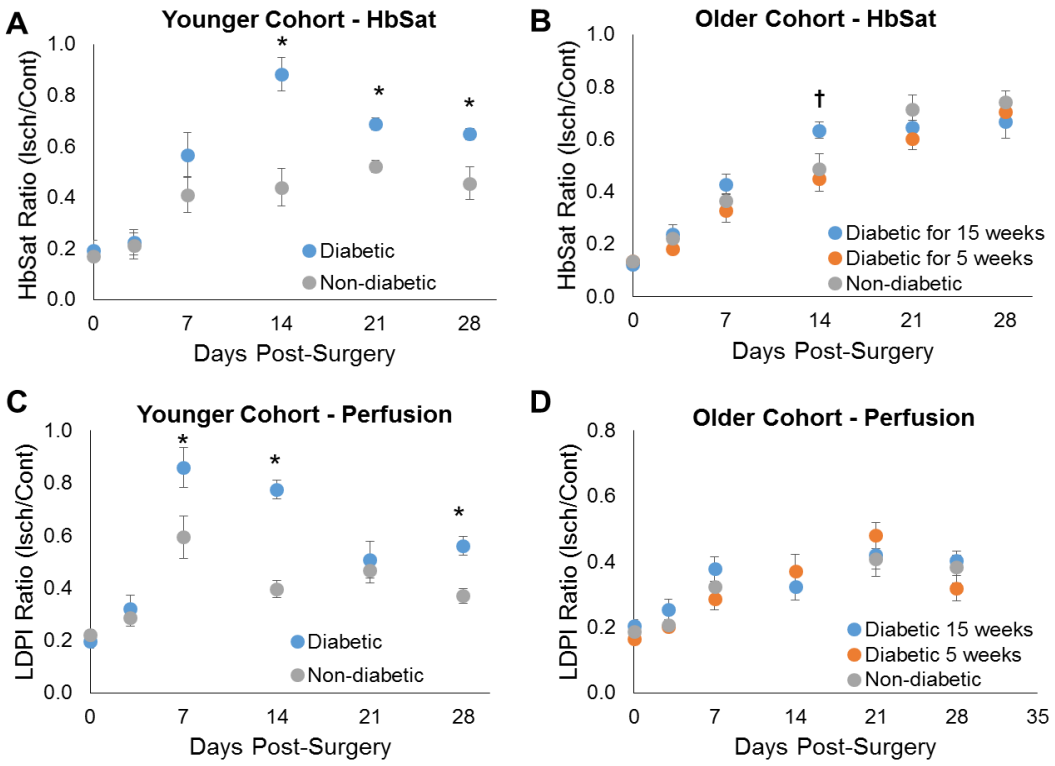

Figure 6.3: Oxygenation and perfusion outcomes of diabetic and non-diabetic mice with hind limb ischemia. Younger diabetic mice exhibit an early "overshoot" response in hemoglobin saturation and perfusion measurements in the footpads that is absent from the response to ischemia in older diabetic mice. A) Younger diabetic mice have a significant increase in HbSat relative to age-matched, non-diabetic mice that peaks at day 14 and is followed by regression. B) In older diabetic mice, there is no overshoot response in the HbSat ratio, and mice with 15 weeks of diabetes only differ significantly at day 14. C) The overshoot response in younger diabetic mice is also apparent in perfusion measurements, with significantly higher ratios at days 7, 14, and 28. D) In the older cohort of mice, there are no significant differences in perfusion ratio between the diabetic and non-diabetic groups. n=5/group for younger cohort and n≥6/group for older cohort. *p<0.05 relative to non-diabetic group at a given time point. †p<0.05 between 15-week diabetic mice and 5-week diabetic mice at day 14.

6.4.3.2 Non-invasive imaging of vascular morphology in diabetes models

The vasculature in the proximal limb (adductor muscle region) was imaged non-invasively in the younger and older cohorts of diabetic and non-diabetic mice using OCT. In the younger cohort, there is a trend toward greater vessel area density and vessel length fraction in the non-diabetic mice at days 7 and 14 post-surgery (p-value for rank sum test at day 7 is at minimum value for n=3/group) (Fig. 6.4A & C). In the older cohort, there are no significant differences in vessel area density or length fraction between the diabetic and non-diabetic mice (Fig. 6.4B & D). Additionally, there is a trend toward increased vessel area density and vessel length fraction in the younger mice in comparison to the older mice. At day 7, vessel area density in the younger, non-diabetic group is greater than that in the older mice with 5 or 15 weeks of diabetes (Kruskal-Wallis ANOVA p=0.05).

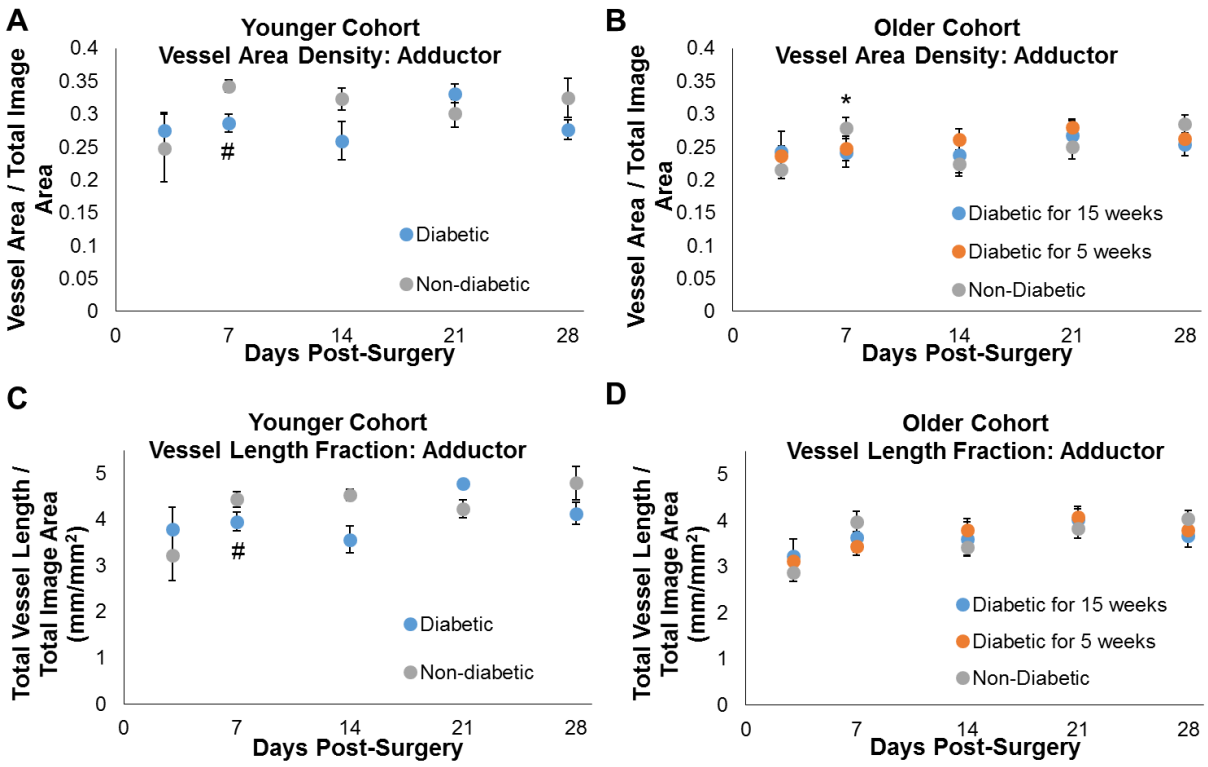

Figure 6.4: Vascular morphology parameters from intravital OCT images reveal differences between diabetes models. In the younger cohort, there is a trend toward increased vessel area density (A) and vessel length fraction (C) in the non-diabetic mice at days 7 and 14 (#p-value at minimum value of 0.10 for n=3/group at day 7). In the older cohort, there are no significant differences between groups in vessel area density (B) or vessel length fraction (D). At day 7, vessel area density in the younger, non-diabetic group (A) is greater than that in the older mice with 5 or 15 weeks of diabetes (B) (*p=0.05). n=3/group for younger cohort and n≥6/group for older cohort.

In addition to the adductor region, the gastrocnemius muscle region was imaged in the older cohort using OCT. The vessel area density in the mice with 15 weeks of diabetes is significantly lower than that of the age-matched non-diabetic mice and the 5 weeks diabetic mice

at days 7 and 28, respectively (Suppl. Fig. B.2A). Similarly, the vessel length fraction in the 15 weeks diabetic group is significantly lower than that in the non-diabetic group and the 5 weeks diabetic group at days 7 and 28, respectively ($p<0.05$) (Suppl. Fig. B.2B).

6.4.3.3 H_2O_2 is elevated in response to ischemia in diabetic mice relative to non-diabetic mice

Tissue H_2O_2 was measured in freshly excised adductor and gastrocnemius muscles in both cohorts of mice using the Amplex Red assay. In the younger cohort, H_2O_2 is elevated in ischemic limbs relative to control limbs in the adductor in both groups and in the gastrocnemius for the diabetic mice at day 8 post-surgery (ischemic / control > 1) (Fig. 6.5A). The relative H_2O_2 level (ischemic/control ratio) is significantly greater in the gastrocnemius muscle of diabetic mice compared to that of the non-diabetic mice ($p<0.05$). In the older cohort, H_2O_2 is elevated in both ischemic adductor and gastrocnemius muscles relative to control limbs in both diabetic and non-diabetic mice at day 14 post-surgery (Fig. 6.5B). The relative H_2O_2 level is significantly greater in the gastrocnemius muscle of diabetic mice than that of non-diabetic mice in the older cohort ($p<0.05$).

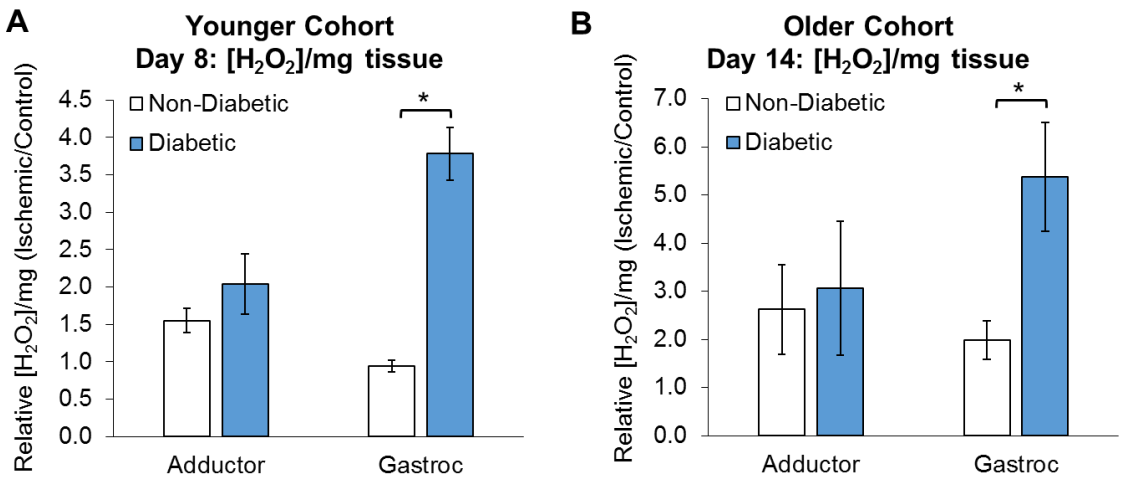

Figure 6.5: Tissue H_2O_2 levels were measured in freshly excised gastrocnemius and adductor muscles in diabetic and age-matched non-diabetic mice. A) In the younger cohort, diabetic mice had significantly greater H_2O_2 in the gastrocnemius muscle compared to the non-diabetic group at day 8 post-surgery. B) In the older cohort, the mice with 15 weeks of diabetes had a greater increase in relative H_2O_2 levels in the gastrocnemius muscle compared to non-diabetic mice at day 14 post-surgery. Additionally, H_2O_2 is elevated in the ischemic limb relative to the control limb (ischemic/control ratio > 1) in both muscles in both the non-diabetic and diabetic mice in the older cohort. n≥4/group for both cohorts. *p<0.05.

6.4.4 Response to PPS and tempo-PPS microspheres in long-term hyperglycemic mice

Based on the presence of a larger "therapeutic window" for improving the vascular response at earlier time points in the older cohort of mice, the variation of the diabetes model consisting of 15 weeks of hyperglycemia prior to surgery was selected for subsequent therapeutic studies. Additionally, these diabetic mice demonstrated elevated oxidative stress in the ischemic limb relative to age-matched non-diabetic mice, as measured by the Amplex Red assay for H_2O_2.

6.4.4.1 Functional response to two microsphere doses in vivo

Two doses of blank and tempo-PPS microspheres were tested in the ischemic limb of diabetic mice. Microsphere doses containing 1.2 mg or 4.75 mg of PPS (plus 0.03 mg or 0.15 mg of tempo-benzoate, respectively, in the tempo-PPS cohort) were injected in the ischemic limb at the time of surgery, and hyperspectral imaging and LDPI were performed to assess the functional response over 2 weeks (Fig. 6.6). In both measures of recovery, the higher dose of microspheres tended to impair the vascular response to ischemia. The perfusion ratio for the lower dose, referred to as the therapeutic dose, is significantly greater than that of the high dose of the respective treatment at day 14 ($p<0.05$) (Fig. 6.6A-B). At day 7, there is a trend toward increased perfusion ratio in the tempo-PPS therapeutic dose group compared to the high dose group ($p<0.1$). The HbSat ratio shows a similar trend of an improved response in the therapeutic dose group for both treatments (Fig. 6.6C-D). The HbSat ratio for the therapeutic dose is significantly greater at day 3 for blank PPS and at days 0 and 14 for tempo-PPS ($p<0.05$).

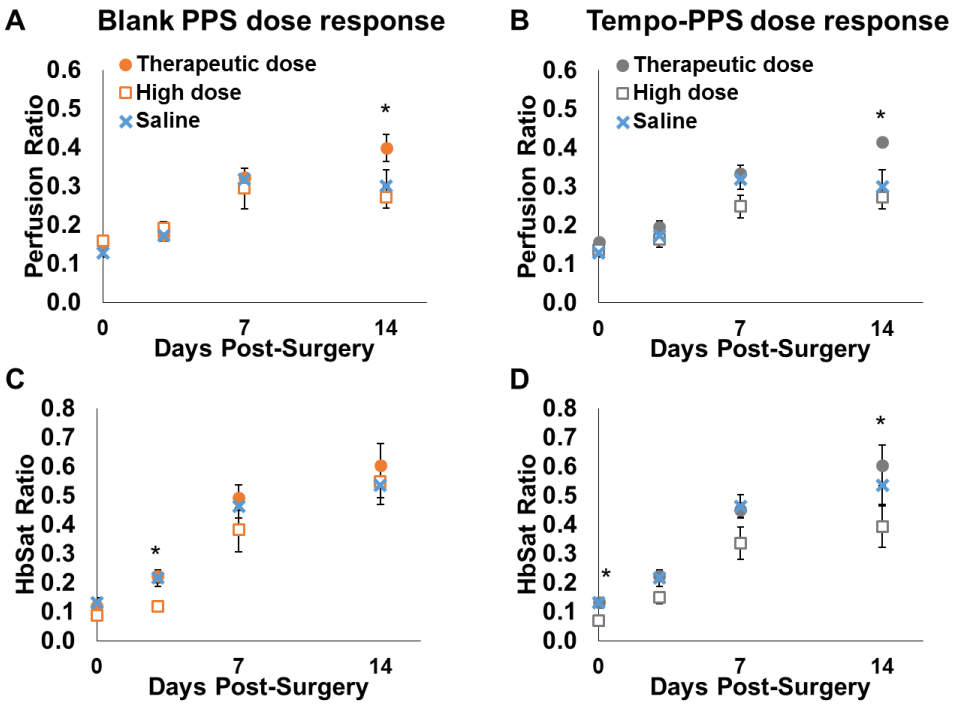

Figure 6.6: Two doses of microspheres were compared using functional measures of recovery. The "therapeutic" dose contains 1.2 mg of PPS (plus 0.03 mg tempo-benzoate in tempo-PPS), and the "high" dose contains 4.75 mg of PPS (plus 0.15 mg tempo-benzoate in tempo-PPS). The perfusion ratio (A-B) for the therapeutic dose of both blank PPS and tempo-PPS is significantly greater than that of the high dose of the respective treatment at day 14 (*p<0.05) (and p<0.1 for tempo-PPS comparison for day 7). The HbSat ratio (C-D) for the therapeutic dose is significantly greater than that of the high dose at day 3 for blank PPS and at days 0 and 14 for tempo-PPS (*p<0.05). (p<0.1 at day 3 for tempo-PPS HbSat). n≥5/group.

6.4.4.2 High-dose microsphere treatment reduces H_2O_2 in ischemic muscle

Tissue H_2O_2 was measured in freshly excised adductor and gastrocnemius muscles at day 14 for mice treated with the high dose of PPS microspheres or tempo-PPS microspheres and

compared to mice receiving a saline injection as a vehicle control (Fig. 6.7A). At the high dose of microspheres, relative H_2O_2 in the gastrocnemius muscle is significantly reduced in comparison to saline-treated control mice ($p<0.05$). At the lower dose of microspheres which resulted in improved functional recovery (Fig. 6.6), no significant differences in relative H_2O_2 between treatment groups at day 8 were detectable using the Amplex Red assay.

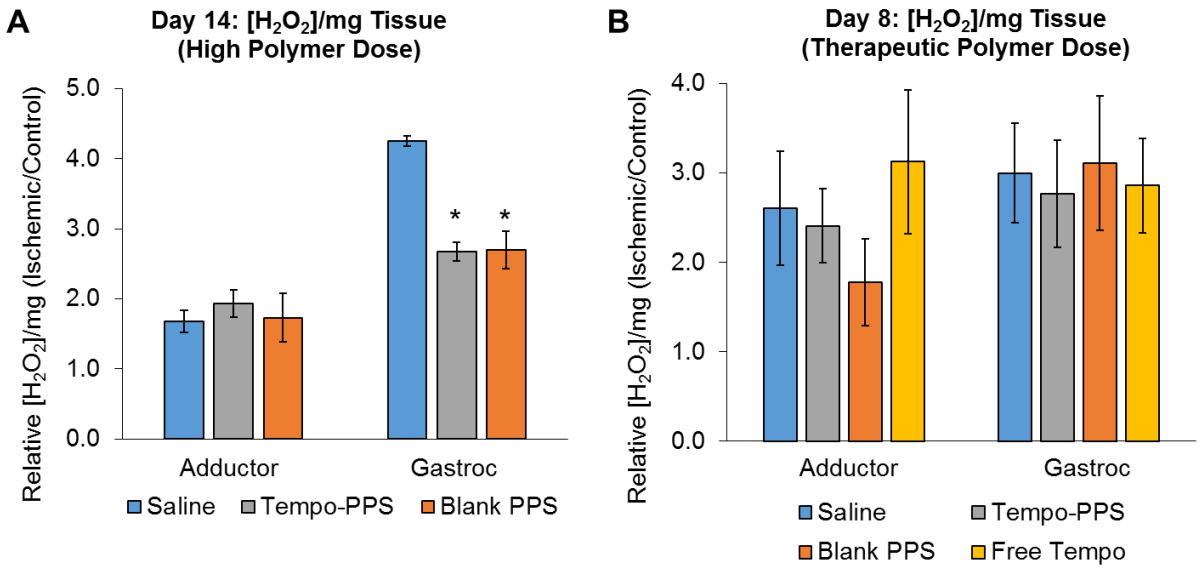

Figure 6.7: The effect of microspheres on H_2O_2 levels in ischemic muscle was measured using the Amplex Red assay. A) The high dose of PPS and tempo-PPS microspheres significantly reduced relative H_2O_2 levels in the gastrocnemius muscle at day 14 relative to saline-treated controls ($p<0.05$ for Kruskal-Wallis ANOVA and * indicates significant differences for post-hoc comparisons). B) At the functionally therapeutic dose of microspheres, no significant differences between treatment groups were detectable with the Amplex Red assay for fresh tissue excised at day 8. n=3-4/group for high dose and n=7-8/group for therapeutic dose.

6.4.4.3 Distal response to microsphere treatment measured with hyperspectral imaging and LDPI

Hemoglobin oxygen saturation was measured in the footpads of diabetic mice treated with saline, blank PPS, tempo-PPS, or free tempo-benzoate at the time of hind limb ischemia surgery (Fig. 6.8A). Microspheres were administered at the therapeutic dose identified in the dose response experiment described previously (Fig. 6.6). A t-test performed on the general linear model of the longitudinal response curves shows that the blank PPS and saline-treated groups differ significantly from days 19 to 28 ($p<0.05$) (Suppl. Fig. B.3). The perfusion ratio was also measured to assess the effect of microsphere treatments on the response to ischemia (Fig. 6.8B). At day 14, the perfusion ratio for the tempo-PPS group is significantly greater than that for the saline and free tempo-benzoate groups, and the blank PPS group perfusion ratio is significantly greater than that of the free tempo-benzoate group as determined by a Kruskal-Wallis ANOVA ($*p<0.05$) and a post-hoc multiple comparisons test. Similarly, a t-test performed on the longitudinal response curves generated by a general linear model analysis returns significantly higher perfusion ratios for the microsphere-treated groups compared to the saline and free tempo-benzoate groups for the latter half of the time course (Suppl. Fig. B.4).

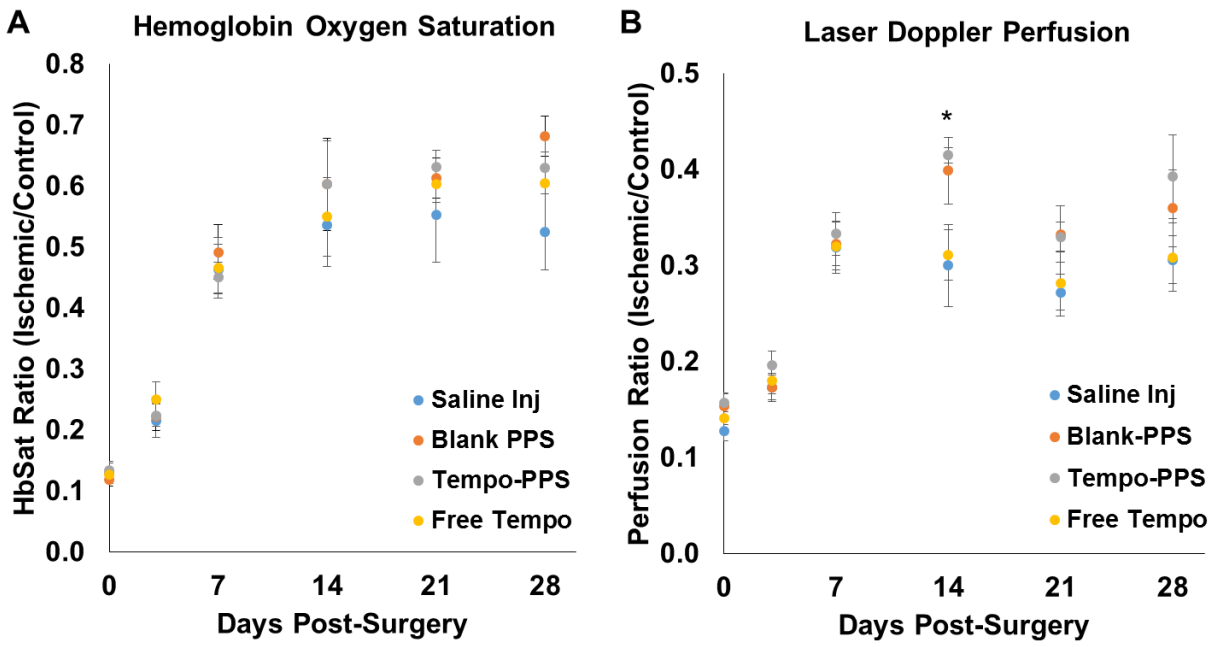

Figure 6.8: HbSat and perfusion were measured in the footpads of diabetic mice treated with saline, blank PPS, tempo-PPS, or free tempo-benzoate. A) Individual time point analyses did not identify significant differences between treatment groups in the HbSat response. B) At day 14, perfusion in the tempo-PPS group is significantly greater than that in the free tempo-benzoate group as determined by a Kruskal-Wallis ANOVA (*p<0.05) with a post-hoc multiple comparisons test. n=15-20/group for days 0-7 and n=6-7/group for days 14-28.

6.4.4.4 Non-invasive imaging of vascular morphology changes in response to therapy

Speckle variance OCT [128, 166] was used to image the longitudinal vascular response to microsphere therapies in the adductor and gastrocnemius muscle regions. Representative time course images from one animal in each treatment group are given for the adductor and gastrocnemius regions in Fig. 6.9 and Fig. 6.10, respectively, and images for additional animals from each group are provided for day 7 in Suppl. Fig. B.5 and Suppl. Fig. B.6. Qualitatively,

vascular morphology in the adductor looks similar among the treatment groups at the start and end of the time course (Fig. 6.9), with an apparent increase in vessel density in the microsphere-treated groups relative to the saline and free tempo-benzoate groups at intermediate time points such as day 7 (Suppl. Fig. B.5). In the gastrocnemius muscle, there is also greater variability in vessel density at early and intermediate time points compared to the end of the time course (Fig. 6.10). Additionally, while the response in the saline group still lags in the gastrocnemius muscle, the response in the free tempo-benzoate group is improved (Suppl. Fig. B.6).

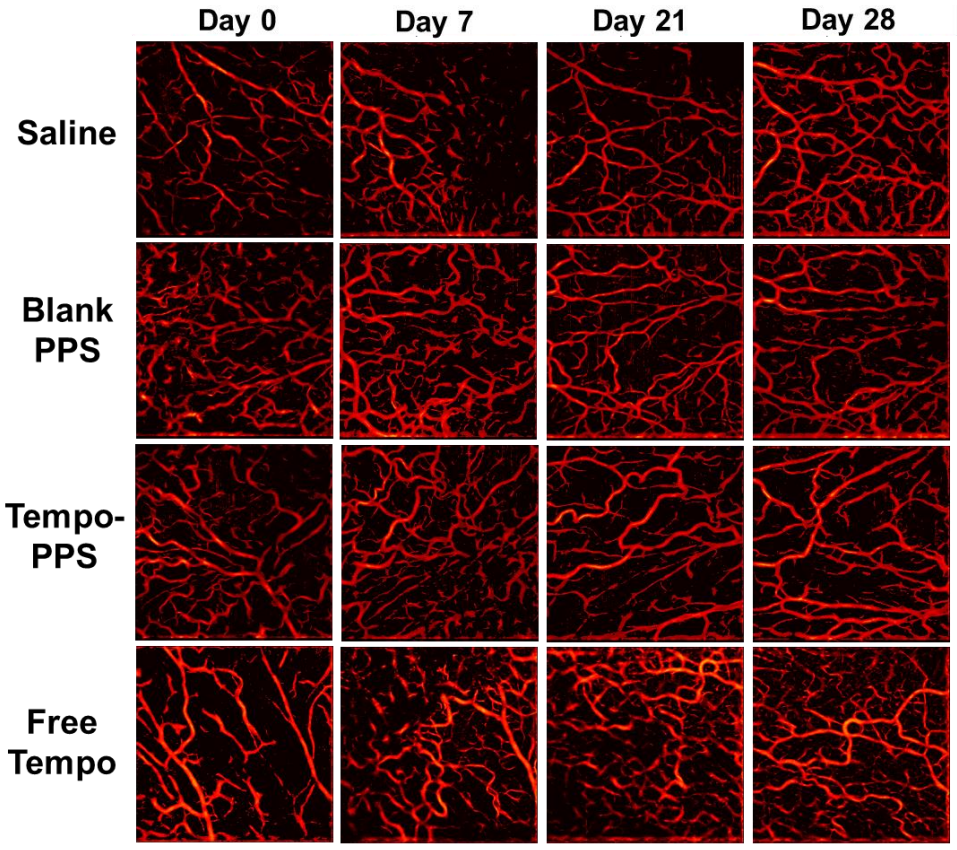

Figure 6.9: Representative time course images of vascular morphology in the adductor muscle region for each treatment group. Images are projections of all vessels present in the volume acquired over a 4 mm x 4 mm area.

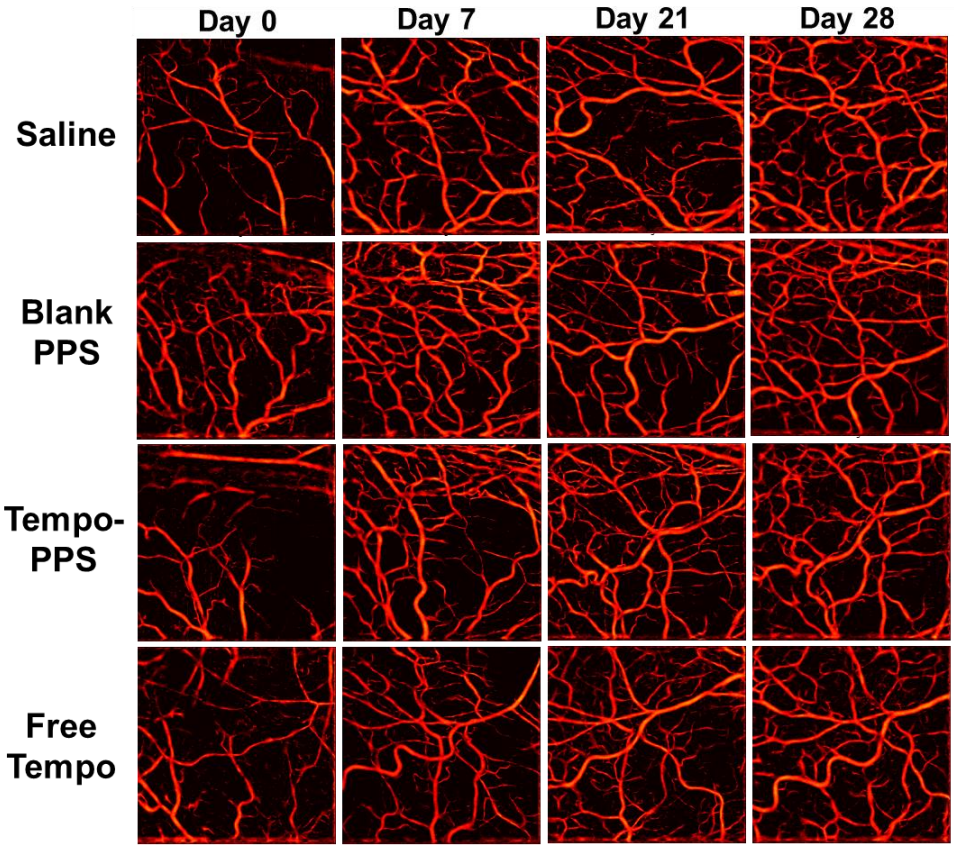

Figure 6.10: Representative time course images of vascular morphology in the gastrocnemius muscle region for each treatment group. Images are projections of all vessels present in the volume acquired over a 4 mm x 4 mm area.

In the adductor muscle, vessel area density is significantly greater in microsphere-treated groups at day 7 ($p<0.001$) and day 14 ($p<0.05$) relative to the saline and free tempo-benzoate groups (Fig. 6.11A), and vessel length fraction is significantly greater at day 7 ($p<0.01$) (Fig. 6.11B). GLM analysis of the longitudinal response in the adductor also reveals significant increases in vessel area density and vessel length fraction in the microsphere groups relative to the saline and free tempo-benzoate groups for the second and third weeks post-surgery (Suppl. Fig. B.7-B.8).

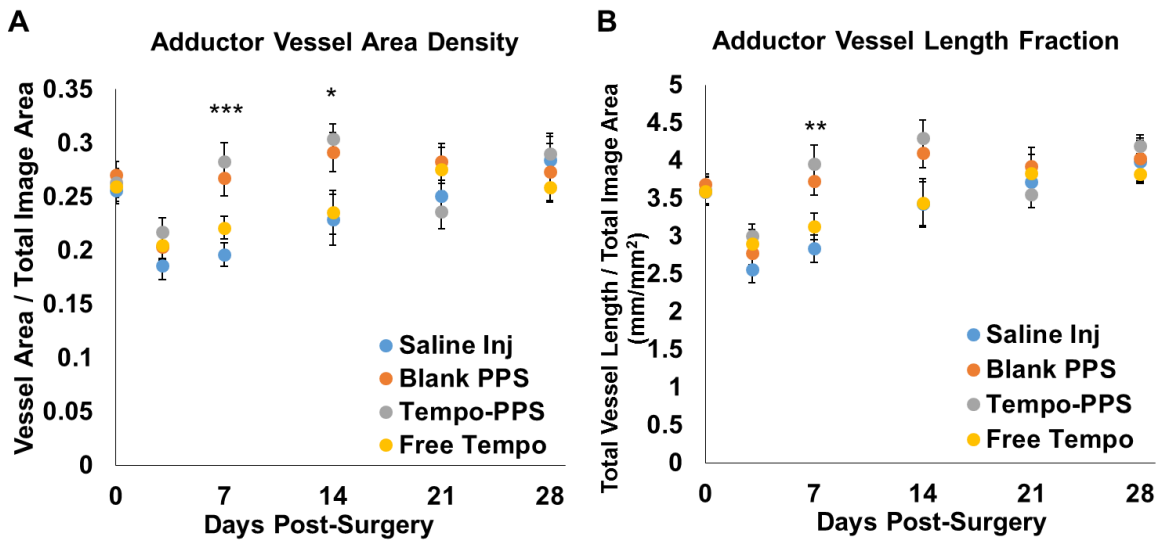

Figure 6.11: Vessel morphology parameters were quantified from OCT images of the adductor muscle region. At day 7, vessel area density (A) is significantly lower in the saline group than in both blank PPS and tempo-PPS groups (Kruskal-Wallis ANOVA ***p<0.001). At day 14, vessel area density in the tempo-PPS group is significantly greater than that in the saline and free tempo-benzoate groups (Kruskal-Wallis ANOVA *p<0.05). Vessel length fraction (B) differs significantly at day 7 between saline and both microsphere groups, and between the free tempo-benzoate and tempo-PPS groups (Kruskal-Wallis ANOVA **p<0.01). At day 14 a trend toward increased vessel length fraction in microsphere groups persists (p<0.1). n=15-20/group for days 0-7 and n=6-7/group for days 14-28.

In the gastrocnemius muscle, vessel area density is significantly lower in the saline and free tempo-treated groups at day 0 relative to the blank PPS group ($p<0.05$) (Fig. 6.12A). At day 3, saline-treated mice have significantly lower vessel area density than the blank PPS and free tempo-benzoate groups ($p<0.01$). Similarly, vessel length fraction in the gastrocnemius muscle is significantly lower in the saline group than that in the blank PPS and free tempo-benzoate-treated

groups at day 3 ($p<0.05$). At day 7, saline-treated mice have significantly lower vessel length fraction than the blank PPS and tempo-PPS treated groups ($p<0.05$). GLM analysis of the longitudinal response in the gastrocnemius also indicates that there are significant differences between treatment groups over similar ranges in time (Suppl. Fig. B.9-B.10).

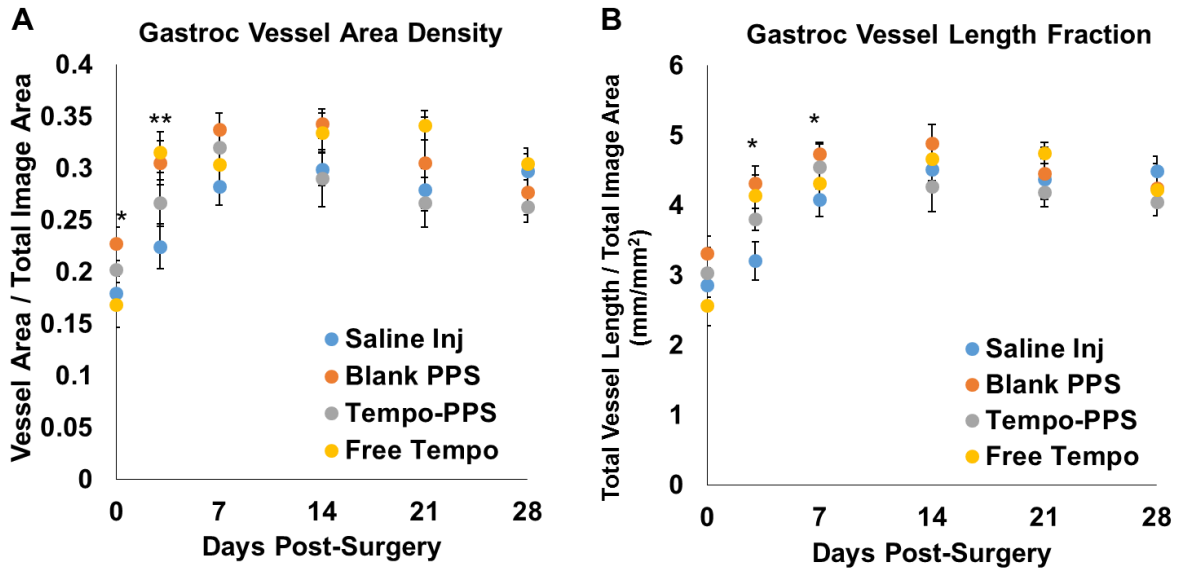

Figure 6.12: Vessel morphology parameters were quantified from OCT images of the gastrocnemius region. At day 0, the blank PPS group has significantly greater vessel area density (A) than the saline and free tempo-benzoate groups (Kruskal-Wallis ANOVA *$p<0.05$). At day 3, vessel area density in the saline group is significantly lower than that in the blank PPS and free tempo-benzoate groups (Kruskal-Wallis ANOVA *$p<0.01$). Vessel length fraction (B) is significantly lower in the saline group than in the blank PPS and free tempo-benzoate groups at day 3 (Kruskal-Wallis ANOVA *$p<0.05$). At day 7, saline-treated mice have significantly lower vessel length fraction than the blank PPS and tempo-PPS groups (Kruskal-Wallis ANOVA *$p<0.05$). n=15-20/group for days 0-7 and n=6-7/group for days 14-28.

6.4.4.5 IHC for assessing inflammation and oxidative stress in the ischemic muscle

CD68 IHC on sections from gastrocnemius muscles excised at day 8 post-surgery (Fig. 6.13, top) show that macrophage infiltration is present in ischemic tissue in all treatment groups. Nitrotyrosine IHC was performed in serial sections in order to assess peroxynitrite-mediated oxidative stress in the ischemic gastrocnemius (Fig. 6.13, bottom). In a non-ischemic control muscle, CD68 staining is sparse and nitrotyrosine staining is absent. In ischemic muscles, nitrotyrosine staining is present in varying intensities and does not appear to correlate with the extent of CD68 staining. These observations suggest that both inflammation and oxidative stress are present in ischemic muscles across treatment groups, but a larger sampling volume of tissue is needed to provide quantification of oxidative stress for discerning treatment effects.

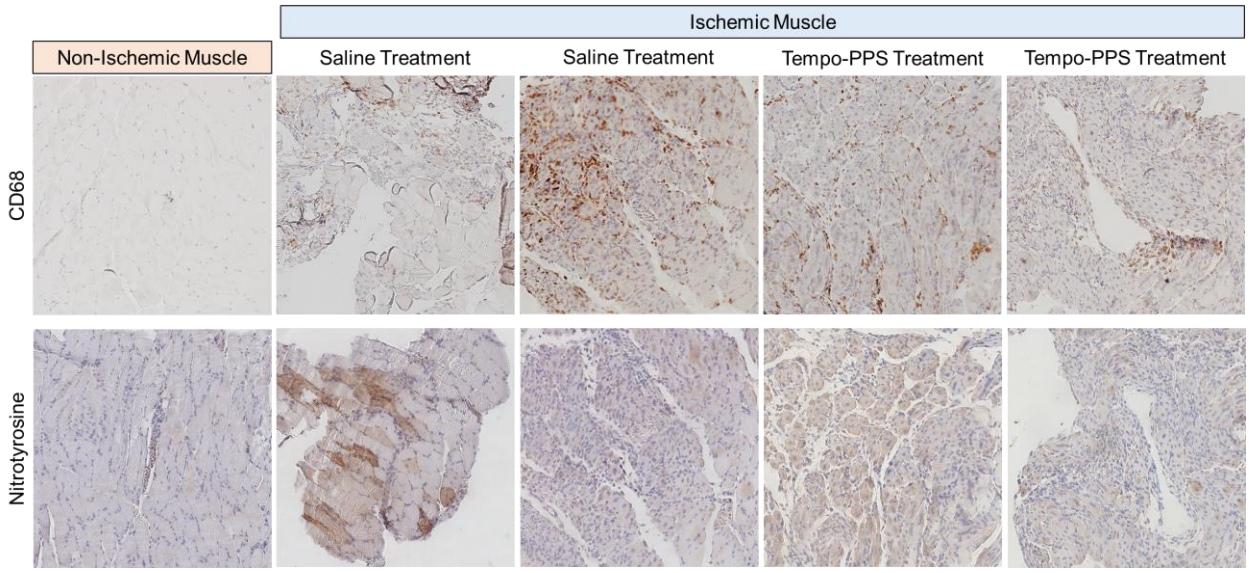

Figure 6.13: CD68 and nitrotyrosine IHC were performed on gastrocnemius muscles (5 µm sections) extracted at day 8 post-surgery. Staining for macrophages and nitrotyrosine (oxidative stress-induced damage) is present in ischemic muscles in all treatment groups, and the extent of inflammation and damage is variable within treatment groups.

6.5. Discussion

Transient or low levels of ROS are important to signaling pathways that promote regeneration and growth, while chronic or high levels of ROS, which often occurs in diabetes, can be detrimental to vascular function [43, 183, 204]. The inhibition of ROS in healthy animals has shown that ROS are key players in angiogenesis during normal recovery [43, 171, 205]. This effect is believed to be mediated by the mechanistic functions of H_2O_2 in stimulating cell migration and proliferation in endothelial cells [171, 205], and of ROS generated by NADPH oxidases which modulate VEGF-A expression and vascular smooth muscle cell proliferation [43]. In fact, infusion of the H_2O_2 and peroxynitrite scavenger ebselen reduces perfusion recovery and capillary density [171], and mice lacking the $gp91^{phox}$ (Nox2) subunit of NADPH oxidase have impaired neovascularization [43, 171, 183]. However, studies using preclinical models of chronic oxidative stress (i.e. diabetic animals) have demonstrated the potential for antioxidant treatment to improve neovascularization and vascular function in these situations [43, 44, 191, 206, 207]. Diabetes is a known risk factor for atherosclerosis and is associated with increased prevalence of PAD [208], so the development of more effective treatments for mitigating vascular dysfunction is of significant interest. Scavenging ROS with superoxide dismutase and/or catalase mimetics is a promising approach, but to date these treatments have generally been administered systemically in preclinical models [44, 191, 209]. In order to avoid off-target effects in tissues with physiologically appropriate levels of ROS [204], we have pursued ROS-sensitive PPS microspheres [91] as a local delivery vehicle for superoxide dismutase mimetic tempo-benzoate.

PPS was selected as the polymer carrier in this application because it provides ROS-responsive drug release, scavenges H_2O_2 (Fig. 6.1B) and peroxynitrite (Fig. 6.2), and protects

cells from H_2O_2-induced toxicity [49, 91]. Additionally, this dual-antioxidant approach allows for PPS to scavenge the H_2O_2 generated by the dismutation of superoxide by encapsulated tempo-benzoate (Fig. 6.1A & 6.1B). This concept of combined ROS targeting has been previously demonstrated *in vitro* in a hybrid polymer-enzyme nanocarrier system [88]. However, micron-sized particles such as the PPS microspheres are advantageous because they are able to form a stable depot at the targeted site and provide sustained drug release over a longer time frame as shown in previous work [91].

Prior to evaluating the effect of the tempo-PPS microspheres on recovery from hind limb ischemia, we optimized our preclinical model through comparisons between younger mice with 5 weeks of pre-surgical STZ-induced hyperglycemia and older mice with 15 or 5 weeks of hyperglycemia prior to surgery. The duration of hyperglycemia prior to experimental manipulation varies among previously reported preclinical studies of the vascular response to ischemia [13, 43, 44, 206, 207]; however, the effects of diabetes on vascular function have been shown to be disease duration-dependent [210-212]. Additionally, susceptibility to STZ and the severity of the resulting hyperglycemia and other symptoms varies with mouse strain [213]. In the current work, we have used the FVB strain which is susceptible to robust, persistent hyperglycemia after a low dose STZ protocol (fasting blood glucose ranging from 300 – 700 mg/dL in the current studies) and has demonstrated improved neovascularization with antioxidant and anti-inflammatory therapies [206, 207]. After induction of hind limb ischemia in the younger and older cohorts of diabetic mice and age-matched non-diabetic controls, an "overshoot" response was observed in footpad hemoglobin saturation and perfusion ratios in the younger diabetic group, but not in the younger non-diabetic group or the older groups (Fig. 6.4). This response with an early peak followed by regression in the younger diabetic group is similar

to that observed in diabetic C57Bl6/J mice which had more pronounced vessel growth and vessel rarefaction phases in comparison to non-diabetic controls [13]. In contrast, the older cohort of mice in the current study did not show significant differences in the footpad measures of recovery, except for a transient increase in the HbSat ratio for the 15 weeks-diabetic group at day 14 (Fig. 6.3B). As a measure of the vascular response in the proximal limb, vessel morphology parameters were extracted from OCT speckle variance images. There was a trend toward increased vessel density and total length in the adductor muscle region of younger non-diabetic mice, and the older cohort exhibited less vascular remodeling overall in comparison to the younger cohort (Fig. 6.4). Although there were no significant differences between the older groups in vessel morphology in the adductor, vessel area density and length fraction in the gastrocnemius muscle were significantly lower in the mice with 15 weeks of diabetes compared to the other age-matched groups (Suppl. Fig. B.2). Additionally, relative H_2O_2 levels were significantly increased in the gastrocnemius of 15 weeks-diabetic mice in the older cohort (Fig. 6.5B). Taken together, these comparisons indicate that the mice in the older cohort with 15 weeks of diabetes prior to surgery have the greatest "therapeutic window" for reducing oxidative stress in the muscle and improving the vascular response at early time points. Therefore, this model was selected to evaluate the effect of the tempo-PPS microspheres on the response to hind limb ischemia.

The functional effects of PPS and tempo-PPS microspheres were evaluated in the hind limb ischemia model using perfusion, hemoglobin oxygen saturation, vessel morphology, and oxidative stress as endpoints. A preliminary dose experiment was performed to identify an appropriate level of ROS-scavenging, since there is an optimal range in which ROS are beneficial to angiogenesis [43], and scavenging "too much" could be detrimental [171, 183] even

in the diabetic model. The comparison of two doses showed that a higher dose of microspheres reduced the perfusion and HbSat ratios significantly (Fig. 6.6), which is likely due to scavenging H_2O_2 to a greater extent (Fig. 6.7A) in comparison to a low dose of microspheres. In contrast, the lower dose of microspheres (referred to as the therapeutic dose) did not result in a decrease in H_2O_2 relative to control groups detectable by the Amplex Red assay (Fig. 6.7B). However, in subsequent experiments with the therapeutic dose, there were significant increases in perfusion in the footpads (Fig. 6.8 and Suppl. Fig. B.4) and vessel remodeling in the adductor (Fig. 6.11 and Suppl. Fig. B.7-8) associated with the microsphere treatments relative to saline and free tempo-benzoate controls. Hemoglobin saturation ratios showed a slight improvement with microsphere treatments at the end of the time course with the modeled data (Suppl. Fig. B.3). IHC showed that macrophage infiltration and peroxynitrite-mediated oxidative stress (measured via nitrotyrosine) were present in both saline- and tempo-PPS-treated mice, and the staining was heterogeneous both within tissue sections and within treatment groups (Fig. 6.13). This heterogeneity warrants further studies with bulk tissue measurements such as a Western blot for nitrotyrosine. Another notable result in these studies is that mice treated with blank PPS microspheres were statistically equivalent to mice treated with tempo-PPS microspheres in the functional endpoints, suggesting that scavenging of H_2O_2 and peroxynitrite by PPS is a driving factor in this enhanced response. However, it is warranted to further explore more doses of tempo-benzoate in order to more thoroughly discern whether tempo-benzoate will provide an additive effect in a more optimized formulation. Overall, these microspheres show promise for targeting local oxidative stress and improving the vascular response to ischemia in mice with prolonged hyperglycemia. Future studies could investigate optimization of the relative doses of the PPS and tempo-benzoate components of the dual ROS-scavenging system.

6.6. Conclusions

There is a significant need for improved therapies for diabetic PAD, as two decades of clinical trials have yielded inconsistent outcomes and no new Food and Drug Administration-approved therapies for PAD [214]. In this work, oxidation-sensitive PPS was used to encapsulate a superoxide-scavenging nitroxide radical, tempo-benzoate, in microspheres for local delivery of dual-antioxidant therapy. The microspheres provide environmentally-responsive drug release and are capable of scavenging multiple ROS including H_2O_2, superoxide, and peroxynitrite. A mouse model of diabetic PAD with significant oxidative stress and an impaired response to ischemia was identified, and blank PPS and tempo-PPS microspheres were evaluated *in vivo*. The microspheres were found to reduce ROS levels in muscle tissue when administered at a high dose, while a lower dose was more effective in improving functional measures of vascular recovery in the ischemic hind limb. Interestingly, the blank PPS microspheres provided an equivalent effect to that of the tempo-PPS microspheres *in vivo*, suggesting that targeting H_2O_2 and peroxynitrite in the model is an effective strategy. The results from the current work and prior studies have established the PPS microsphere system as a promising drug delivery vehicle for treatment of diabetic PAD or other pathologies associated with localized oxidative stress.

6.7. Acknowledgments

The authors thank Fang Yu, Alonda Pollins, John Martin, Melissa Markham, and Dan Gil for assistance with experiments, Mukesh Gupta for the PPS polymer, Jeffrey M. Davidson for use of the LDPI, and Christine O'Brien for guidance on GLM analysis. Immunohistochemistry was performed in the lab of Lillian B. Nanney and in the Vanderbilt Translational Pathology Shared Resource (supported by NCI/NIH Cancer Center Support Grant 2P30 CA068485-14 and the Vanderbilt Mouse Metabolic Phenotyping Center Grant 5U24DK059637-13). This work was

supported by a Vanderbilt Discovery Grant, NIH R21 HL109748, and American Heart Associate Grant-in-Aid 12GRNT 12060235. K.M.P. was supported by a P.E.O. Scholar Award and an NSF Graduate Research Fellowship DGE-0909667.

CHAPTER 7

SYNOPSIS AND FUTURE DIRECTIONS

7.1 Summary

Despite extensive, promising preclinical studies and two decades of clinical trials of angiogenic and cell therapies, there is yet to be a new therapy approved by the Food and Drug Administration for PAD patients [214]. Based on what has been learned from these clinical trials, several recommendations have been made for advancing research in this field, including the incorporation of cardiovascular risk factors such as diabetes into preclinical models to increase their predictive value, and the application of novel imaging technologies to understand mechanisms of response and to indicate the likelihood of success [214]. Additionally, key readouts in the widely used hind limb ischemia model of PAD have typically been focused on tools with limiting factors: LDPI is low-resolution and subject to many variables including temperature and depth of anesthesia, micro-computed tomography is high resolution but post-mortem and sensitive to under-filling with the contrast agent, and histology is also post-mortem and is subject to sampling error [215]. The goal of this work was to develop a non-invasive, optical imaging platform to study the vascular response to ischemia in the mouse hind limb ischemia model with previously unattainable, quantitative measures of vascular function obtained over time from a living animal. Additionally, these studies set out to apply this platform to study the effect of diabetes on hind limb ischemia recovery using these novel endpoints, and evaluate novel therapeutic treatments that target an important factor contributing to vascular dysfunction in diabetes: oxidative stress.

In Aim 1, the hyperspectral imaging and OCT platform was developed for application to the hind limb ischemia model, including validation of hemoglobin saturation and blood flow

measurements, respectively. First, young, wild-type mice with hind limb ischemia were used to establish imaging protocols and image processing methods. Additionally, two strains with known differences in the response to ischemia were used to further validate the observed changes in vessel morphology data provided by speckle variance OCT. Importantly, this work was the first to demonstrate longitudinal, non-invasive imaging of the vascular response to hind limb ischemia using OCT and hyperspectral imaging, and it resulted in the extraction of quantitative measurements that correlated with a gold standard method (LDPI).

In Aim 2, the effect of diabetes on the response to ischemia was investigated using mice with STZ-induced hyperglycemia. Young adult mice with 5 weeks of diabetes and older mice with either 5 or 15 weeks of diabetes prior to surgery were compared, along with age-matched, non-diabetic mice. Interestingly, an overshoot response was observed in the younger diabetic mice, but not in the older diabetic mice. Additionally, OCT revealed an overall trend of reduced vessel remodeling in the older mice compared to the younger mice, especially in the group with 15 weeks of hyperglycemia. Previous studies have used the hind limb ischemia model with a variable range of durations of diabetes (2 weeks to 12 weeks) to investigate the impact of hyperglycemia on vascular response, which has led to contradicting observations in the literature [210]. However, this work, in addition to the work of others [210-212], highlights the dependence of vascular dysfunction on the duration of the disease, in addition to other factors such as the strain of mice used [93] and the extent of femoral artery excision in the surgical procedure.

Finally, Aim 3 applied the optical imaging platform to evaluate novel antioxidant therapies *in vivo* in a model of diabetic PAD. Initially, the antioxidant and anti-inflammatory molecule curcumin was delivered from the ROS-responsive, PPS microsphere system that we

have developed and characterized. This work demonstrated the ability to provide on demand drug release from a local depot in the ischemic tissue, which is important when systemic off-target effects are undesirable. Additionally, curcumin-PPS microspheres had a significant therapeutic effect in functional measures of vascular recovery in the ischemic limb. In a second therapeutic study, the same PPS microsphere system was used to deliver tempo-benzoate, a superoxide scavenger, for dual targeting of H_2O_2 and superoxide in a mouse model with a more impaired vascular response and significant oxidative stress identified in Aim 2. Both tempo-PPS and blank PPS-treated mice showed significant increases in measures of recovery including vascular remodeling (OCT), perfusion (LDPI), and hemoglobin saturation (hyperspectral imaging) in comparison to saline and free tempo-benzoate treatments. This demonstrated that in this model of diabetic PAD, scavenging H_2O_2 and peroxynitrite with PPS is a viable strategy for mitigating the effect of oxidative stress on recovery from ischemia. An additive effect from tempo-benzoate was not detected in this study, but future work will address the limitations of the current microsphere formulation so that the relative dose of tempo-benzoate compared to the PPS dose can be varied for optimization of the dual-antioxidant approach.

Together, these studies show that the combination of OCT and hyperspectral imaging can be applied to address a gap in current methodologies for studying neovascularization in the hind limb ischemia model: the ability to obtain high-resolution, quantitative vascular structure and function data from individual animals over time. Additionally, this imaging approach has been applied to study a more relevant preclinical model of PAD and evaluate novel antioxidant therapies that can be applied to treat diabetic PAD and other diseases with localized, chronic oxidative stress and inflammation.

7.2 Limitations

The OCT and hyperspectral imaging platform has been successfully applied to study temporal and therapeutically-induced changes in the mouse hind limb vasculature, and provides an important advance in preclinical methodologies for studying arteriogenesis and developing novel therapies. However, it should be noted that the OCT method is not directly translatable to serve the same purpose in clinical trials for proangiogenic therapies. First, although it has the advantages of collecting three-dimensional data with micron-resolution without exogenous contrast agents, OCT typically has an imaging depth of only 1-3 mm in tissue and fields of view consisting of several millimeters [29, 30, 79], which would not be sufficient for imaging the peripheral vasculature non-invasively in humans. OCT is already used for intravascular imaging in humans [216], but that method would not provide morphological information analogous to what has been acquired in the mouse model. However, other imaging techniques such as MRI, CT angiography, and duplex ultrasound may be used to detect changes in perfusion and arteriogenesis in humans with adequate resolution [217, 218]. Additionally, hyperspectral imaging is being investigated as a tool for assessing oxygenation status in the skin of PAD and diabetes patients [219, 220], and the results of our preclinical studies have validated the sensitivity of this technique for detecting changes in oxygenation in response to ischemia and therapy.

A second concern regarding this work is related to future clinical translation of ROS-scavenging, polymeric microparticles. First, it may be a challenge to determine the optimal dose of these particles since low levels of H_2O_2 and superoxide are necessary for normal physiological processes. “Over-scavenging” of ROS could be detrimental rather than therapeutic, as shown in our studies in Chapter 6 and in the work of others [43, 171]. Although the particles were tested

for cytocompatibility *in vitro* (Fig. 5.3) and there was no apparent, deleterious host response to the microsphere treatments *in vivo* (Appendix Fig. A.4), more dose-response studies should be performed *in vivo* to determine the dose limits for avoiding toxicity and for optimizing ROS levels. Additionally, we were not able to detect a significant additive benefit of delivering tempo-benzoate along with the PPS, which is likely a result of the low concentration of tempo-benzoate relative to that of the PPS. In section 7.3, a brief discussion on possible future work to improve on the current approach for delivering tempo-benzoate with PPS is provided. Finally, clinical trials with other antioxidant therapies such as vitamins E and C have produced disappointing, ambiguous results in terms of improving cardiovascular outcomes [56, 187, 189], and clinical trials with a native SOD enzyme (bovine CuZnSOD) were discontinued due to immunogenic responses, despite promising results [221]. However, we and others are optimistic that low-molecular-weight superoxide dismutase mimetics may overcome some limitations associated with these prior antioxidant approaches by acting catalytically rather than in a stoichiometric manner, and by avoiding immunological problems [56, 221]. Additionally, the use of micron-sized particles for ROS-responsive drug delivery has the added benefits of longer-term retention at the desired site (Fig. 5.5A), and "smart" drug release only when there is local demand (oxidative stress) (Fig. 5.2).

7.3 Future Directions and Recommendations

Based on the limitations and challenges described in section 7.2, there are several avenues for future research that may be pursued, including (1) improved control over the tempo:PPS ratio in the microspheres to optimize the potential benefit of co-delivery, (2) application of the PPS microspheres to other preclinical models of oxidative stress and inflammation, and (3) application of the optical imaging methods developed here to other

preclinical models and expansion of OCT vessel morphology analysis to 3-D volumes. As shown in Chapter 6, an additive effect from delivery of tempo-benzoate in the PPS microspheres was not detected relative to delivery of blank PPS microspheres. This may be due to the low drug content that is achievable using the current microsphere fabrication method of oil-in-water emulsion with PPS and free tempo-benzoate. Others have incorporated a nitroxide radical (tempo) moiety into triblock polymers to form hydrogel-forming micelles with superoxide-scavenging activity [193] and into copolymers for superoxide-scavenging, pH-responsive nanoparticles [199]. A "tempo polymer" approach may provide an opportunity to tune the relative amounts of the superoxide scavenging radical and PPS in the microspheres by varying the ratio of tempo polymer to PPS polymer in the oil phase for formation of mixed-polymer microspheres.

As mentioned in Chapter 6, there is potential to scavenge too much H_2O_2 in the hind limb ischemia model, resulting in impaired functional recovery. As ROS have an overall pro-angiogenic role, it is challenging to optimize antioxidant therapies in a model in which neovascularization is the goal, even in the case of hyperglycemia-induced oxidative stress. Therefore, it would be interesting to apply this antioxidant therapy to other models of oxidative stress in which reducing ROS and inflammation is the primary goal rather than augmenting a vascular response. Potential applications for the PPS microspheres include osteoarthritis [222] and acute lung inflammation (acute respiratory distress syndrome) [223, 224].

The optical imaging methods that were developed for the hind limb ischemia model in this work can also be applied to other preclinical studies of vascular remodeling, including studies on the vascular response to therapies. Wound healing improvement with hydrogels and biomaterial scaffolds is an area of interest in our laboratory, and the ability to image

neovascularization within the materials non-invasively over time would be advantageous over sacrificing animals at multiple time points for histological analysis. Other areas of interest include imaging the microvascular response in preclinical models of sub-arachnoid hemorrhage and migraines. Finally, a next step in the OCT vascular imaging work could be the extension of the morphological analysis to three dimensions from the current 2-D analysis performed on projections of speckle variance volumes. This is challenging due to shadowing artifacts [116] and the relatively low contrast to noise ratio of OCT volumes compared to other imaging modalities such as MRI and CT, but recently, progress has been made in optimizing 3-D vessel segmentation algorithms for OCT imaging of the choroidal vasculature [225].

Throughout this dissertation, several variations on the hind limb ischemia model were utilized. These variations included multiple strains of mice (A/J, FVB, Balb/c, and C57Bl/6), different durations of diabetes (5 weeks, 15 weeks), different ages (~9, 15, and 25 weeks old), and different surgical models (varied length of excised femoral artery and vein segments). The dependence of the vascular response to ischemia on mouse strain is well established [69, 93], and as shown in Chapters 4 and 6, the choice of mouse model has a significant impact on outcome in hind limb ischemia studies. In Chapter 3, a small segment of the femoral artery and vein was ligated and excised in healthy, young adult A/J mice (Fig. 7.1A). Some toe and foot necrosis was observed in this strain, but the majority of the animals recovered distal perfusion and hemoglobin saturation within three weeks. In unpublished observations, the “mild” surgery model in young adult C57Bl/6 mice only reduced ischemic footpad hemoglobin saturation and perfusion to ~50% of the control footpad, and the mice recovered quickly. In Chapter 4, healthy, young adult Balb/c and FVB mice were compared using a more severe ligation and transection procedure (Fig. 7.1B). While Balb/c mice displayed severe ischemia and necrosis of the foot for all animals, very

few FVB mice developed necrosis in the foot beyond the toes. However, FVB mice still exhibited a pronounced reduction in footpad perfusion and hemoglobin saturation following induction of ischemia (ischemic:control ratio of ~20%) (Fig. 6.3). With respect to age and diabetes comparisons, 15-week-old FVB mice with 5 weeks of hyperglycemia prior to surgery had an "overshoot" response in the distal perfusion and hemoglobin saturation measures (Fig. 6.3), even with the more severe vessel transection procedure (Fig. 7.1B). In contrast, 25-week-old mice with or without hyperglycemia had a dampened vascular response distally (Fig. 6.3), and 15 weeks of diabetes had the greatest effect on vessel remodeling in the proximal limb (Fig. 6.4 and B.2). Diabetes increased oxidative stress in both the younger and older diabetic mice (Fig. 6.5), but in terms of providing a "window" to improve the vascular response with a therapeutic intervention, the long-term hyperglycemia (15 weeks) model is recommended.

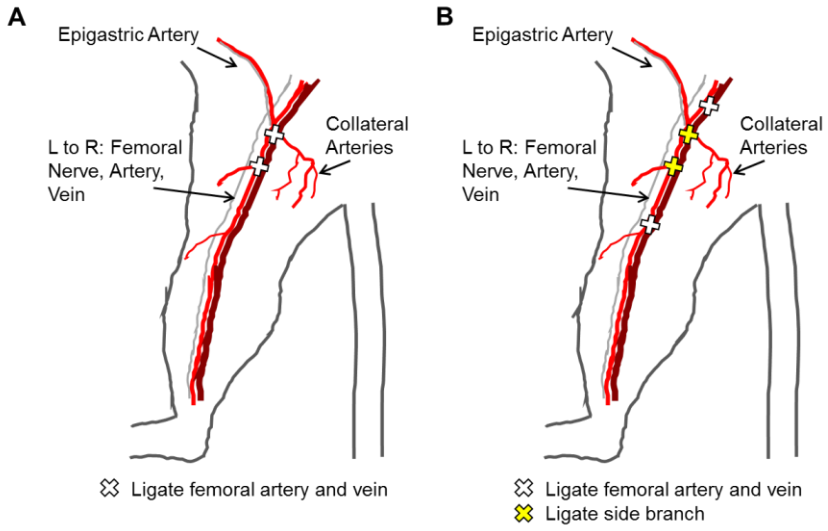

Figure 7.1: "Mild" (A) and "Severe" (B) vessel ligation and transection locations for the mouse hind limb ischemia model used in Chapter 3 (mild) and in Chapters 4-6 (severe). In both models, a white "X" indicates the start or end point of the excised segment of the femoral artery and vein.

7.4 Contribution to the Field and Broader Impacts

Contribution to Biophotonics

This work represents the first application of combined hyperspectral imaging and optical coherence tomography for quantitative, non-invasive, longitudinal imaging of the vascular response to hind limb ischemia. To our knowledge, we are the first to image vessel morphology in the ischemic hind limb longitudinally without making incisions in the skin or injecting exogenous contrast agents. Previously, these imaging technologies were predominantly applied to applications in cancer, superficial wounds, and eye imaging. By developing image acquisition, processing, and quantification methods for the hind limb ischemia model, this dissertation has extended the reach of biophotonics and optical imaging to a new audience within basic science and drug development research. Additionally, the image processing and quantification methods described in Chapters 3 and 4 of this work can be applied to future studies in other preclinical models in which monitoring vascular dynamics is important.

Contribution to Vascular Biology

The optical imaging platform developed in this work provides a new toolset for basic science research on postnatal neovascularization. With the prior set of standard methodologies for hind limb ischemia studies, a comprehensive assessment of arteriogenesis and angiogenesis in this model requires the use of multiple modalities and post-mortem evaluations that make longitudinal studies expensive and time-consuming. Furthermore, post-mortem animal evaluation can be affected by artifacts associated with injection of viscous contrast agents at super-physiologic pressures or masking of desired epitopes by fixation. The ability to obtain both structure and function information intravitally at every time point within individual animals is attractive because fewer cohorts of mice are required to complete a statistically powered time

course study. Longitudinal monitoring of individual animals also helps mitigate the effects of inter-animal variability present even within inbred strains, and provides incentive for researchers to conduct longer time courses which would require several more cohorts using the previous toolset alone. These extended time courses are important as recent studies have shown that the vascular response is biphasic and the initial vascular response may not be stable long-term, especially in diabetic animals [13]. Finally, this contribution to the toolset available to vascular biology researchers may enable new insights into the mechanisms of vascular dysfunction in the setting of diabetes with new, intravital structure-function endpoints.

Potential Impact on Preclinical Drug Development for PAD

As discussed previously, recent clinical trials have yielded inconsistent and disappointing outcomes in comparison to promising preclinical results for novel PAD therapies. Contributing factors include the use of young and healthy animals rather than mice with cardiovascular risk factors incorporated for better predictive value, and assessment only in the early stages of hind limb ischemia recovery. However, therapeutic angiogenesis treatments have been shown to induce an unstable vascular response that regresses after cessation of treatment, and this regression phase can be even more pronounced in the setting of diabetes [13]. The ability to image individual cohorts of mice non-invasively for time courses of longer duration would incentivize drug development researchers to utilize more relevant mouse models (i.e. aged or diabetic mice) since the cost associated with sacrificing a cohort of animals at every time point could be reduced. The longitudinal structure-function data acquired with OCT and hyperspectral imaging is complementary to standard post-mortem micro-CT and histological analyses that can still be acquired at the end of an intravital study. Furthermore, the new intravital endpoints derived from the optical imaging data may enable more robust evaluation of new therapeutic

agents and drug delivery vehicles and streamline identification of the most promising candidates for clinical translation.

7.5 Conclusion

With the increasing prevalence of PAD and the significant clinical consequences associated with diabetic PAD, there is a growing need for a better understanding of the arteriogenesis and angiogenesis processes and for more effective alternative therapies. There is currently a disconnect between preclinical and clinical outcomes for novel therapeutic treatments for PAD, and intravital imaging of vascular structure and function has the potential to improve preclinical assessment in more relevant models of this complex disease. Furthermore, new environmentally-responsive antioxidant therapies show promise for clinical translation, as they target upstream mediators of vascular dysfunction such as oxidative stress rather than single downstream factors in the complex angiogenesis and arteriogenesis pathways.

Appendix A

Supplementary Information for Chapter 5

Supplemental Information from:

Poole KM, Nelson CE, Joshi RV, Martin JR, Gupta MK, Haws SC, Kavanaugh TE, Skala MC, Duvall CL. ROS-responsive microspheres for on demand antioxidant therapy in a model of diabetic peripheral arterial disease. Biomaterials. 2015; 41(0):166-175

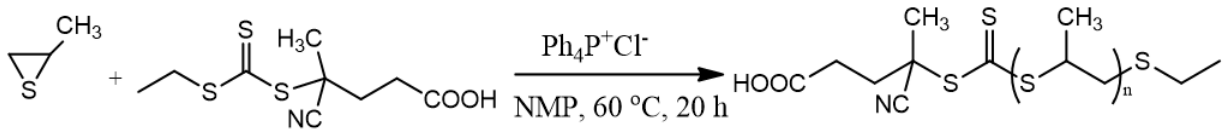

Figure A.1: Synthesis of ROS responsive PPS through TAGT polymerization.

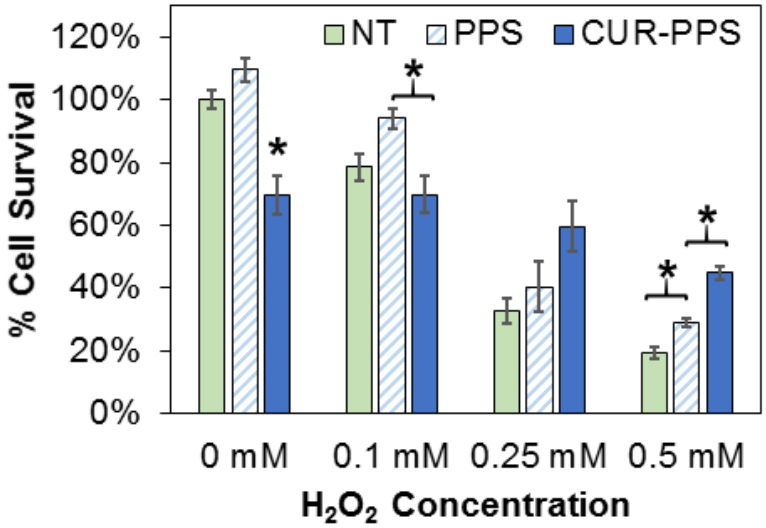

Figure A.2: Curcumin loaded PPS microparticles reduce the cytotoxicity of H_2O_2. Cell survival was measured for luciferase-expressing 3T3 fibroblasts incubated for 24 hours with blank PPS microspheres, curcumin-PPS microspheres, or vehicle in media containing varied doses of H_2O_2. Curcumin dose is 13.6 µM, and blank PPS microparticles represent the equivalent polymer dose (10.2 µg/mL PPS) used in the curcumin-loaded microparticles. *$p<0.05$ relative to other treatment groups within each H_2O_2 dose.

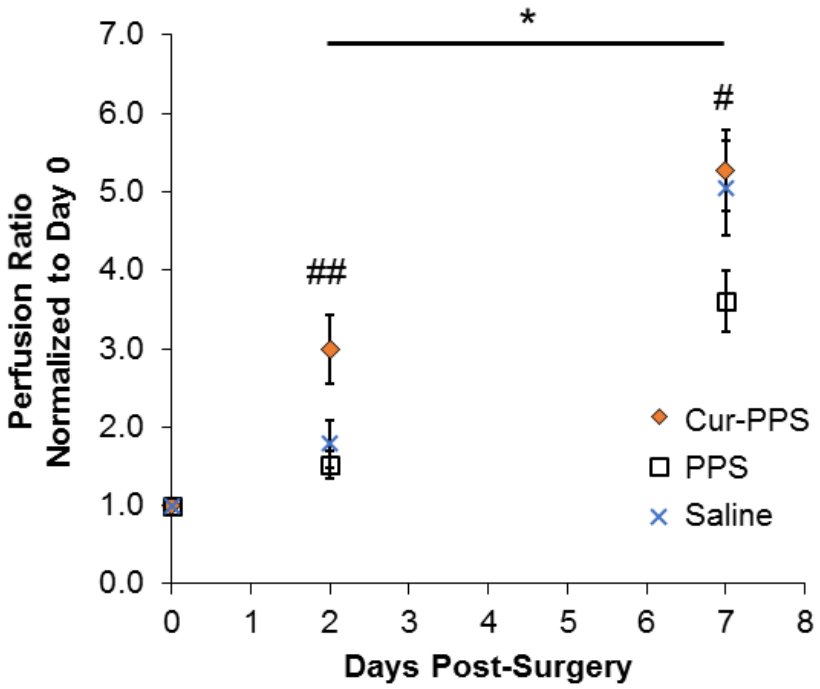

Figure A.3: Animals treated with curcumin PPS microspheres have significantly higher perfusion in the hind limb footpads at day 2 compared to animals treated with blank PPS microspheres or saline. At day 7 the curcumin-treated group had significantly higher perfusion than the blank PPS microspheres group. Data presented as mean ± SEM. * Cur-PPS group is significantly different from PPS group over the time course from day 2 to 6 ($p<0.05$). ## Cur-PPS group is significantly different from PPS and Saline ($p<0.05$). # Cur-PPS and PPS differ significantly ($p<0.05$).

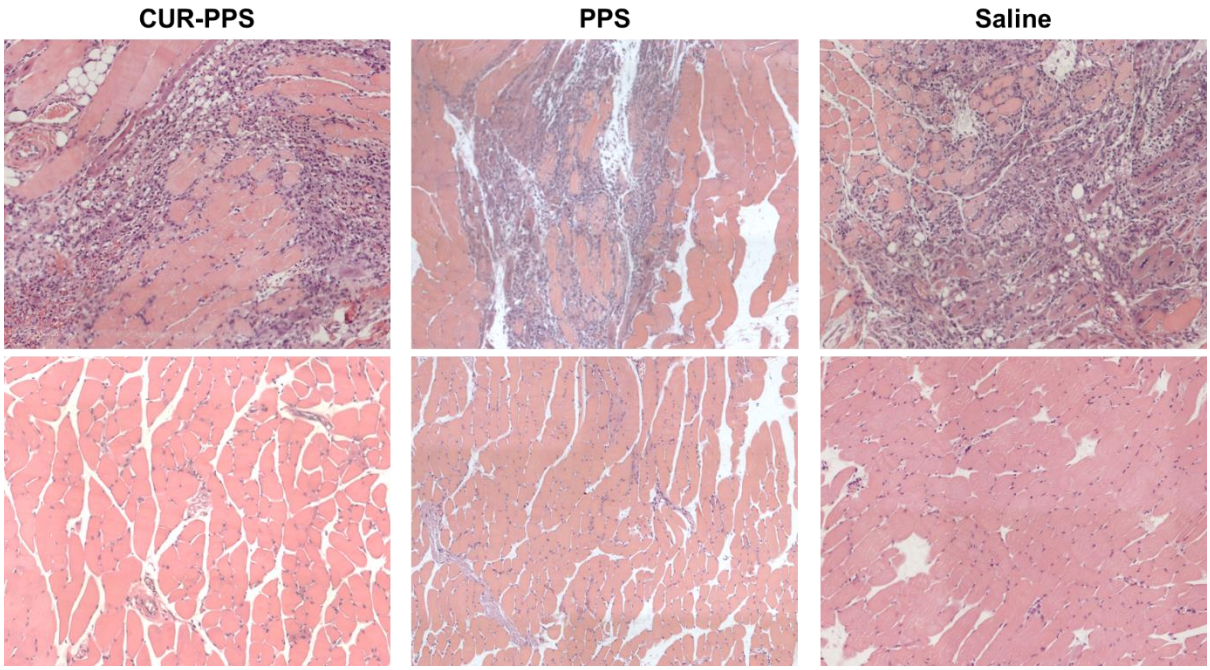

Figure A.4: Representative H&E-stained sections from the ischemic gastrocnemius muscle at day 7 for each treatment group. All treatment groups exhibit a heterogeneous host response within the muscle, with inflammatory cell infiltration in some areas likely associated with needle entry for intramuscular injection. There is no apparent, deleterious host response to the PPS microspheres beyond that which also appears in the group receiving saline injections.

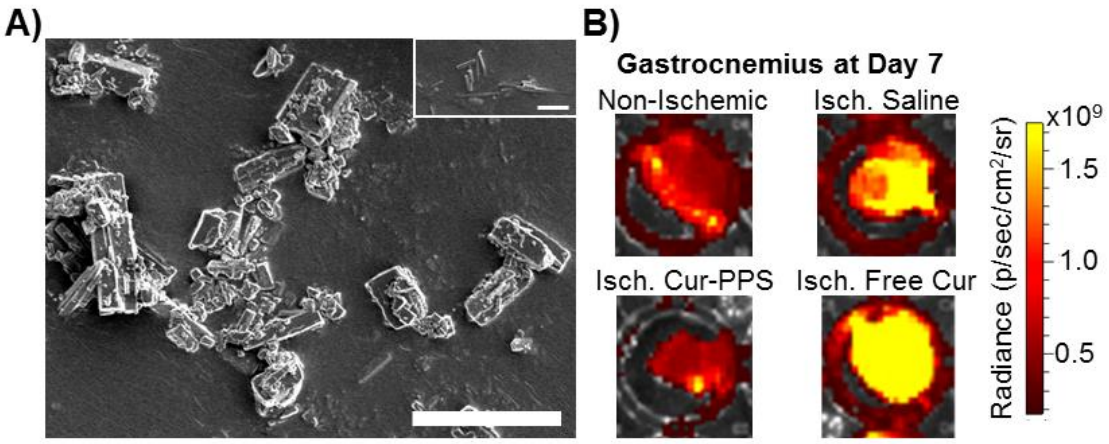

Figure A.5: Free curcumin is insoluble in aqueous solution and crystalizes, consequently increasing ROS in the ischemic muscle. A) As shown by SEM, free curcumin forms large crystals in solution. Scale bar is 30 µm. Inset shows that narrow crystals are also formed. Inset scale bar is 10 µm. B) ROS in gastrocnemius muscles extracted from ischemic limbs at day 7 is increased with free curcumin treatment compared to saline and microsphere treatments.

Appendix B

Supplementary Information for Chapter 6

Supplemental Methods

CD68 immunohistochemistry

Immunohistochemical staining was performed using commercial antibodies specifically directed against mouse CD68 (BioRad, Hercules, CA). Formalin-fixed paraffin embedded tissues were sectioned at 5 μm, collected on glass slides and incubated overnight at 60°C. Slides were deparaffinized and rehydrated with graded alcohols ending in Tris buffered saline (TBS-T Wash Buffer, LabVision, Freemont, CA). Heat mediated target retrieval was performed in 1X Target Retrieval Buffer (pH 6.0, DAKO, Carpenteria, CA). Endogenous peroxidases, non-specific background, and endogenous avidin and biotin were blocked by subsequent incubations in 3% H_2O_2 (Fisher, Suwanee, GA), serum-free Protein Block (RTU, DAKO), and Avidin/Biotin Blocking Reagent (Life Technologies, Carlsbad, CA), respectively. Primary antibody to CD68 was used at 1:200 for 1 hour, followed by secondary incubation in biotinylated anti-rat antibody (Vector Laboratories, Burlingame, CA), and then tertiary incubation in Streptavidin-HRP (BD Biosciences, San Jose, CA). Slides were rinsed with TBS-T between each reagent treatment and all steps were carried out at room temperature. Visualization was achieved with DAB+ chromogen (DAKO). Slides were counterstained with Mayer's hematoxylin, dehydrated through a series of alcohols and xylenes, and then coverslipped with Acrytol Mounting Media (Surgipath, Richmond, IL).

Nitrotyrosine immunohistochemistry

Immunohistochemical staining was performed using commercial antibodies specifically directed against mouse nitrotyrosine (AB5411, Millipore, Billerica, MA). Formalin-fixed paraffin embedded tissues were sectioned at 5 μm, collected on glass slides and incubated overnight at 60°C. Slides were deparaffinized and placed on the Leica Bond Max IHC stainer. Heat induced antigen retrieval was performed using Epitope Retrieval 1 solution for 5 minutes. Slides were placed in a Protein Block (Ref# x0909, DAKO) for 10 minutes. Slides were incubated with the primary antibody to nitrotyrosine for one hour at a 1:300 dilution. The Bond Polymer Refine detection system was used for visualization. Slides were then dehydrated, cleared, and coverslipped.

Supplemental Figures

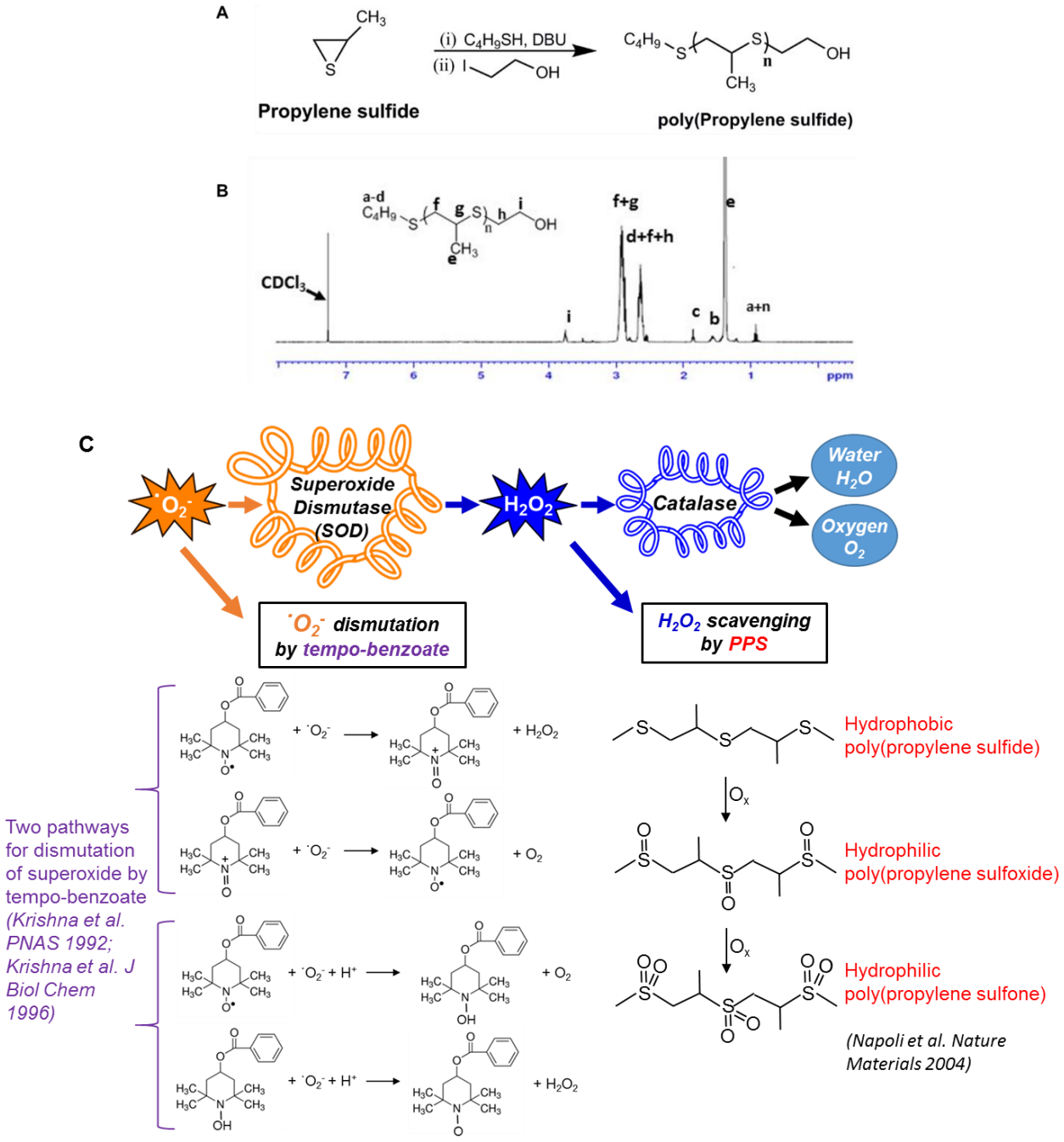

Figure B.1: A) Synthesis of poly(propylene sulfide) (PPS) by anionic polymerization of propylene sulfide. B) ^{1}H NMR spectrum for PPS polymer. C) Schematic of how tempo-benzoate and PPS mimic superoxide dismutase and catalase activity, respectively.

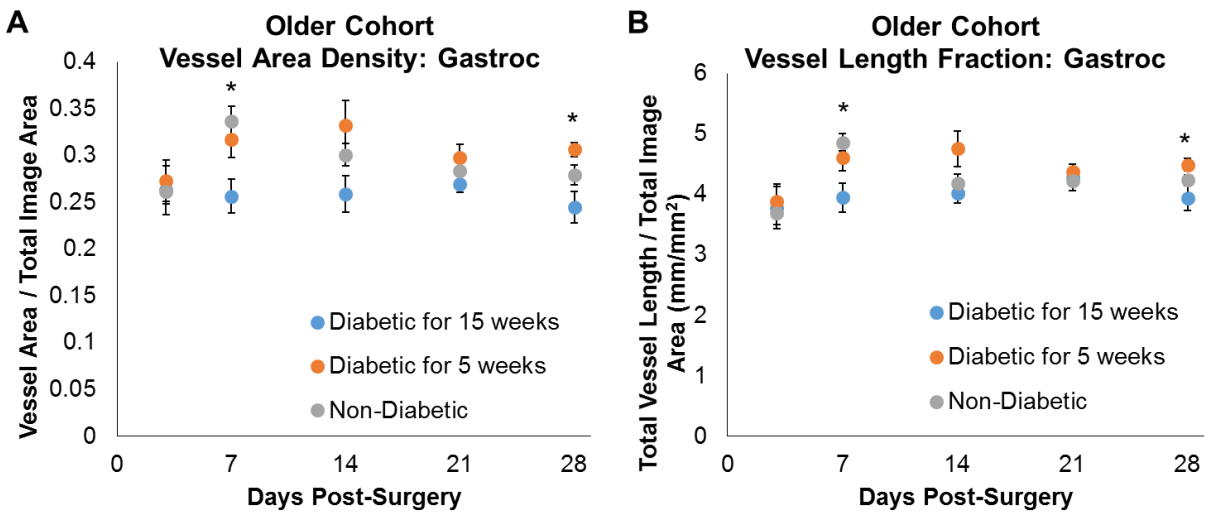

Figure B.2: In older mice, 15 weeks of diabetes significantly reduces vessel area density (A) and vessel length fraction (B) compared to age-matched non-diabetic mice and mice with only 5 weeks of diabetes. At day 7, vessel area density and vessel length fraction are significantly lower in the 15 weeks diabetic group compared to the non-diabetic group (Kruskal-Wallis ANOVA *p<0.05). At day 28, both parameters are significantly lower in the 15 weeks diabetic group compared to the 5 weeks diabetic group (Kruskal-Wallis ANOVA *p<0.05). N=9-14/group for days 3-7 and n=6-7/group for days 14-28.

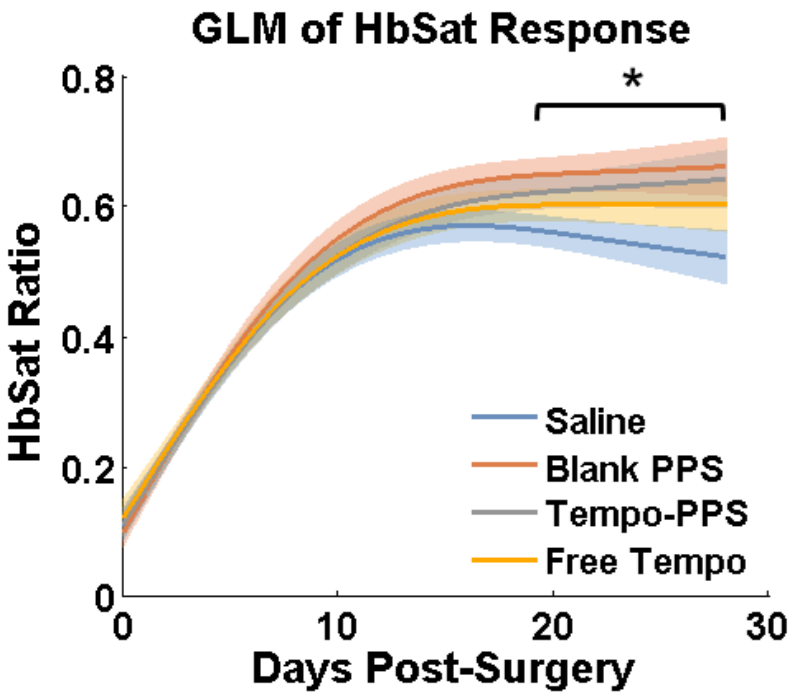

Figure B.3: General linear models for the HbSat longitudinal response for diabetic mice in the therapeutic study. A t-test performed on the general linear model curves shows that the blank PPS and saline-treated groups differ significantly from days 19 to 28 (*p<0.05).

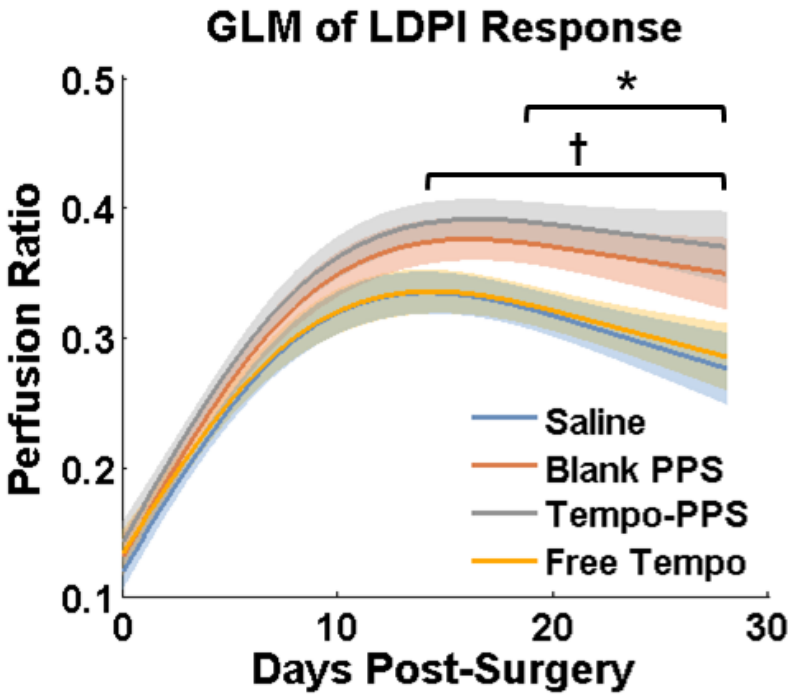

Figure B.4: The perfusion response to therapy was modeled using a general linear model. A t-test performed on the longitudinal response curves generated by the model analysis returns significant differences between blank PPS and saline (days 19-28), tempo-PPS and saline (days 14-28), and tempo-PPS and free tempo-benzoate (days 14-28). *$p<0.05$ for saline vs. blank PPS. †$p<0.05$ for tempo-PPS vs. saline and free tempo-benzoate.

.

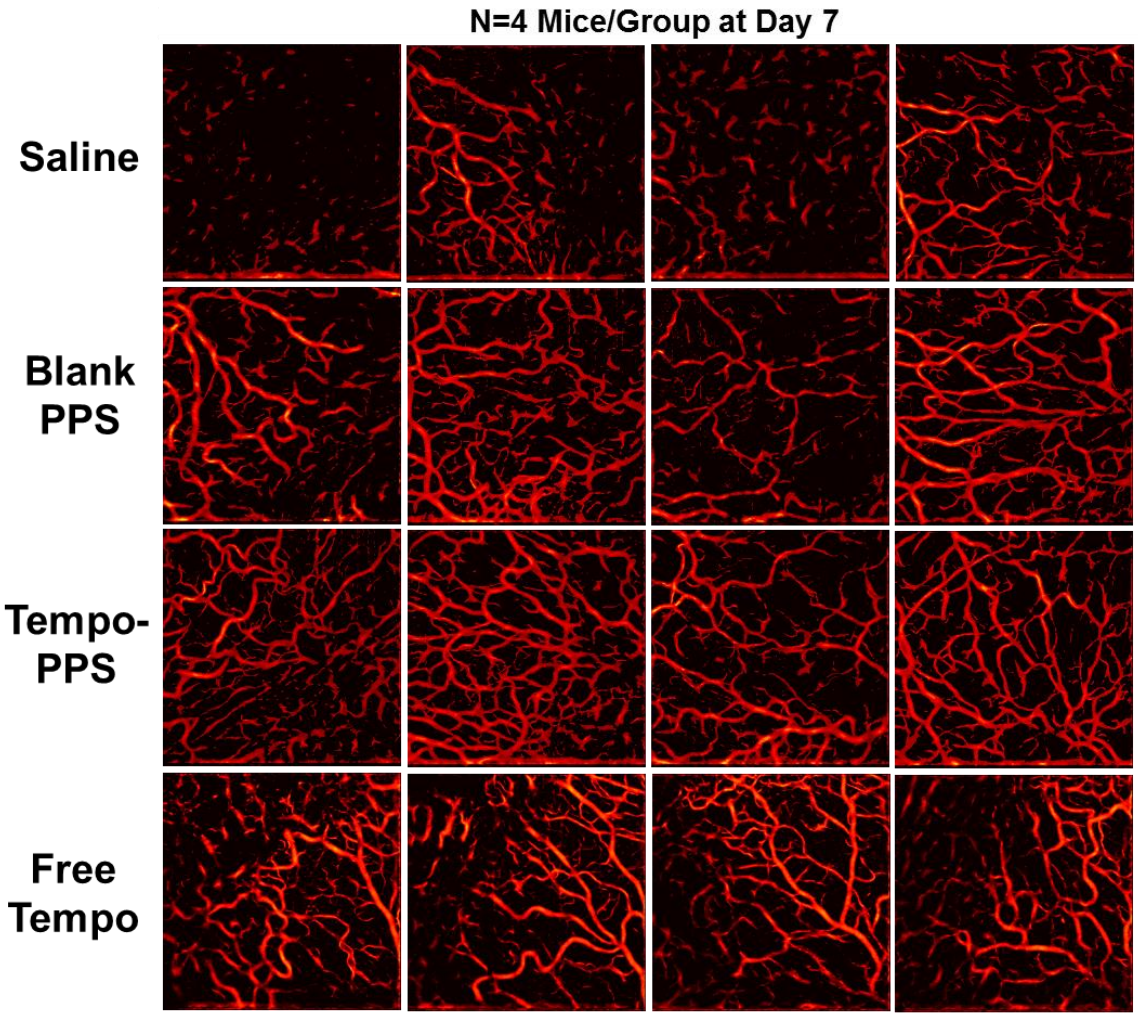

Figure B.5: Additional representative OCT images for the adductor region are shown for day 7, the time at which statistically significant differences are detected between the treatment groups. At this time point, the blank PPS and tempo-PPS treatment groups tend to have a greater vessel density compared to the saline and free tempo-benzoate groups. Images are from 4 different mice per treatment group and consist of an average intensity projection covering a 4 mm x 4 mm area.

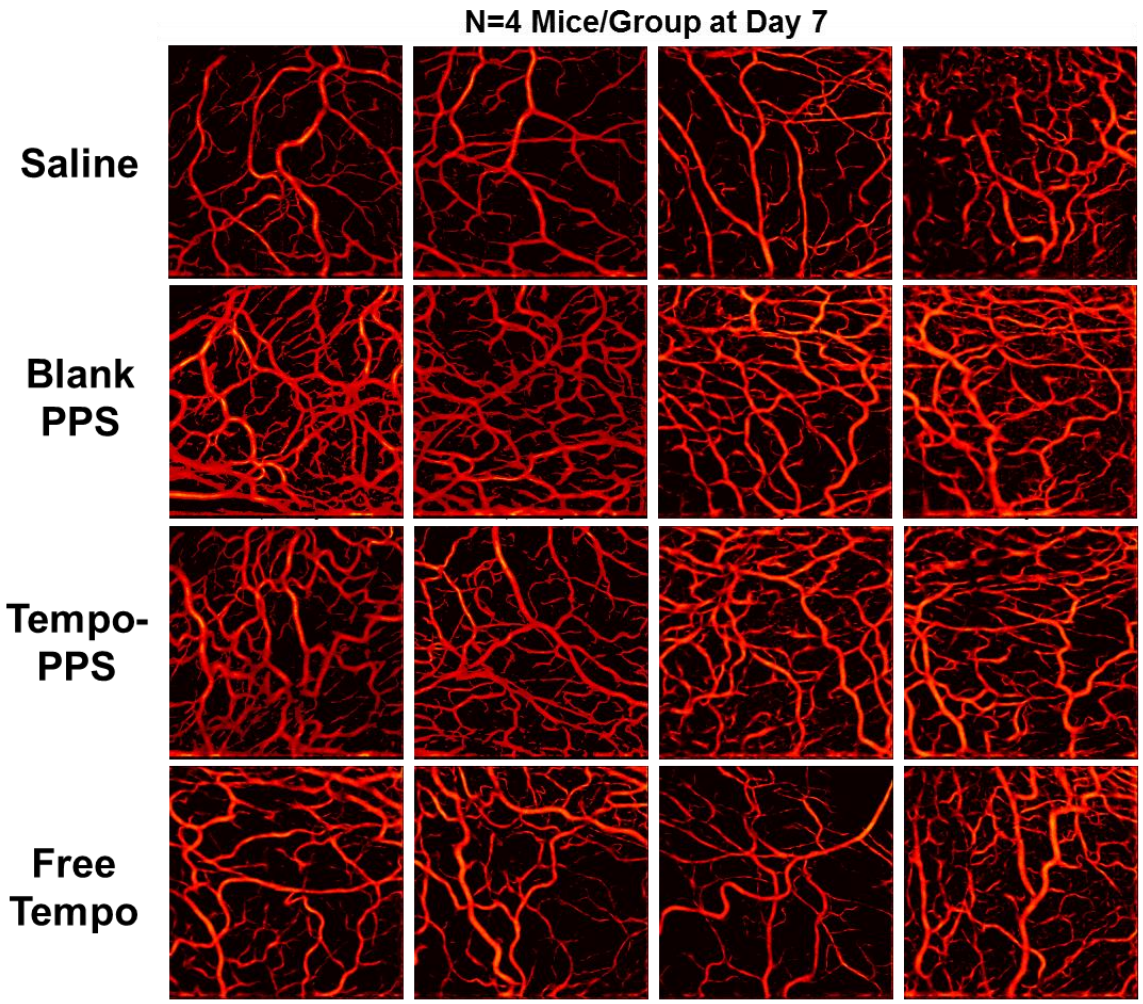

Figure B.6: Additional representative OCT images are shown for the gastrocnemius region at day 7. At this time point, the blank PPS group tends to have the greatest vessel density while the saline group has the least vessels. Images are from 4 different mice per treatment group and consist of an average intensity projection covering a 4 mm x 4 mm area.

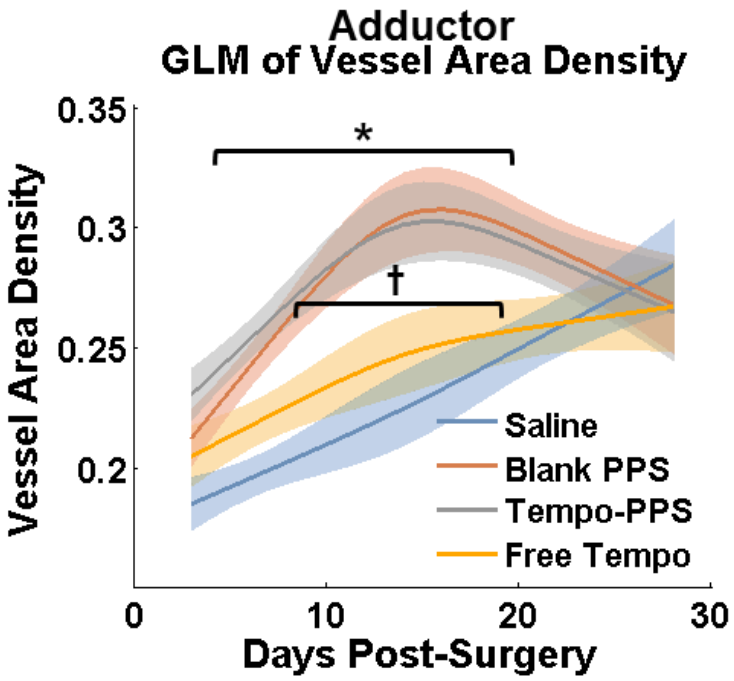

Figure B.7: The vessel morphology response to therapy in the adductor muscle region was modeled using a general linear model. Analysis of the resulting longitudinal response curves for vessel area density shows that the saline group differs significantly from the blank PPS and tempo-PPS groups (for days 4-21 and 3-20, respectively), and the free tempo-benzoate group differs significantly from the blank PPS and tempo-PPS groups (days 7-19). *$p<0.05$ for saline vs. blank PPS and free tempo-benzoate. †$p<0.05$ for blank PPS vs. tempo-PPS and free tempo-benzoate.

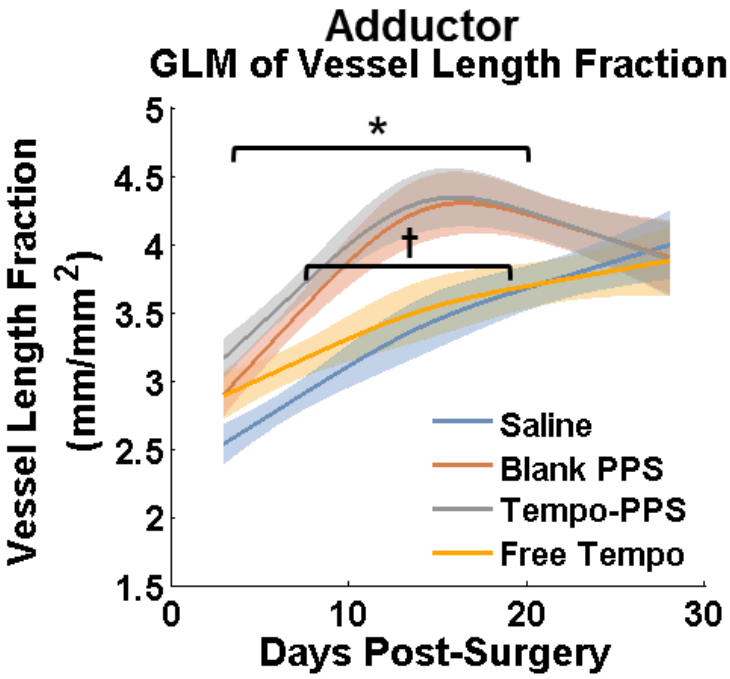

Figure B.8: Analysis of the GLM curves for vessel length fraction in the adductor muscle shows that the saline group differs significantly from the blank PPS and tempo-PPS groups (for days 4-20 and 3-20, respectively), and the free tempo-benzoate group differs significantly from the blank PPS and tempo-PPS groups (for days 9-19 and 5-20, respectively). *$p<0.05$ for saline vs. blank PPS and tempo-PPS. †$p<0.05$ for free tempo-benzoate vs. blank PPS and tempo-PPS.

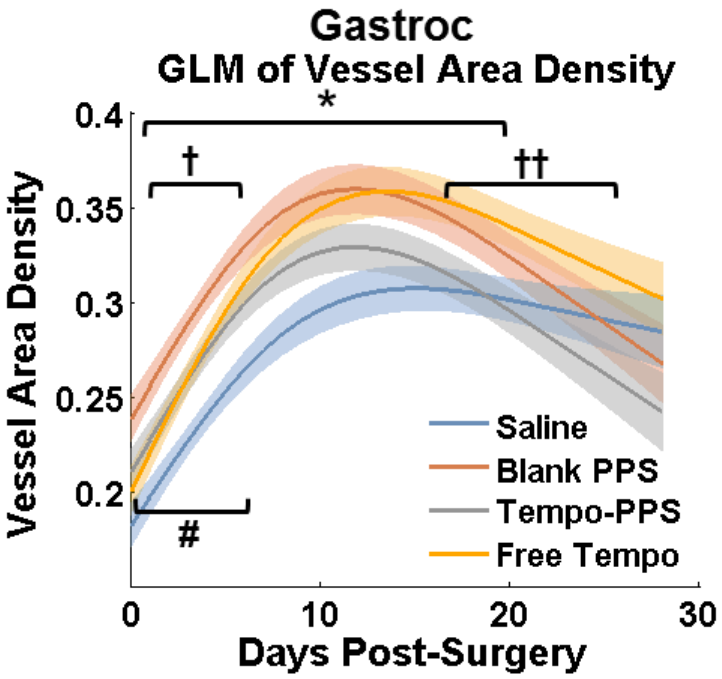

Figure B.9: Analysis of GLM curves for vessel area density in the gastrocnemius shows that the saline group differs significantly from blank PPS (days 0-17), tempo-PPS (days 0-7), and free tempo-benzoate (days 2-20). The blank PPS group differs significantly from the tempo-PPS and free tempo-benzoate groups at early time points (days 2-6 and 0-4, respectively). Finally, the tempo-PPS and free tempo-benzoate groups differ significantly for later time points (days 17-26). *$p<0.05$ for saline vs. blank PPS and free tempo-benzoate. †$p<0.05$ for blank PPS vs. tempo-PPS and free tempo-benzoate. #$p<0.05$ for saline vs. tempo-PPS. ††$p<0.05$ for free tempo-benzoate vs. tempo-PPS.

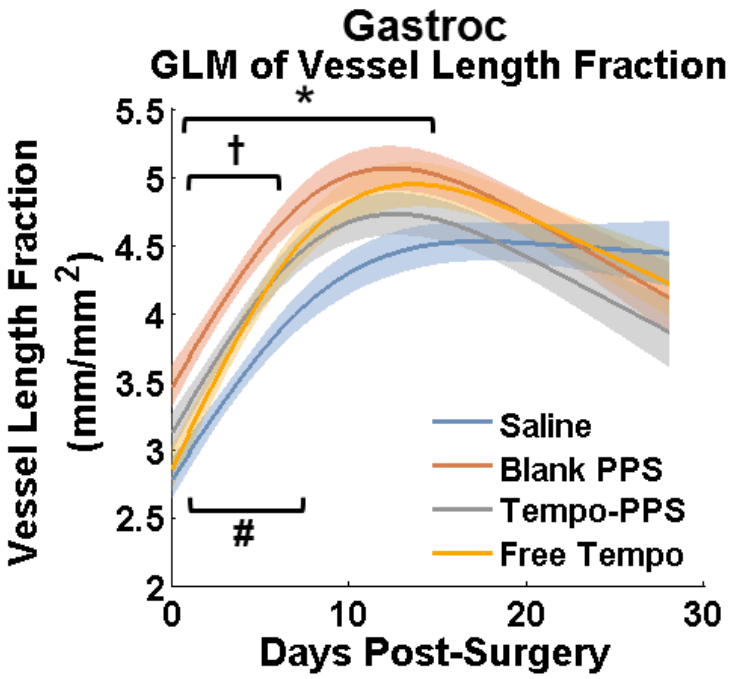

Figure B.10: Analysis of GLM curves for vessel length fraction in the gastrocnemius shows that the saline group differs significantly from blank PPS (days 0-15), tempo-PPS (days 1-7), and free tempo-benzoate (days 4-12). The blank PPS group differs significantly from the tempo-PPS and free tempo-benzoate groups at early time points (days 2-6 and 0-5, respectively). Tempo-PPS and free tempo-benzoate are not statistically different at any time point. *$p<0.05$ for saline vs. blank PPS and free tempo-benzoate. †$p<0.05$ for blank PPS vs. tempo-PPS and free tempo-benzoate. #$p<0.05$ for saline vs. tempo-PPS.

REFERENCES

[1] Roger VL, Go AS, Lloyd-Jones DM, Benjamin EJ, Berry JD, Borden WB, et al. Heart Disease and Stroke Statistics--2012 Update: A Report From the American Heart Association. Circulation. 2012;125:e2-e220.

[2] Peripheral arterial disease in people with diabetes. Diabetes care. 2003;26:3333-41.

[3] Weitz JI, Byrne J, Clagett GP, Farkouh ME, Porter JM, Sackett DL, et al. Diagnosis and treatment of chronic arterial insufficiency of the lower extremities: a critical review. Circulation. 1996;94:3026-49.

[4] Leeper NJ, Kullo IJ, Cooke JP. Genetics of peripheral artery disease. Circulation.125:3220-8.

[5] Petznick AM, Shubrook JH. Treatment of specific macrovascular beds in patients with diabetes mellitus. Osteopath Med Prim Care. 2010;4:5.

[6] Gupta R, Tongers J, Losordo DW. Human studies of angiogenic gene therapy. Circulation research. 2009;105:724-36.

[7] Nikol S, Baumgartner I, Van Belle E, Diehm C, Visona A, Capogrossi MC, et al. Therapeutic angiogenesis with intramuscular NV1FGF improves amputation-free survival in patients with critical limb ischemia. Molecular therapy : the journal of the American Society of Gene Therapy. 2008;16:972-8.

[8] Powell RJ, Simons M, Mendelsohn FO, Daniel G, Henry TD, Koga M, et al. Results of a double-blind, placebo-controlled study to assess the safety of intramuscular injection of hepatocyte growth factor plasmid to improve limb perfusion in patients with critical limb ischemia. Circulation. 2008;118:58-65.

[9] Makino H, Aoki M, Hashiya N, Yamasaki K, Azuma J, Sawa Y, et al. Long-term follow-up evaluation of results from clinical trial using hepatocyte growth factor gene to treat severe peripheral arterial disease. Arteriosclerosis, thrombosis, and vascular biology. 2012;32:2503-9.

[10] Marui A, Tabata Y, Kojima S, Yamamoto M, Tambara K, Nishina T, et al. A novel approach to therapeutic angiogenesis for patients with critical limb ischemia by sustained release of basic fibroblast growth factor using biodegradable gelatin hydrogel: an initial report of the phase I-IIa study. Circ J. 2007;71:1181-6.

[11] Couffinhal T, Silver M, Zheng LP, Kearney M, Witzenbichler B, Isner JM. Mouse model of angiogenesis. The American journal of pathology. 1998;152:1667-79.

[12] Gounis MJ, Spiga MG, Graham RM, Wilson A, Haliko S, Lieber BB, et al. Angiogenesis is confined to the transient period of VEGF expression that follows adenoviral gene delivery to ischemic muscle. Gene Therapy. 2005;12:762-71.

[13] Landazuri N, Joseph G, Guldberg RE, Taylor WR. Growth and regression of vasculature in healthy and diabetic mice after hindlimb ischemia. Am J Physiol Regul Integr Comp Physiol. 2012;303:R48-56.

[14] Steffen LM, Duprez DA, Boucher JL, Ershow AG, Hirsch AT. Management of Peripheral Arterial Disease. Diabetes Spectrum. 2008;21:171-7.

[15] Jude EB, Oyibo SO, Chalmers N, Boulton AJ. Peripheral arterial disease in diabetic and nondiabetic patients: a comparison of severity and outcome. Diabetes care. 2001;24:1433-7.

[16] Papanas N, Maltezos E. Advances in treating the ischaemic diabetic foot. Curr Vasc Pharmacol. 2008;6:23-8.

[17] Rees DA, Alcolado JC. Animal models of diabetes mellitus. Diabet Med. 2005;22:359-70.

[18] Bir SC, Esaki J, Marui A, Sakaguchi H, Kevil CG, Ikeda T, et al. Therapeutic treatment with sustained-release platelet-rich plasma restores blood perfusion by augmenting ischemia-induced angiogenesis and arteriogenesis in diabetic mice. J Vasc Res. 2011;48:195-205.

[19] Raiter A, Bechor Z, Kleiman M, Leshem-Lev D, Battler A, Hardy B. Angiogenic peptides improve blood flow and promote capillary growth in a diabetic and ischaemic mouse model. European journal of vascular and endovascular surgery : the official journal of the European Society for Vascular Surgery. 2011;40:381-8.

[20] Golub JS, Kim YT, Duvall CL, Bellamkonda RV, Gupta D, Lin AS, et al. Sustained VEGF delivery via PLGA nanoparticles promotes vascular growth. American journal of physiology Heart and circulatory physiology. 2010;298:H1959-65.

[21] Duvall CL, Taylor WR, Weiss D, Guldberg RE. Quantitative microcomputed tomography analysis of collateral vessel development after ischemic injury. American journal of physiology Heart and circulatory physiology. 2004;287:H302-10.

[22] Duvall CL, Weiss D, Robinson ST, Alameddine FM, Guldberg RE, Taylor WR. The role of osteopontin in recovery from hind limb ischemia. Arteriosclerosis, thrombosis, and vascular biology. 2008;28:290-5.

[23] Scholz D, Ziegelhoeffer T, Helisch A, Wagner S, Friedrich C, Podzuweit T, et al. Contribution of arteriogenesis and angiogenesis to postocclusive hindlimb perfusion in mice. J Mol Cell Cardiol. 2002;34:775-87.

[24] Jones WS, Annex BH. Growth factors for therapeutic angiogenesis in peripheral arterial disease. Curr Opin Cardiol. 2007;22:458-63.

[25] Tongers J, Roncalli JG, Losordo DW. Therapeutic angiogenesis for critical limb ischemia: microvascular therapies coming of age. Circulation. 2008;118:9-16.

[26] Shonat RD, Wachman ES, Niu W, Koretsky AP, Farkas DL. Near-simultaneous hemoglobin saturation and oxygen tension maps in mouse brain using an AOTF microscope. Biophys J. 1997;73:1223-31.

[27] Sorg BS, Moeller BJ, Donovan O, Cao Y, Dewhirst MW. Hyperspectral imaging of hemoglobin saturation in tumor microvasculature and tumor hypoxia development. Journal of biomedical optics. 2005;10:44004.

[28] Palmer GM, Fontanella AN, Shan S, Hanna G, Zhang G, Fraser CL, et al. In vivo optical molecular imaging and analysis in mice using dorsal window chamber models applied to hypoxia, vasculature and fluorescent reporters. Nat Protoc. 2011;6:1355-66.

[29] Fujimoto JG. Optical coherence tomography for ultrahigh resolution in vivo imaging. Nature biotechnology. 2003;21:1361-7.

[30] Vakoc BJ, Fukumura D, Jain RK, Bouma BE. Cancer imaging by optical coherence tomography: preclinical progress and clinical potential. Nature Reviews Cancer. 2012;12:363-8.

[31] Yazdanfar S, Kulkarni M, Izatt J. High resolution imaging of in vivo cardiac dynamics using color Doppler optical coherence tomography. Optics express. 1997;1:424-31.

[32] Izatt JA, Kulkarni MD, Yazdanfar S, Barton JK, Welch AJ. In vivo bidirectional color Doppler flow imaging of picoliter blood volumes using optical coherence tomography. Optics letters. 1997;22:1439-41.

[33] Drexler W, Fujimoto JG. State-of-the-art retinal optical coherence tomography. Prog Retin Eye Res. 2008;27:45-88.

[34] Pierce MC, Strasswimmer J, Park BH, Cense B, de Boer JF. Advances in optical coherence tomography imaging for dermatology. J Invest Dermatol. 2004;123:458-63.

[35] Skala MC, Fontanella A, Hendargo H, Dewhirst MW, Izatt JA. Combined hyperspectral and spectral domain optical coherence tomography microscope for noninvasive hemodynamic imaging. Optics letters. 2009;34:289-91.

[36] Skala MC, Fontanella A, Lan L, Izatt JA, Dewhirst MW. Longitudinal optical imaging of tumor metabolism and hemodynamics. Journal of biomedical optics. 2010;15:011112.

[37] Jia Y, Qin J, Zhi Z, Wang RK. Ultrahigh sensitive optical microangiography reveals depth-resolved microcirculation and its longitudinal response to prolonged ischemic event within skeletal muscles in mice. Journal of biomedical optics. 2011;16:086004.

[38] Gu S, Jenkins MW, Peterson LM, Doughman YQ, Rollins AM, Watanabe M. Optical coherence tomography captures rapid hemodynamic responses to acute hypoxia in the cardiovascular system of early embryos. Dev Dyn. 2012;241:534-44.

[39] Mariampillai A, Standish BA, Moriyama EH, Khurana M, Munce NR, Leung MK, et al. Speckle variance detection of microvasculature using swept-source optical coherence tomography. Optics letters. 2008;33:1530-2.

[40] Simons M, Annex BH, Laham RJ, Kleiman N, Henry T, Dauerman H, et al. Pharmacological treatment of coronary artery disease with recombinant fibroblast growth factor-2: double-blind, randomized, controlled clinical trial. Circulation. 2002;105:788-93.

[41] Giugliano D, Ceriello A, Paolisso G. Oxidative stress and diabetic vascular complications. Diabetes care. 1996;19:257-67.

[42] Kojda G, Harrison D. Interactions between NO and reactive oxygen species: pathophysiological importance in atherosclerosis, hypertension, diabetes and heart failure. Cardiovascular research. 1999;43:562-71.

[43] Ebrahimian TG, Heymes C, You D, Blanc-Brude O, Mees B, Waeckel L, et al. NADPH oxidase-derived overproduction of reactive oxygen species impairs postischemic neovascularization in mice with type 1 diabetes. The American journal of pathology. 2006;169:719-28.

[44] Ceradini DJ, Yao D, Grogan RH, Callaghan MJ, Edelstein D, Brownlee M, et al. Decreasing intracellular superoxide corrects defective ischemia-induced new vessel formation in diabetic mice. The Journal of biological chemistry. 2008;283:10930-8.

[45] Rivard A, Silver M, Chen D, Kearney M, Magner M, Annex B, et al. Rescue of diabetes-related impairment of angiogenesis by intramuscular gene therapy with adeno-VEGF. The American journal of pathology. 1999;154:355-63.

[46] Purcell BP, Lobb D, Charati MB, Dorsey SM, Wade RJ, Zellars KN, et al. Injectable and bioresponsive hydrogels for on-demand matrix metalloproteinase inhibition. Nature materials. 2014;13:653-61.

[47] Wilson DS, Dalmasso G, Wang L, Sitaraman SV, Merlin D, Murthy N. Orally delivered thioketal nanoparticles loaded with TNF-alpha-siRNA target inflammation and inhibit gene expression in the intestines. Nature materials. 2010;9:923-8.

[48] Lee D, Bae S, Hong D, Lim H, Yoon JH, Hwang O, et al. H2O2-responsive molecularly engineered polymer nanoparticles as ischemia/reperfusion-targeted nanotherapeutic agents. Scientific reports. 2013;3:2233.

[49] Gupta MK, Martin JR, Werfel TA, Shen T, Page JM, Duvall CL. Cell Protective, ABC Triblock Polymer-Based Thermoresponsive Hydrogels with ROS-Triggered Degradation and Drug Release. Journal of the American Chemical Society. 2014;136:14896-902.

[50] Zbinden S, Clavijo LC, Kantor B, Morsli H, Cortes GA, Andrews JA, et al. Interanimal variability in preexisting collaterals is a major factor determining outcome in experimental angiogenesis trials. American journal of physiology Heart and circulatory physiology. 2007;292:H1891-7.

[51] Stevens JC, Banks GT, Festing MF, Fisher EM. Quiet mutations in inbred strains of mice. Trends Mol Med. 2007;13:512-9.

[52] Watkins-Chow DE, Pavan WJ. Genomic copy number and expression variation within the C57BL/6J inbred mouse strain. Genome Res. 2008;18:60-6.

[53] Khurana R, Simons M, Martin JF, Zachary IC. Role of angiogenesis in cardiovascular disease: a critical appraisal. Circulation. 2005;112:1813-24.

[54] Carmelli D, Fabsitz RR, Swan GE, Reed T, Miller B, Wolf PA. Contribution of genetic and environmental influences to ankle-brachial blood pressure index in the NHLBI Twin Study. National Heart, Lung, and Blood Institute. Am J Epidemiol. 2000;151:452-8.

[55] Hink U, Li H, Mollnau H, Oelze M, Matheis E, Hartmann M, et al. Mechanisms underlying endothelial dysfunction in diabetes mellitus. Circulation research. 2001;88:E14-22.

[56] Brownlee M. Biochemistry and molecular cell biology of diabetic complications. Nature. 2001;414:813-20.

[57] Kullo IJ, Turner ST, Kardia SL, Mosley TH, Jr., Boerwinkle E, de Andrade M. A genome-wide linkage scan for ankle-brachial index in African American and non-Hispanic white subjects participating in the GENOA study. Atherosclerosis. 2006;187:433-8.

[58] Murabito JM, Guo CY, Fox CS, D'Agostino RB. Heritability of the ankle-brachial index: the Framingham Offspring study. Am J Epidemiol. 2006;164:963-8.

[59] Hirsch AT, Criqui MH, Treat-Jacobson D, Regensteiner JG, Creager MA, Olin JW, et al. Peripheral arterial disease detection, awareness, and treatment in primary care. Jama. 2001;286:1317-24.

[60] Hankey GJ, Norman PE, Eikelboom JW. Medical treatment of peripheral arterial disease. Jama. 2006;295:547-53.

[61] Morishita R. Perspective in progress of cardiovascular gene therapy. J Pharmacol Sci. 2004;95:1-8.

[62] Baumgartner I, Pieczek A, Manor O, Blair R, Kearney M, Walsh K, et al. Constitutive expression of phVEGF165 after intramuscular gene transfer promotes collateral vessel development in patients with critical limb ischemia. Circulation. 1998;97:1114-23.

[63] Comerota AJ, Throm RC, Miller KA, Henry T, Chronos N, Laird J, et al. Naked plasmid DNA encoding fibroblast growth factor type 1 for the treatment of end-stage unreconstructible lower extremity ischemia: preliminary results of a phase I trial. Journal of vascular surgery. 2002;35:930-6.

[64] Taniyama Y, Morishita R, Aoki M, Nakagami H, Yamamoto K, Yamazaki K, et al. Therapeutic angiogenesis induced by human hepatocyte growth factor gene in rat and rabbit

hindlimb ischemia models: preclinical study for treatment of peripheral arterial disease. Gene Ther. 2001;8:181-9.

[65] Mesquita RC, Skuli N, Kim MN, Liang J, Schenkel S, Majmundar AJ, et al. Hemodynamic and metabolic diffuse optical monitoring in a mouse model of hindlimb ischemia. Biomedical optics express. 2010;1:1173-87.

[66] Cao R, Brakenhielm E, Pawliuk R, Wariaro D, Post MJ, Wahlberg E, et al. Angiogenic synergism, vascular stability and improvement of hind-limb ischemia by a combination of PDGF-BB and FGF-2. Nature medicine. 2003;9:604-13.

[67] Limbourg A, Korff T, Napp LC, Schaper W, Drexler H, Limbourg FP. Evaluation of postnatal arteriogenesis and angiogenesis in a mouse model of hind-limb ischemia. Nat Protoc. 2009;4:1737-46.

[68] Lee K, Qian DZ, Rey S, Wei H, Liu JO, Semenza GL. Anthracycline chemotherapy inhibits HIF-1 transcriptional activity and tumor-induced mobilization of circulating angiogenic cells. P Natl Acad Sci USA. 2009;106:2353-8.

[69] Helisch A, Wagner S, Khan N, Drinane M, Wolfram S, Heil M, et al. Impact of mouse strain differences in innate hindlimb collateral vasculature. Arteriosclerosis, thrombosis, and vascular biology. 2006;26:520-6.

[70] Palmer GM, Viola RJ, Schroeder T, Yarmolenko PS, Dewhirst MW, Ramanujam N. Quantitative diffuse reflectance and fluorescence spectroscopy: tool to monitor tumor physiology in vivo. Journal of biomedical optics. 2009;14:024010.

[71] Brown EB, Campbell RB, Tsuzuki Y, Xu L, Carmeliet P, Fukumura D, et al. In vivo measurement of gene expression, angiogenesis and physiological function in tumors using multiphoton laser scanning microscopy. Nature medicine. 2001;7:864-8.

[72] Zhang HF, Maslov K, Stoica G, Wang LV. Functional photoacoustic microscopy for high-resolution and noninvasive in vivo imaging. Nature biotechnology. 2006;24:848-51.

[73] Wang LV, Gao L. Photoacoustic microscopy and computed tomography: from bench to bedside. Annual review of biomedical engineering. 2014;16:155-85.

[74] Rege A, Thakor NV, Rhie K, Pathak AP. In vivo laser speckle imaging reveals microvascular remodeling and hemodynamic changes during wound healing angiogenesis. Angiogenesis. 2012;15:87-98.

[75] Dunn AK, Bolay H, Moskowitz MA, Boas DA. Dynamic imaging of cerebral blood flow using laser speckle. Journal of cerebral blood flow and metabolism : official journal of the International Society of Cerebral Blood Flow and Metabolism. 2001;21:195-201.

[76] Goertz DE, Yu JL, Kerbel RS, Burns PN, Foster FS. High-frequency 3-D color-flow imaging of the microcirculation. Ultrasound in medicine & biology. 2003;29:39-51.

[77] Jacoby C, Boring YC, Beck A, Zernecke A, Aurich V, Weber C, et al. Dynamic changes in murine vessel geometry assessed by high-resolution magnetic resonance angiography: a 9.4T study. J Magn Reson Imaging. 2008;28:637-45.

[78] Khaodhiar L, Dinh T, Schomacker KT, Panasyuk SV, Freeman JE, Lew R, et al. The use of medical hyperspectral technology to evaluate microcirculatory changes in diabetic foot ulcers and to predict clinical outcomes. Diabetes care. 2007;30:903-10.

[79] Srinivasan VJ, Jiang JY, Yaseen MA, Radhakrishnan H, Wu W, Barry S, et al. Rapid volumetric angiography of cortical microvasculature with optical coherence tomography. Optics letters. 2010;35:43-5.

[80] Altunbas A, Lee SJ, Rajasekaran SA, Schneider JP, Pochan DJ. Encapsulation of curcumin in self-assembling peptide hydrogels as injectable drug delivery vehicles. Biomaterials. 2011;32:5906-14.

[81] Sun D, Zhuang X, Xiang X, Liu Y, Zhang S, Liu C, et al. A novel nanoparticle drug delivery system: the anti-inflammatory activity of curcumin is enhanced when encapsulated in exosomes. Molecular therapy : the journal of the American Society of Gene Therapy. 2010;18:1606-14.

[82] Pu HL, Chiang WL, Maiti B, Liao ZX, Ho YC, Shim MS, et al. Nanoparticles with dual responses to oxidative stress and reduced ph for drug release and anti-inflammatory applications. ACS nano. 2014;8:1213-21.

[83] Shahani K, Swaminathan SK, Freeman D, Blum A, Ma L, Panyam J. Injectable sustained release microparticles of curcumin: a new concept for cancer chemoprevention. Cancer research. 2010;70:4443-52.

[84] Zhu G, Mallery SR, Schwendeman SP. Stabilization of proteins encapsulated in injectable poly (lactide- co-glycolide). Nature biotechnology. 2000;18:52-7.

[85] Vert M, Li S, Garreau H. More About the Degradation of La/Ga-Derived Matrices in Aqueous-Media. Journal of Controlled Release. 1991;16:15-26.

[86] Napoli A, Valentini M, Tirelli N, Muller M, Hubbell JA. Oxidation-responsive polymeric vesicles. Nature materials. 2004;3:183-9.

[87] Reddy ST, Rehor A, Schmoekel HG, Hubbell JA, Swartz MA. In vivo targeting of dendritic cells in lymph nodes with poly(propylene sulfide) nanoparticles. Journal of controlled release : official journal of the Controlled Release Society. 2006;112:26-34.

[88] Hu P, Tirelli N. Scavenging ROS: superoxide dismutase/catalase mimetics by the use of an oxidation-sensitive nanocarrier/enzyme conjugate. Bioconjugate chemistry. 2012;23:438-49.

[89] Velluto D, Demurtas D, Hubbell JA. PEG-b-PPS diblock copolymer aggregates for hydrophobic drug solubilization and release: cyclosporin A as an example. Molecular pharmaceutics. 2008;5:632-42.

[90] Gupta MK, Meyer TA, Nelson CE, Duvall CL. Poly(PS-b-DMA) micelles for reactive oxygen species triggered drug release. Journal of controlled release : official journal of the Controlled Release Society. 2012;162:591-8.

[91] Poole KM, Nelson CE, Joshi RV, Martin JR, Gupta MK, Haws SC, et al. ROS-responsive microspheres for on demand antioxidant therapy in a model of diabetic peripheral arterial disease. Biomaterials. 2015;41:166-75.

[92] Duvall CL, Taylor WR, Weiss D, Wojtowicz AM, Guldberg RE. Impaired angiogenesis, early callus formation, and late stage remodeling in fracture healing of osteopontin-deficient mice. J Bone Miner Res. 2007;22:286-97.

[93] Chalothorn D, Faber JE. Strain-dependent variation in collateral circulatory function in mouse hindlimb. Physiol Genomics. 2010;42:469-79.

[94] Gebhart SC, Thompson RC, Mahadevan-Jansen A. Liquid-crystal tunable filter spectral imaging for brain tumor demarcation. Applied optics. 2007;46:1896-910.

[95] Jacques SL. Skin Optics. Oregon Medical Laser Center News; 1998.

[96] Skala MC, Tao YK, Davis AM, Izatt JA. Functional Optical Coherence Tomography in Preclinical Models. In: Boas DA, Pitris C, Ramanujam N, editors. Handbook of biomedical optics. Boca Raton: CRC Press; 2011. p. 281-302.

[97] Bower BA, Zhao M, Zawadzki RJ, Izatt JA. Real-time spectral domain Doppler optical coherence tomography and investigation of human retinal vessel autoregulation. Journal of biomedical optics. 2007;12:041214.

[98] Makita S, Hong Y, Yamanari M, Yatagai T, Yasuno Y. Optical coherence angiography. Optics express. 2006;14:7821-40.

[99] Standish BA, Yang VXD, Munce NR, Song LMWK, Gardiner G, Lin A, et al. Doppler optical coherence tomography monitoring of microvascular tissue response during photodynamic therapy in an animal model of Barrett's esophagus. Gastrointestinal Endoscopy. 2007;66:326-33.

[100] Pearson K. Mathematical Contributions to the Theory of Evolution. III. Regression, Heredity, and Panmixia. Philos T R Soc A. 1896;187:253-318.

[101] Braun RD, Lanzen JL, Snyder SA, Dewhirst MW. Comparison of tumor and normal tissue oxygen tension measurements using OxyLite or microelectrodes in rodents. American Journal of Physiology-Heart and Circulatory Physiology. 2001;280:H2533-H44.

[102] Ito WD, Arras M, Winkler B, Scholz D, Schaper J, Schaper W. Monocyte chemotactic protein-1 increases collateral and peripheral conductance after femoral artery occlusion. Circulation research. 1997;80:829-37.

[103] Davis AM, Rothenberg FG, Shepherd N, Izatt JA. In vivo spectral domain optical coherence tomography volumetric imaging and spectral Doppler velocimetry of early stage embryonic chicken heart development. J Opt Soc Am A Opt Image Sci Vis. 2008;25:3134-43.

[104] Rao B, Yu L, Chiang HK, Zacharias LC, Kurtz RM, Kuppermann BD, et al. Imaging pulsatile retinal blood flow in human eye. Journal of biomedical optics. 2008;13:040505.

[105] Yang V, Gordon M, Qi B, Pekar J, Lo S, Seng-Yue E, et al. High speed, wide velocity dynamic range Doppler optical coherence tomography (Part I): System design, signal processing, and performance. Optics express. 2003;11:794-809.

[106] Brevetti LS, Paek R, Brady SE, Hoffman JI, Sarkar R, Messina LM. Exercise-induced hyperemia unmasks regional blood flow deficit in experimental hindlimb ischemia. J Surg Res. 2001;98:21-6.

[107] Carmeliet P, Jain RK. Angiogenesis in cancer and other diseases. Nature. 2000;407:249-57.

[108] Hanahan D, Weinberg RA. The hallmarks of cancer. Cell. 2000;100:57-70.

[109] Kumar I, Staton CA, Cross SS, Reed MW, Brown NJ. Angiogenesis, vascular endothelial growth factor and its receptors in human surgical wounds. The British journal of surgery. 2009;96:1484-91.

[110] Gibbons GH, Dzau VJ. The emerging concept of vascular remodeling. The New England journal of medicine. 1994;330:1431-8.

[111] Rey S, Semenza GL. Hypoxia-inducible factor-1-dependent mechanisms of vascularization and vascular remodelling. Cardiovascular research. 2010;86:236-42.

[112] Weis SM, Cheresh DA. Tumor angiogenesis: molecular pathways and therapeutic targets. Nature medicine. 2011;17:1359-70.

[113] Prewett M, Huber J, Li Y, Santiago A, O'Connor W, King K, et al. Antivascular endothelial growth factor receptor (fetal liver kinase 1) monoclonal antibody inhibits tumor angiogenesis and growth of several mouse and human tumors. Cancer research. 1999;59:5209-18.

[114] Qin J, Reif R, Zhi Z, Dziennis S, Wang R. Hemodynamic and morphological vasculature response to a burn monitored using a combined dual-wavelength laser speckle and optical microangiography imaging system. Biomedical optics express. 2012;3:455-66.

[115] Poole KM, Tucker-Schwartz JM, Sit WW, Walsh AJ, Duvall CL, Skala MC. Quantitative optical imaging of vascular response in vivo in a model of peripheral arterial disease. American journal of physiology Heart and circulatory physiology. 2013;305:H1168-80.

[116] Vakoc BJ, Lanning RM, Tyrrell JA, Padera TP, Bartlett LA, Stylianopoulos T, et al. Three-dimensional microscopy of the tumor microenvironment in vivo using optical frequency domain imaging. Nature medicine. 2009;15:1219-23.

[117] Hendargo HC, Estrada R, Chiu SJ, Tomasi C, Farsiu S, Izatt JA. Automated non-rigid registration and mosaicing for robust imaging of distinct retinal capillary beds using speckle variance optical coherence tomography. Biomedical optics express. 2013;4:803-21.

[118] Kim DY, Fingler J, Werner JS, Schwartz DM, Fraser SE, Zawadzki RJ. In vivo volumetric imaging of human retinal circulation with phase-variance optical coherence tomography. Biomedical optics express. 2011;2:1504-13.

[119] Schmidt-Erfurth U, Leitgeb RA, Michels S, Povazay B, Sacu S, Hermann B, et al. Three-dimensional ultrahigh-resolution optical coherence tomography of macular diseases. Investigative ophthalmology & visual science. 2005;46:3393-402.

[120] Schmoll T, Kolbitsch C, Leitgeb RA. Ultra-high-speed volumetric tomography of human retinal blood flow. Optics express. 2009;17:4166-76.

[121] Zotter S, Pircher M, Torzicky T, Baumann B, Yoshida H, Hirose F, et al. Large-field high-speed polarization sensitive spectral domain OCT and its applications in ophthalmology. Biomedical optics express. 2012;3:2720-32.

[122] Davoudi B, Morrison M, Bizheva K, Yang VX, Dinniwell R, Levin W, et al. Optical coherence tomography platform for microvascular imaging and quantification: initial experience in late oral radiation toxicity patients. Journal of biomedical optics. 2013;18:76008.

[123] Zhao Y, Chen Z, Saxer C, Xiang S, de Boer JF, Nelson JS. Phase-resolved optical coherence tomography and optical Doppler tomography for imaging blood flow in human skin with fast scanning speed and high velocity sensitivity. Optics letters. 2000;25:114-6.

[124] Enfield J, Jonathan E, Leahy M. In vivo imaging of the microcirculation of the volar forearm using correlation mapping optical coherence tomography (cmOCT). Biomedical optics express. 2011;2:1184-93.

[125] Mariampillai A, Leung MK, Jarvi M, Standish BA, Lee K, Wilson BC, et al. Optimized speckle variance OCT imaging of microvasculature. Optics letters. 2010;35:1257-9.

[126] Zhi Z, Cepurna W, Johnson E, Shen T, Morrison J, Wang RK. Volumetric and quantitative imaging of retinal blood flow in rats with optical microangiography. Biomedical optics express. 2011;2:579-91.

[127] Jenkins MW, Watanabe M, Rollins AM. Longitudinal Imaging of Heart Development With Optical Coherence Tomography. Ieee J Sel Top Quant. 2012;18:1166-75.

[128] Poole KM, Patil CA, Nelson CE, McCormack DR, Madonna MC, Duvall CL, et al. Longitudinal study of arteriogenesis with swept source optical coherence tomography and hyperspectral imaging. SPIE Photonics West. San Francisco, CA: SPIE; 2014. p. 89341Z-Z-7.

[129] Meisner JK, Annex BH, Price RJ. Despite normal arteriogenic and angiogenic responses, hind limb perfusion recovery and necrotic and fibroadipose tissue clearance are impaired in matrix metalloproteinase 9-deficient mice. Journal of vascular surgery. 2014;In Press.

[130] Mahmud MS, Cadotte DW, Vuong B, Sun C, Luk TW, Mariampillai A, et al. Review of speckle and phase variance optical coherence tomography to visualize microvascular networks. Journal of biomedical optics. 2013;18:50901.

[131] Frangi AF, Niessen WJ, Vincken KL, Viergever MA. Multiscale vessel enhancement filtering. Lect Notes Comput Sc. 1998;1496:130-7.

[132] Yousefi S, Qin J, Zhi Z, Wang RK. Label-free optical lymphangiography: development of an automatic segmentation method applied to optical coherence tomography to visualize lymphatic vessels using Hessian filters. Journal of biomedical optics. 2013;18:86004.

[133] Kroon D. Hessian based Frangi vesselness filter. MathWorks2009.

[134] Reif R, Qin J, An L, Zhi Z, Dziennis S, Wang R. Quantifying optical microangiography images obtained from a spectral domain optical coherence tomography system. International journal of biomedical imaging. 2012;2012:509783.

[135] Seaman ME, Peirce SM, Kelly K. Rapid analysis of vessel elements (RAVE): a tool for studying physiologic, pathologic and tumor angiogenesis. PloS one. 2011;6:e20807.

[136] Landazuri N, Joseph G, Guldberg RE, Taylor WR. Growth and Regression of Vasculature in Healthy and Diabetic Mice after Hind Limb Ischemia. Am J Physiol Regul Integr Comp Physiol. 2012;In press.

[137] Conroy L, DaCosta RS, Vitkin IA. Quantifying tissue microvasculature with speckle variance optical coherence tomography. Optics letters. 2012;37:3180-2.

[138] Schmoll T, Singh AS, Blatter C, Schriefl S, Ahlers C, Schmidt-Erfurth U, et al. Imaging of the parafoveal capillary network and its integrity analysis using fractal dimension. Biomedical optics express. 2011;2:1159-68.

[139] Unterhuber A, Povazay B, Hermann B, Sattmann H, Chavez-Pirson A, Drexler W. In vivo retinal optical coherence tomography at 1040 nm - enhanced penetration into the choroid. Optics express. 2005;13:3252-8.

[140] Reif R, Baran U, Wang RK. Motion artifact and background noise suppression on optical microangiography frames using a naive Bayes mask. Applied optics. 2014;53:4164-71.

[141] Liu G, Wang R. Stripe motion artifact suppression in phase-resolved OCT blood flow images of the human eye based on the frequency rejection filter. Chin Opt Lett. 2013;11:031701.

[142] Kraus MF, Potsaid B, Mayer MA, Bock R, Baumann B, Liu JJ, et al. Motion correction in optical coherence tomography volumes on a per A-scan basis using orthogonal scan patterns. Biomedical optics express. 2012;3:1182-99.

[143] Yousefi S, Zhi Z, Wang RK. Eigendecomposition-based clutter filtering technique for optical micro-angiography. IEEE transactions on bio-medical engineering. 2011;58.

[144] Ross R. Atherosclerosis--an inflammatory disease. The New England journal of medicine. 1999;340:115-26.

[145] Stocker R, Keaney JF, Jr. New insights on oxidative stress in the artery wall. Journal of thrombosis and haemostasis : JTH. 2005;3:1825-34.

[146] Dopheide JF, Doppler C, Scheer M, Obst V, Radmacher MC, Radsak MP, et al. Critical limb ischaemia is characterised by an increased production of whole blood reactive oxygen species and expression of TREM-1 on neutrophils. Atherosclerosis. 2013;229:396-403.

[147] Grisham MB, Granger DN, Lefer DJ. Modulation of leukocyte-endothelial interactions by reactive metabolites of oxygen and nitrogen: relevance to ischemic heart disease. Free radical biology & medicine. 1998;25:404-33.

[148] Wang Q, Tang XN, Yenari MA. The inflammatory response in stroke. Journal of neuroimmunology. 2007;184:53-68.

[149] Joe B, Vijaykumar M, Lokesh BR. Biological properties of curcumin-cellular and molecular mechanisms of action. Critical reviews in food science and nutrition. 2004;44:97-111.

[150] Singh S, Aggarwal BB. Activation of transcription factor NF-kappa B is suppressed by curcumin (diferuloylmethane) [corrected]. The Journal of biological chemistry. 1995;270:24995-5000.

[151] Barzegar A, Moosavi-Movahedi AA. Intracellular ROS protection efficiency and free radical-scavenging activity of curcumin. PloS one. 2011;6:e26012.

[152] Avci G, Kadioglu H, Sehirli AO, Bozkurt S, Guclu O, Arslan E, et al. Curcumin protects against ischemia/reperfusion injury in rat skeletal muscle. J Surg Res. 2012;172:e39-46.

[153] Rogers NM, Stephenson MD, Kitching AR, Horowitz JD, Coates PT. Amelioration of renal ischaemia-reperfusion injury by liposomal delivery of curcumin to renal tubular epithelial and antigen-presenting cells. British journal of pharmacology. 2012;166:194-209.

[154] Anand P, Kunnumakkara AB, Newman RA, Aggarwal BB. Bioavailability of curcumin: problems and promises. Molecular pharmaceutics. 2007;4:807-18.

[155] Jeffery H, Davis SS, Ohagan DT. The Preparation and Characterization of Poly(Lactide-Co-Glycolide) Microparticles .1. Oil-in-Water Emulsion Solvent Evaporation. Int J Pharm. 1991;77:169-75.

[156] Convertine AJ, Benoit DS, Duvall CL, Hoffman AS, Stayton PS. Development of a novel endosomolytic diblock copolymer for siRNA delivery. Journal of controlled release : official journal of the Controlled Release Society. 2009;133:221-9.

[157] Nagai A, Koike N, Kudo H, Nishikubo T. Controlled Thioacyl Group Transfer (TAGT) Polymerization of Cyclic Sulfide: Novel Approach to AB Diblock Copolymers by the Combination of RAFT and TAGT Polymerizations. Macromolecules. 2007;40:8129-31.

[158] Fundueanu G, Constantin M, Stanciu C, Theodoridis G, Ascenzi P. pH- and temperature-sensitive polymeric microspheres for drug delivery: the dissolution of copolymers modulates drug release. Journal of materials science Materials in medicine. 2009;20:2465-75.

[159] Hogg N, Darley-Usmar VM, Wilson MT, Moncada S. Production of hydroxyl radicals from the simultaneous generation of superoxide and nitric oxide. The Biochemical journal. 1992;281 (Pt 2):419-24.

[160] Kuzkaya N, Weissmann N, Harrison DG, Dikalov S. Interactions of peroxynitrite, tetrahydrobiopterin, ascorbic acid, and thiols: implications for uncoupling endothelial nitric-oxide synthase. The Journal of biological chemistry. 2003;278:22546-54.

[161] Joshi RV, Nelson CE, Poole KM, Skala MC, Duvall CL. Dual pH- and temperature-responsive microparticles for protein delivery to ischemic tissues. Acta Biomater. 2013;9:6526-34.

[162] Lorsbach RB, Murphy WJ, Lowenstein CJ, Snyder SH, Russell SW. Expression of the Nitric-Oxide Synthase Gene in Mouse Macrophages Activated for Tumor-Cell Killing - Molecular-Basis for the Synergy between Interferon-Gamma and Lipopolysaccharide. Journal of Biological Chemistry. 1993;268:1908-13.

[163] Mosser DM, Edwards JP. Exploring the full spectrum of macrophage activation. Nat Rev Immunol. 2008;8:958-69.

[164] Like AA, Rossini AA. Streptozotocin-induced pancreatic insulitis: new model of diabetes mellitus. Science. 1976;193:415-7.

[165] Kundu K, Knight SF, Willett N, Lee S, Taylor WR, Murthy N. Hydrocyanines: a class of fluorescent sensors that can image reactive oxygen species in cell culture, tissue, and in vivo. Angewandte Chemie. 2009;48:299-303.

[166] Poole KM, McCormack DR, Patil CA, Duvall CL, Skala MC. Quantifying the vascular response to ischemia with speckle variance optical coherence tomography. Biomedical optics express. 2014.

[167] Rosenkranz B, Winkelmann BR, Parnham MJ. Clinical pharmacokinetics of molsidomine. Clinical pharmacokinetics. 1996;30:372-84.

[168] Zhang YM, Wang H, Li JR, Jimenez DA, Levitan ES, Aizenman E, et al. Peroxynitrite-induced neuronal apoptosis is mediated by intracellular zinc release and 12-lipoxygenase activation. J Neurosci. 2004;24:10616-27.

[169] Amoli MM, Mousavizadeh R, Sorouri R, Rahmani M, Larijani B. Curcumin inhibits in vitro MCP-1 release from mouse pancreatic islets. Transplantation proceedings. 2006;38:3035-8.

[170] Wang Y, Rangan GK, Goodwin B, Tay YC, Harris DC. Lipopolysaccharide-induced MCP-1 gene expression in rat tubular epithelial cells is nuclear factor-kappaB dependent. Kidney international. 2000;57:2011-22.

[171] Tojo T, Ushio-Fukai M, Yamaoka-Tojo M, Ikeda S, Patrushev N, Alexander RW. Role of gp91(phox) (Nox2)-containing NAD(P)H oxidase in angiogenesis in response to hindlimb ischemia. Circulation. 2005;111:2347-55.

[172] Wang YJ, Pan MH, Cheng AL, Lin LI, Ho YS, Hsieh CY, et al. Stability of curcumin in buffer solutions and characterization of its degradation products. Journal of pharmaceutical and biomedical analysis. 1997;15:1867-76.

[173] O'Toole MG, Henderson RM, Soucy PA, Fasciotto BH, Hoblitzell PJ, Keynton RS, et al. Curcumin encapsulation in submicrometer spray-dried chitosan/Tween 20 particles. Biomacromolecules. 2012;13:2309-14.

[174] Shahani K, Panyam J. Highly loaded, sustained-release microparticles of curcumin for chemoprevention. Journal of pharmaceutical sciences. 2011;100:2599-609.

[175] May RC, Machesky LM. Phagocytosis and the actin cytoskeleton. Journal of cell science. 2001;114:1061-77.

[176] Shive MS, Anderson JM. Biodegradation and biocompatibility of PLA and PLGA microspheres. Advanced drug delivery reviews. 1997;28:5-24.

[177] Champion JA, Walker A, Mitragotri S. Role of particle size in phagocytosis of polymeric microspheres. Pharmaceutical research. 2008;25:1815-21.

[178] Hirosue S, Kourtis IC, van der Vlies AJ, Hubbell JA, Swartz MA. Antigen delivery to dendritic cells by poly(propylene sulfide) nanoparticles with disulfide conjugated peptides: Cross-presentation and T cell activation. Vaccine. 2010;28:7897-906.

[179] Rhee SG. Cell signaling. H2O2, a necessary evil for cell signaling. Science. 2006;312:1882-3.

[180] Hood ED, Chorny M, Greineder CF, I SA, Levy RJ, Muzykantov VR. Endothelial targeting of nanocarriers loaded with antioxidant enzymes for protection against vascular oxidative stress and inflammation. Biomaterials. 2014;35:3708-15.

[181] Derochette S, Franck T, Mouithys-Mickalad A, Deby-Dupont G, Neven P, Serteyn D. Intra- and extracellular antioxidant capacities of the new water-soluble form of curcumin (NDS27) on stimulated neutrophils and HL-60 cells. Chemico-biological interactions. 2013;201:49-57.

[182] Kim HW, Lin A, Guldberg RE, Ushio-Fukai M, Fukai T. Essential role of extracellular SOD in reparative neovascularization induced by hindlimb ischemia. Circulation research. 2007;101:409-19.

[183] Urao N, Inomata H, Razvi M, Kim HW, Wary K, McKinney R, et al. Role of nox2-based NADPH oxidase in bone marrow and progenitor cell function involved in neovascularization induced by hindlimb ischemia. Circulation research. 2008;103:212-20.

[184] Ruiter MS, van Golde JM, Schaper NC, Stehouwer CD, Huijberts MS. Diabetes impairs arteriogenesis in the peripheral circulation: review of molecular mechanisms. Clinical science. 2010;119:225-38.

[185] Woo CH, Shishido T, McClain C, Lim JH, Li JD, Yang J, et al. Extracellular signal-regulated kinase 5 SUMOylation antagonizes shear stress-induced antiinflammatory response and endothelial nitric oxide synthase expression in endothelial cells. Circulation research. 2008;102:538-45.

[186] Case J, Ingram DA, Haneline LS. Oxidative stress impairs endothelial progenitor cell function. Antioxidants & redox signaling. 2008;10:1895-907.

[187] Forstermann U. Nitric oxide and oxidative stress in vascular disease. Pflugers Archiv : European journal of physiology. 2010;459:923-39.

[188] Cai H, Harrison DG. Endothelial dysfunction in cardiovascular diseases: the role of oxidant stress. Circulation research. 2000;87:840-4.

[189] Lonn E, Bosch J, Yusuf S, Sheridan P, Pogue J, Arnold JM, et al. Effects of long-term vitamin E supplementation on cardiovascular events and cancer: a randomized controlled trial. Jama. 2005;293:1338-47.

[190] Salvemini D, Wang ZQ, Zweier JL, Samouilov A, Macarthur H, Misko TP, et al. A nonpeptidyl mimic of superoxide dismutase with therapeutic activity in rats. Science. 1999;286:304-6.

[191] Nassar T, Kadery B, Lotan C, Da'as N, Kleinman Y, Haj-Yehia A. Effects of the superoxide dismutase-mimetic compound tempol on endothelial dysfunction in streptozotocin-induced diabetic rats. European journal of pharmacology. 2002;436:111-8.

[192] Thiemermann C. Membrane-permeable radical scavengers (tempol) for shock, ischemia-reperfusion injury, and inflammation. Critical care medicine. 2003;31:S76-84.

[193] Pua ML, Yoshitomi T, Chonpathompikunlert P, Hirayama A, Nagasaki Y. Redox-active injectable gel using thermo-responsive nanoscale polyion complex flower micelle for noninvasive treatment of local inflammation. Journal of controlled release : official journal of the Controlled Release Society. 2013;172:914-20.

[194] Monti E, Supino R, Colleoni M, Costa B, Ravizza R, Gariboldi MB. Nitroxide TEMPOL impairs mitochondrial function and induces apoptosis in HL60 cells. Journal of cellular biochemistry. 2001;82:271-6.

[195] Reddy MK, Labhasetwar V. Nanoparticle-mediated delivery of superoxide dismutase to the brain: an effective strategy to reduce ischemia-reperfusion injury. FASEB journal : official publication of the Federation of American Societies for Experimental Biology. 2009;23:1384-95.

[196] Yun X, Maximov VD, Yu J, Zhu H, Vertegel AA, Kindy MS. Nanoparticles for targeted delivery of antioxidant enzymes to the brain after cerebral ischemia and reperfusion injury. Journal of cerebral blood flow and metabolism : official journal of the International Society of Cerebral Blood Flow and Metabolism. 2013;33:583-92.

[197] Fiore VF, Lofton MC, Roser-Page S, Yang SC, Roman J, Murthy N, et al. Polyketal microparticles for therapeutic delivery to the lung. Biomaterials. 2010;31:810-7.

[198] Giovagnoli S, Luca G, Casaburi I, Blasi P, Macchiarulo G, Ricci M, et al. Long-term delivery of superoxide dismutase and catalase entrapped in poly(lactide-co-glycolide) microspheres: in vitro effects on isolated neonatal porcine pancreatic cell clusters. Journal of controlled release : official journal of the Controlled Release Society. 2005;107:65-77.

[199] Yoshitomi T, Hirayama A, Nagasaki Y. The ROS scavenging and renal protective effects of pH-responsive nitroxide radical-containing nanoparticles. Biomaterials. 2011;32:8021-8.

[200] Tang H, Cao W, Kasturi SP, Ravindran R, Nakaya HI, Kundu K, et al. The T helper type 2 response to cysteine proteases requires dendritic cell-basophil cooperation via ROS-mediated signaling. Nature immunology. 2010;11:608-17.

[201] Zhao H, Kalivendi S, Zhang H, Joseph J, Nithipatikom K, Vasquez-Vivar J, et al. Superoxide reacts with hydroethidine but forms a fluorescent product that is distinctly different from ethidium: potential implications in intracellular fluorescence detection of superoxide. Free radical biology & medicine. 2003;34:1359-68.

[202] Nazarewicz RR, Bikineyeva A, Dikalov SI. Rapid and specific measurements of superoxide using fluorescence spectroscopy. Journal of biomolecular screening. 2013;18:498-503.

[203] Balavoine GG, Geletii YV. Peroxynitrite scavenging by different antioxidants. Part I: convenient assay. Nitric oxide : biology and chemistry / official journal of the Nitric Oxide Society. 1999;3:40-54.

[204] Kim YW, Byzova TV. Oxidative stress in angiogenesis and vascular disease. Blood. 2014;123:625-31.

[205] Hodara R, Weiss D, Joseph G, Velasquez-Castano JC, Landazuri N, Han JW, et al. Overexpression of catalase in myeloid cells causes impaired postischemic neovascularization. Arteriosclerosis, thrombosis, and vascular biology. 2011;31:2203-9.

[206] Huang PH, Tsai HY, Wang CH, Chen YH, Chen JS, Lin FY, et al. Moderate intake of red wine improves ischemia-induced neovascularization in diabetic mice--roles of endothelial progenitor cells and nitric oxide. Atherosclerosis. 2010;212:426-35.

[207] Huang PH, Lin CP, Wang CH, Chiang CH, Tsai HY, Chen JS, et al. Niacin improves ischemia-induced neovascularization in diabetic mice by enhancement of endothelial progenitor cell functions independent of changes in plasma lipids. Angiogenesis. 2012;15:377-89.

[208] Marso SP, Hiatt WR. Peripheral arterial disease in patients with diabetes. Journal of the American College of Cardiology. 2006;47:921-9.

[209] Banday AA, Marwaha A, Tallam LS, Lokhandwala MF. Tempol reduces oxidative stress, improves insulin sensitivity, decreases renal dopamine D1 receptor hyperphosphorylation, and restores D1 receptor-G-protein coupling and function in obese Zucker rats. Diabetes. 2005;54:2219-26.

[210] Pieper GM. Enhanced, unaltered and impaired nitric oxide-mediated endothelium-dependent relaxation in experimental diabetes mellitus: importance of disease duration. Diabetologia. 1999;42:204-13.

[211] Perreault M, Dombrowski L, Marette A. Mechanism of impaired nitric oxide synthase activity in skeletal muscle of streptozotocin-induced diabetic rats. Diabetologia. 2000;43:427-37.

[212] Nagareddy PR, Xia Z, McNeill JH, MacLeod KM. Increased expression of iNOS is associated with endothelial dysfunction and impaired pressor responsiveness in streptozotocin-induced diabetes. American journal of physiology Heart and circulatory physiology. 2005;289:H2144-52.

[213] Qi Z, Fujita H, Jin J, Davis LS, Wang Y, Fogo AB, et al. Characterization of susceptibility of inbred mouse strains to diabetic nephropathy. Diabetes. 2005;54:2628-37.

[214] Cooke JP, Losordo DW. Modulating the vascular response to limb ischemia: angiogenic and cell therapies. Circulation research. 2015;116:1561-78.

[215] Simons M, Alitalo K, Annex BH, Augustin HG, Beam C, Berk BC, et al. State-of-the-Art Methods for Evaluation of Angiogenesis and Tissue Vascularization: A Scientific Statement From the American Heart Association. Circulation research. 2015;116:e99-132.

[216] Bezerra HG, Attizzani GF, Sirbu V, Musumeci G, Lortkipanidze N, Fujino Y, et al. Optical coherence tomography versus intravascular ultrasound to evaluate coronary artery disease and percutaneous coronary intervention. JACC Cardiovascular interventions. 2013;6:228-36.

[217] Eiberg JP, Gronvall Rasmussen JB, Hansen MA, Schroeder TV. Duplex ultrasound scanning of peripheral arterial disease of the lower limb. European journal of vascular and endovascular surgery : the official journal of the European Society for Vascular Surgery. 2010;40:507-12.

[218] Tang GL, Chin J, Kibbe MR. Advances in diagnostic imaging for peripheral arterial disease. Expert review of cardiovascular therapy. 2010;8:1447-55.

[219] Chin JA, Wang EC, Kibbe MR. Evaluation of hyperspectral technology for assessing the presence and severity of peripheral artery disease. Journal of vascular surgery. 2011;54:1679-88.

[220] Nouvong A, Hoogwerf B, Mohler E, Davis B, Tajaddini A, Medenilla E. Evaluation of diabetic foot ulcer healing with hyperspectral imaging of oxyhemoglobin and deoxyhemoglobin. Diabetes care. 2009;32:2056-61.

[221] Muscoli C, Cuzzocrea S, Riley DP, Zweier JL, Thiemermann C, Wang ZQ, et al. On the selectivity of superoxide dismutase mimetics and its importance in pharmacological studies. British journal of pharmacology. 2003;140:445-60.

[222] Kavanaugh TE, Werfel TA, Cho H, Hasty KA, Duvall CL. Particle-based technologies for osteoarthritis detection and therapy. Drug delivery and translational research. 2015.

[223] Spence S, Greene MK, Fay F, Hams E, Saunders SP, Hamid U, et al. Targeting Siglecs with a sialic acid-decorated nanoparticle abrogates inflammation. Science translational medicine. 2015;7:303ra140.

[224] Sato K, Kadiiska MB, Ghio AJ, Corbett J, Fann YC, Holland SM, et al. In vivo lipid-derived free radical formation by NADPH oxidase in acute lung injury induced by lipopolysaccharide: a model for ARDS. FASEB journal : official publication of the Federation of American Societies for Experimental Biology. 2002;16:1713-20.

[225] Kajic V, Esmaeelpour M, Glittenberg C, Kraus MF, Honegger J, Othara R, et al. Automated three-dimensional choroidal vessel segmentation of 3D 1060 nm OCT retinal data. Biomedical optics express. 2013;4:134-50.